Chem Soc Rev

Progress on Ternary Oxide-Based Photoanodes for Use in Photoelectrochemical Cells for Solar Water Splitting

Journal:	*Chemical Society Reviews*
Manuscript ID	CS-REV-09-2018-000761.R1
Article Type:	Review Article
Date Submitted by the Author:	19-Nov-2018
Complete List of Authors:	Lee, Dong Ki; University of Wisconsin Madison, Chemistry Lee, Dongho; University of Wisconsin Madison, Chemistry Lumley, Margaret; University of Wisconsin Madison, Chemistry Choi, Kyoung-Shin; University of Wisconsin Madison, Chemistry

Progress on Ternary Oxide-Based Photoanodes for Use in Photoelectrochemical Cells for Solar Water Splitting

Dong Ki Lee, Dongho Lee, Margaret A. Lumley, and Kyoung-Shin Choi*

Department of Chemistry, University of Wisconsin-Madison, Madison, WI 53706, USA.

* Correspondence and requests for materials should be addressed to K.-S.C. (email: kschoi@chem.wisc.edu)

Abstract

Solar water splitting using photoelectrochemical cells (PECs) has emerged as one of the most promising routes to produce hydrogen as a clean and renewable fuel source. Among various semiconductors that have been considered as photoelectrodes for use in PECs, oxide-based photoanodes are particularly attractive because of their stability in aqueous media in addition to inexpensive and facile processing compared to other types of semiconductors. However, they typically suffer from poor charge carrier separation and transport. In the past few years, there has been tremendous progress in developing ternary oxide-based photoelectrodes, specifically, photoanodes. The use of ternary oxides provides more opportunities to tune the composition and electronic structure of the photoelectrode compared to binary oxides, thus providing more freedom to tune the photoelectrochemical properties. In this article, we outline the important characteristics to analyze when evaluating photoanodes and review the major recent progress made on the development of ternary oxide-based photoanodes. For each system, we highlight the favorable and unfavorable features and summarize the strategies utilized to address the challenges associated with each material. Finally, by combining our analyses of all the photoanodes surveyed in this review, we provide possible future research directions for each compound and an outlook for constructing more efficient oxide-based PECs. Overall, this review will provide a critical overview of current ternary oxide-based photoanodes and will serve as a platform for the design of future oxide-based PECs.

1. Introduction

Since the first photoelectrochemical cell (PEC) was reported in 1972,[1] PEC-based solar water splitting has become one of the most promising routes for the environmentally benign and sustainable production of hydrogen as a clean fuel.[2-5] Semiconductor electrodes that can absorb visible light to generate electron-hole pairs and can separate and transport these charge carriers to the semiconductor/electrolyte interface are the key components of water splitting PECs.[5, 6] The doping type of the semiconductor electrode determines whether it will serve as the photoanode or photocathode of a PEC; an n-type semiconductor will serve as a photoanode while a p-type semiconductor will serve as a photocathode. To be used as a single photon absorber (i.e. only one electrode of the PEC is a semiconductor electrode) in a PEC that can achieve unassisted water splitting, the semiconductor must have a conduction band maximum (CBM) and valence band minimum (VBM) that straddle the water reduction and oxidation potentials. Semiconductors that meet this requirement while also having a bandgap that allows a solar-to-hydrogen (STH) conversion efficiency of greater than 10% are rare. Therefore, efficient PECs will most likely contain an anode and a cathode that are both semiconductors, which will both contribute to the photon absorption and photovoltage generation.[5, 7] A schematic representation of such a PEC composed of a larger bandgap photoanode and a smaller bandgap photocathode combined in tandem is shown in Figure 1. For comparison, a PEC composed of a photoanode serving as a single photon absorber paired with a metal cathode is also shown. In the tandem cell, although both electrodes absorb photons and generate electron-hole pairs, only the minority carriers are used to drive chemical reactions. The majority carriers of each electrode move to the back contact and recombine. As a result, only the location of the VBM of the photoanode and CBM of the photocathode are absolutely critical conditions for the selection of materials for solar water splitting. (The CBM of the photoanode and VBM of the photocathode are still important as they affect the photovoltage achievable by each electrode. This will be explained in the next section). Compared to a PEC which uses a single photon absorber, the use of a tandem cell allows for a greater number of materials to be considered for the construction of a water splitting PEC.

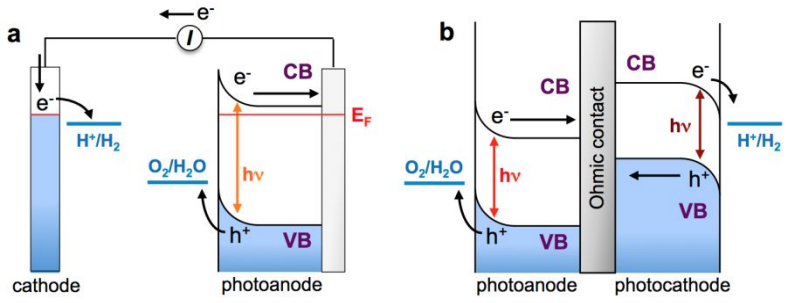

Figure 1. Schematic energy diagrams of (a) a PEC composed of a photoanode as a single photon absorber paired with a metal cathode and (b) a PEC composed of a photoanode and a photocathode in tandem (E_F: Fermi level, CB: conduction band, and VB: valence band).

Among various semiconductors that have been investigated as photoelectrodes for solar water splitting, oxide-based photoelectrodes are attractive because of their inexpensive processing costs and better stability in aqueous media compared to other types of semiconductor electrodes. These are critical advantages because the commercial viability of a water splitting

PEC is ultimately determined by the cost of hydrogen produced by the PEC, not just the STH efficiency. Early studies on oxide-based photoelectrodes focused on a few types of binary oxides (e.g. TiO_2, Fe_2O_3, WO_3, ZnO). However, in the past decade, a significant effort has been made to investigate ternary oxide-based photoelectrodes for application in water splitting PECs. Ternary oxides are composed of two different metal ions combined in an oxide matrix. Using ternary oxides instead of binary oxides provides more opportunities to tune the composition and atomic and electronic structures of photoelectrodes, which can directly impact their photoelectrochemical properties.

The purpose of this article is to provide a critical review of n-type ternary oxides that have been investigated as photoanodes for water splitting PECs. The oxides reviewed in this study meet the following criteria. First, the oxides have a bandgap energy ≤ 2.5 eV. Second, the oxides have demonstrated a photovoltage gain for water oxidation (i.e. the difference between the photocurrent onset for water oxidation and the thermodynamic water oxidation potential of 1.23 V vs. RHE) of at least ~0.4 V. This means that their photocurrent onset potentials for water oxidation have been shown to be more negative than ~0.8 V vs. RHE. Third, there are several studies that contain reliable reports of the photoelectrochemical properties of the oxide being investigated as a photoanode. For each compound reviewed in this study, we will summarize the relevant properties and performances of the compound related to solar water oxidation. Then, we will discuss the advantages and limitations of each compound, major efforts made to overcome these limitations, and possible future research directions. Finally, by integrating our understanding and analyses of all the photoanodes surveyed in this review, we will offer our outlook for constructing more efficient oxide-based photoanodes. The information and discussion provided in this review will be useful not only for the construction of water splitting PECs but also for other types of PECs used for solar fuel production (e.g. CO_2 reduction) where water oxidation is used as the anode reaction.

2. Evaluation of Photoanodes

Before reviewing the photoanode materials, important factors to consider when evaluating photoanodes are briefly summarized in this section. This overview will be useful to understand the discussions and insights provided in the review section.

Bandgap energy is one of the most important criteria in evaluating a photoanode as it determines the maximum photocurrent density that can be generated by a given material. Figure 2 shows the relationship between the bandgap and the maximum achievable photocurrent density.[8] We emphasize that the relationship shown in Figure 2 assumes that all photons available in the solar spectrum with an energy equal to or greater than the bandgap energy are utilized by the material. In other words, this plot assumes 100% incident photon-to-current efficiency (IPCE). (This means that other factors that can affect photocurrent generation, such as photon absorption, electron-hole separation, and interfacial charge injection as well as the band edge positions relative to the water reduction and oxidation potentials, are not considered).

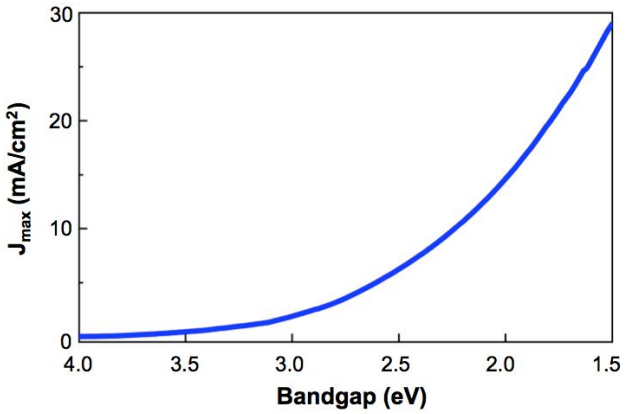

Figure 2. Theoretical maximum photocurrent density (J_{max}) as a function of semiconductor bandgap energy calculated using the photon flux of the AM 1.5G solar spectrum[8] assuming 100% IPCE.

To date, photocurrent densities generated by most oxide-based photoanodes are far from the predicted values shown in Figure 2. This is partly because not all incident photons with energy equal to or greater than the bandgap energy of the semiconductor are absorbed by the semiconductor. One critical factor that affects photon absorption is the absorption coefficient, α, which indicates how strongly a semiconductor absorbs light at a given wavelength. The inverse of the absorption coefficient is the light penetration depth (α^{-1}) and indicates how thick the photoelectrode needs to be to achieve an optical density of 1 at a given wavelength.[9] If α^{-1} is small, a thinner photoanode film can be used, which is advantageous to reduce bulk recombination.

Even if this loss in photon absorption is taken into account and only the number of absorbed photons is used to calculate the expected photocurrent density (using the experimentally obtained absorbance spectra) assuming 100% absorbed photon-to-current efficiency (APCE), the measured photocurrent densities (J_{PEC}) can still be much lower than those predicted (J_{abs}). This is because not all electron-hole pairs generated by photon absorption can be separated and utilized for photocurrent generation due to bulk and surface recombination. The following equation shows the relationship between J_{PEC} and J_{abs}.[10-12]

$$J_{PEC} = J_{abs} \times \eta_{sep} \times \eta_{ox}$$

In this equation, the bulk separation efficiency, η_{sep}, represents the percentage of photogenerated holes that reach the surface of the semiconductor. The charge injection efficiency, η_{ox}, represents the percentage of surface reaching holes that are injected into the solution to perform the desired oxidation reaction. Since the surface reaching holes that are not used for the desired oxidation reaction are lost to surface recombination (assuming that none are used for photocorrosion), η_{ox} can also be referred to as the surface separation efficiency. When J_{PEC} is measured using a kinetically fast hole acceptor (e.g. sulfite), η_{ox} is assumed to be 1 and η_{sep} can easily be calculated by dividing J_{PEC} by J_{abs}. To calculate η_{ox} for water oxidation, J_{PEC} for water oxidation can be divided by J_{PEC} for the oxidation of a hole acceptor with $\eta_{ox} = 1$

Most oxide-based photoelectrodes suffer from an extremely poor η_{sep} so improving η_{sep} is critical to increase J_{PEC} to be closer to $J_{abs.}$ Since η_{ox} can be improved by the addition of an appropriate oxygen evolution catalyst (OEC), η_{ox} of a bare semiconductor electrode is not as important as η_{sep}. Sulfite and H_2O_2 are the most commonly used hole acceptors whose η_{ox} is

assumed to be equal to 1.[13] However, it should be emphasized that this assumption may fail when using a photoanode whose rate of surface recombination is extremely fast (faster than the rate of sulfite or H_2O_2 oxidation). In this case, the calculated η_{sep} will be lower than the actual η_{sep} because the assumption that $\eta_{ox} = 1$ is no longer valid and is less than 1.

The limited η_{sep} of most oxide-based photoanodes is related to their poor charge transport properties. The factors that affect the conductivity of the majority carriers (electrons for n-type photoanodes) are the carrier concentration and the carrier mobility. Improving these properties can help to decrease bulk recombination. The transport properties of the minority carriers (holes for n-type photoanodes) are often evaluated in terms of the minority carrier diffusion length, which is determined by the lifetime and mobility of the minority carriers.[14] These charge transport characteristics, which are critical to understanding and optimizing the performance of photoanodes, are discussed in the review section when available.

Finally, the CBM of the photoanode is another critical factor to consider as it dictates the maximum photovoltage that can be achieved by a given photoanode. (We assume that any material selected as a photoanode already has a VBM properly located to use holes for water oxidation as this is an absolute requirement for photoanodes used in a tandem PEC). As previously mentioned, the photovoltage gain for water oxidation is the difference between the photocurrent onset for water oxidation and the thermodynamic potential for water oxidation (1.23 V vs. RHE). The most negative photocurrent onset potential that can be achieved by a photoanode is equal to its flatband potential (E_{FB}) and the photocurrent onset will be the same as the E_{FB} when no holes are lost to surface recombination. The E_{FB} is not an intrinsic property of a semiconductor, however, as it can be changed by altering the carrier density. Furthermore, since the E_{FB} of any non-degenerate semiconductor cannot be more negative than its CBM, the CBM is the factor that ultimately limits the E_{FB} position, and, therefore, the maximum photovoltage that can be achieved for water oxidation.

Figure 3 illustrates how the photovoltage for water oxidation plays a role in determining the STH efficiency of a PEC. In this figure, two hypothetical photoanodes with the same bandgap but different photocurrent onset potentials are compared. Photoanode A can achieve a photovoltage for water oxidation of ~1 V and photoanode B can achieve a photovoltage for water oxidation of ~0.7 V. When these photoanodes are combined with a photocathode, the operating current density (J_{op}) of the resulting PECs can be determined by the point where the photoanode and photocathode J-V curves intersect (the crossing point). In this example, a photocathode that can achieve a photovoltage for H_2 evolution of 0.6 V is used. By looking at the crossing point, it is evident that photoanode A can achieve a much higher J_{op} than photoanode B. This means that the STH efficiency achieved by photoanode A will be higher even though photoanodes A and B have the same bandgap. (The J_{op} multiplied by 1.23 V provides the STH efficiency of a PEC performing unassisted solar water splitting). Even when photoanode A is compared with another photoanode that has a smaller bandgap (photoanode C), photoanode A can achieve a higher J_{op} if photoanode C exhibits only a very limited photovoltage. (The smaller bandgap of photoanode C results in higher photocurrent generation in the high bias region where the photocurrent approaches the photocurrent limited by photon absorption, J_{abs}). This is why the CBM position is a very important factor for evaluating a photoanode. This is also why photoanodes that have not shown an onset potential for water oxidation more negative than 0.8 V vs. RHE are not covered in this review.

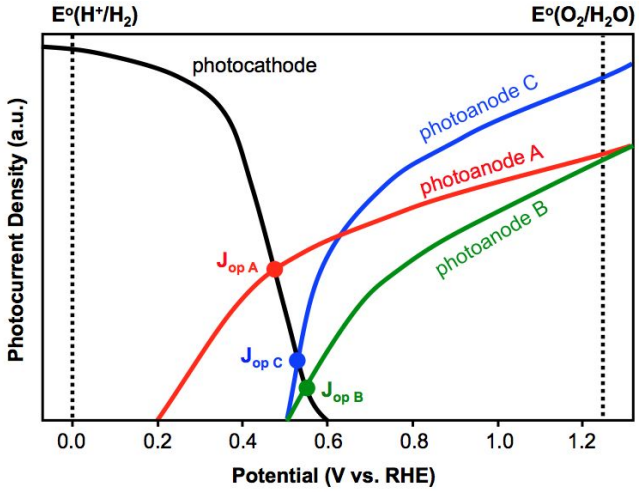

Figure 3. A scheme showing J-V plots of three hypothetical photoanodes and their J_{op}s when combined with a photocathode in a PEC. Photoanodes A and B have the same bandgap but photoanode A has an earlier photocurrent onset potential. Photoanodes B and C have the same photocurrent onset potential but photoanode C has a smaller bandgap.

3. Review of Ternary Oxide-Based Photoanodes

3-1. Metal Ferrites

$ZnFe_2O_4$ $ZnFe_2O_4$ possesses many advantageous features of Fe_2O_3, which has been extensively studied as a photoanode. These include a relatively narrow bandgap (1.9 − 2.1 eV), exceptional (photo)stability in basic media, and the low cost and environmentally benign nature of its constituent elements.[15, 16] One major benefit of $ZnFe_2O_4$ over Fe_2O_3 for use in a water splitting PEC is its CBM position. The CBM of Fe_2O_3 is more positive than the water reduction potential by ~200 mV while that of $ZnFe_2O_4$ is slightly more negative than the water reduction potential,[15] which was confirmed by its ability to produce H_2 when used as a photocatalyst.[17, 18] This feature makes $ZnFe_2O_4$ more thermodynamically suitable for use in a water splitting PEC. However, despite this advantage, the performances of $ZnFe_2O_4$ photoanodes demonstrated to date have been inferior to those of Fe_2O_3.[19, 20] The most notable performances of $ZnFe_2O_4$ demonstrated for solar water oxidation have been summarized in Table 1.

$ZnFe_2O_4$ was first investigated as a photoanode by Blasse and co-workers in 1985.[21] The authors prepared $ZnFe_2O_4$ as a pellet using solid state methods and subsequently annealed at 700 °C in a N_2 atmosphere to improve its n-type character. However, photocurrent generated by the resulting $ZnFe_2O_4$ photoanode in pH 14 NaOH under illumination using 300 nm light was low (0.01 mA/cm^2 at 1.23 V vs. RHE). Wijayantha and co-workers investigated $ZnFe_2O_4$ electrodes prepared by aerogel-assisted chemical vapor deposition (CVD),[22] where the particle size and porosity of $ZnFe_2O_4$ films could be controlled by changing the solvent used for the precursor solution. The authors observed that a decrease in particle size (from ~150 − 200 nm to ~25 − 40 nm) and an increase in surface area improved the photocurrent density of $ZnFe_2O_4$ for water oxidation from 0.08 mA/cm^2 up to 0.16 mA/cm^2 at 1.23 V vs. RHE in pH 14 NaOH. This result suggests that bulk electron-hole recombination is one of the major limitations of $ZnFe_2O_4$, which is also a major challenge for Fe_2O_3.

Table 1. Comparison of solar water oxidation performances of $ZnFe_2O_4$ photoanodes where $ZnFe_2O_4$ was used as a single photon absorber.

Electrode	Preparation method	Onset (V_{RHE})	J at 1.23 V_{RHE} (mA/cm^2)	Electrolyte	IPCE at 400 nm and 1.23 V_{RHE}	Stability
$ZnFe_2O_4$[22]	Aerogel assisted-chemical vapor deposition	0.88	0.35	pH 14 NaOH	10%	-
$ZnFe_2O_4$[23]	Drop-casting a Zn solution on FeOOH followed by annealing and microwave treatment	0.64	0.24	pH 14 NaOH	7%	3 h stable
$ZnFe_2O_4$[24]	Drop-casting a Zn solution on FeOOH followed by annealing and H_2 treatment	0.75	0.32	pH 14 NaOH	-	3 h stable
$ZnFe_2O_4$/ $NiFeO_x$[25]	Drop-casting a Zn solution on FeOOH followed by annealing and H_2 treatment	0.53	0.35	pH 14 NaOH	8% at 1.1 V_{RHE}	24 h stable
TiO_2/ $ZnFe_2O_4$/ $NiFeO_x$[26]	Drop-casting a Zn solution on FeOOH followed by microwave treatment and H_2 treatment	0.62	0.92	pH 14 NaOH	8%	11 h stable
$ZnFe_2O_4$/ $NiFeO_x$[27]	Drop-casting a Zn solution on FeOOH followed by annealing and H_2 heat treatment	0.85	1.00	pH 14 NaOH	6%	-
$ZnFe_2O_4$[28]	Atomic layer deposition on an inverse opal structured-substrate	0.90	0.26	pH 13 NaOH	2%	3 h stable
$ZnFe_2O_4$[29]	Spray pyrolysis, Ti doping	0.95	0.35	pH 14 NaOH	3%	5 h stable

Lee and co-workers prepared $ZnFe_2O_4$ by first growing an array of FeOOH nanorods (diameter = 40 nm, thickness = 400 nm) on fluorine-doped tin oxide (FTO) using chemical bath deposition.[23] They then drop-casted an aqueous $Zn(NO_3)_2$ solution onto their FeOOH electrodes and annealed to form $ZnFe_2O_4$. After removing the excess ZnO layer in NaOH solution, pure $ZnFe_2O_4$ films could be obtained. While the photocurrent density of the as-prepared $ZnFe_2O_4$ photoanodes was not considerable (~0.02 mA/cm^2 at 1.23 V vs. RHE in pH 14 NaOH), it increased to 0.24 mA/cm^2 at 1.23 V vs. RHE after a microwave heat treatment. The authors examined the effect of the microwave treatment on η_{sep} and η_{ox} by comparing the photocurrent densities for water oxidation and H_2O_2 oxidation.[10, 30] The authors showed that the microwave treatment caused η_{sep} to increase from 4% to 8% at 1.23 V vs. RHE by improving the crystallinity of $ZnFe_2O_4$, which was confirmed by a decrease in the full width at half-maximum (FWHM) of X-ray diffraction (XRD) peaks. The authors also showed that the microwave treatment increased η_{ox} from 10% to 80% at 1.23 V vs. RHE by decreasing surface defect sites formed during the removal process of the excess ZnO layer. Lastly, the authors performed a stability test at 1.23 V vs. RHE and showed that a stable photocurrent density of 0.24 mA/cm^2 could be maintained for 3 h without the aid of an OEC.

In a follow-up paper by Lee and co-workers, the microwave treatment was replaced with H_2-treatment (i.e. annealing at 200 °C in a H_2 atmosphere).[24] The H_2 treatment created additional oxygen vacancies, which was confirmed by the O 1s spectra obtained using X-ray photoelectron spectroscopy (XPS). The treatment also resulted in a 10-fold increase in the carrier density, which was confirmed by a decrease in slope of the Mott-Schottky plots measured in pH 14 NaOH. A corresponding shift of the E_{FB} was not observed, however. The authors showed that the H_2 treatment could increase the η_{sep} from 2% to 8% and the η_{ox} from 35% to 90% at 1.23 V vs. RHE compared to the untreated sample. The photocurrent density for water oxidation achieved by the H_2-treated $ZnFe_2O_4$ without the addition of an OEC layer was 0.32 mA/cm^2 at 1.23 V vs. RHE in pH 14 NaOH.

Recently, Sivula and co-workers examined the effect of adding a $NiFeO_x$ OEC layer.[25] They prepared H_2-treated $ZnFe_2O_4$ using the method reported by Lee and co-workers[24] and deposited the $NiFeO_x$ OEC on the surface by drop-casting a solution containing Fe and Ni precursors followed by annealing at 100 °C.[25] Although the same synthesis method was used, the pristine $ZnFe_2O_4$ photoanode prepared by Sivula and co-workers showed an earlier photocurrent onset (~0.53 V vs. RHE compared to ~0.75 V vs. RHE) and a lower photocurrent density at 1.23 V vs. RHE (0.18 mA/cm^2 compared to 0.32 mA/cm^2) for water oxidation in pH 14 NaOH electrolyte. The authors reported that the E_{FB} of $ZnFe_2O_4$ is ~0.5 V vs. RHE, which was determined by the photocurrent onset for H_2O_2 oxidation (i.e. construction of a Butler plot using the J-V plot for H_2O_2 oxidation). Their results showed that the addition of the $NiFeO_x$ OEC resulted in a negligible change in photocurrent onset potential for water oxidation; however, the fill factor increased considerably and a photocurrent density of 0.35 mA/cm^2 was achieved at 1.23 V vs. RHE. The authors concluded that although the addition of the OEC could improve the η_{ox} for water oxidation from 42% to 75% at 1.23 V vs. RHE, the low η_{sep} (12% at 1.23 V vs. RHE) is a major limitation of $ZnFe_2O_4$.

In a more recent study, Lee and co-workers synthesized $ZnFe_2O_4$ using a combination of microwave treatment and H_2 treatment.[26] In addition, they added a thin TiO_2 layer between the FTO substrate and $ZnFe_2O_4$ layer to block electron injection from FTO to the electrolyte. The bottom TiO_2 layer was prepared by spin coating a Ti(IV) diisopropoxide bis(acetylacetonate) solution on FTO followed by annealing at 250 °C. The thickness of the resulting TiO_2 layer was 2 – 7 nm. FeOOH nanorods were then deposited on the FTO/TiO_2 substrate using the previously reported method.[23] An aqueous $Zn(NO_3)_2$ solution was drop-casted onto FeOOH followed by microwaving for 2 min to form $ZnFe_2O_4$ without pre-annealing the sample in a furnace. The excess ZnO was then removed by soaking in a NaOH solution. Based on the XRD patterns, the resulting $ZnFe_2O_4$ electrode showed comparable crystallinity to a $ZnFe_2O_4$ electrode prepared by annealing in a furnace at 800 °C for 20 min. However, the microwave treatment resulted in $ZnFe_2O_4$ nanorods with a smaller average diameter (60 nm vs. 80 nm) than those prepared by annealing in a furnace and also better maintained the conductivity of the FTO substrate. The resulting FTO/TiO_2/$ZnFe_2O_4$ electrode generated a photocurrent density of 0.22 mA/cm^2 for water oxidation at 1.23 V vs. RHE in pH 14 NaOH. When the FTO/TiO_2/$ZnFe_2O_4$ electrode was subsequently treated with H_2 at 200 °C for 2 h to increase the concentration of oxygen vacancies, the photocurrent density for water oxidation was increased from 0.22 mA/cm^2 to 0.79 mA/cm^2 at 1.23 V vs. RHE. The authors showed that the H_2 treatment increased η_{sep} from 10% to 24% and η_{ox} for water oxidation from 51% to 77%. The authors then deposited an amorphous $NiFeO_x$ OEC layer on the H_2-treated FTO/TiO_2/$ZnFe_2O_4$ by photolysis of a solution containing Fe(III) and Ni(II) precursors using 1 sun illumination for 10 min, followed by a heat treatment at 100 °C

for 30 min. The resulting FTO/TiO_2/$ZnFe_2O_4$/$NiFeO_x$ electrode generated a photocurrent density for water oxidation of 0.92 mA/cm^2 at 1.23 V vs RHE in pH 14 NaOH.

In 2018, Sivula and co-workers reported an additional study of $ZnFe_2O_4$ photoanodes where they discussed the effect of spinel inversion.[27] In a normal spinel structure, the divalent ions are stabilized in the tetrahedral (T_d) sites while the trivalent ions are stabilized in the octahedral (O_h) sites. The inversion degree (δ) is defined by the fraction of T_d sites occupied by the trivalent ion, which is Fe^{3+} in the case of $ZnFe_2O_4$. The authors used Rietveld refinement to show that δ increased from 0.13 to 0.30 when the annealing temperature was decreased from 800 °C to 600 °C. The authors also showed that a higher degree of spinel inversion resulted in superior majority charge carrier transport properties, and, therefore, a higher η_{sep}. For example, the η_{sep} of $ZnFe_2O_4$ annealed at 600 °C (17%) was considerably higher than that of $ZnFe_2O_4$ annealed at 800 °C (8%) at 1.23 V vs. RHE. The authors postulated that the conductivity of $ZnFe_2O_4$ is likely based on small polaron hopping, and changes in the electronic structure that accompany the normal-inverse spinel transition could aid charge transport via a hopping mechanism. The $ZnFe_2O_4$ sample with δ = 0.30 generated photocurrent densities of 0.8 mA/cm^2 and 1.0 mA/cm^2 at 1.23 V vs. RHE in pH 14 NaOH without and with the addition of a $NiFeO_x$ OEC, respectively. These photocurrent densities are the highest obtained for $ZnFe_2O_4$ used as a single photon absorber for solar water oxidation. This study demonstrates that the factors affecting small polaron-based charge transport can be significantly different from those affecting charge transport through the conduction band. (Structural disorder is generally known to be unfavorable for charge transport through the conduction band). This study also shows that understanding and improving small polaron-based charge transport is critical in improving the photoelectrochemical properties of oxide-based photoelectrodes.

Atomic doping, which increases the majority carrier density of a material, is another possible method to improve η_{sep}. Li and co-workers prepared Ti-doped $ZnFe_2O_4$ by spray pyrolysis followed by additional annealing steps where Ti^{4+} ions substitutionally replaced Fe^{3+} ions.[29] The authors showed a slight shift of the (220) peak in the XRD pattern to a higher two theta value as evidence for incorporation of Ti into the $ZnFe_2O_4$ lattice. The atomic percent of Ti present in the Fe site of the $ZnFe_2O_4$ lattice was determined to be 6% by XPS. The authors obtained a J-V plot for water oxidation in pH 14 NaOH and showed that the photocurrent density at 1.23 V vs. RHE improved from 0.05 to 0.35 mA/cm^2 by Ti doping, although the photocurrent onset potential was identical at 0.95 V vs. RHE. Mott-Schottky measurements showed that the carrier density of $ZnFe_2O_4$ increased upon Ti doping although no change of the E_{FB} (0.85 V vs. RHE) was observed.

Another effective way to increase η_{sep} is to deposit an extremely thin layer of $ZnFe_2O_4$ on a high surface area, wide-bandgap substrate (e.g. TiO_2 nanotube arrays,[31] Al-doped ZnO nanorod arrays[32]). For example, Kuang and co-workers deposited a thin layer of $ZnFe_2O_4$ (15 nm) on Al-doped ZnO nanowire arrays.[32] The diameter and thickness of the Al-doped ZnO nanowires were ~130 nm and ~7 μm, respectively. The resulting Al-doped ZnO and Al-doped ZnO/$ZnFe_2O_4$ nanowires generated photocurrent densities of 0.30 mA/cm^2 and 1.72 mA/cm^2, respectively, at 1.23 V vs. RHE in pH 6.5 Na_2SO_4. This means that most of the photocurrent (~1.42 mA/cm^2) was generated by the $ZnFe_2O_4$ layer. This value, which was obtained without the use of an OEC, is significantly higher than the photocurrent obtained by $ZnFe_2O_4$ electrodes deposited on typical 2D conducting substrates. $ZnFe_2O_4$ has also been used as an overlayer on other photoanodes. For example, it has been combined with Fe_2O_3 to enhance electron-hole separation[33, 34] and with

$BiVO_4$ to increase the stability of $BiVO_4$ in basic media while simultaneously increasing light absorption.[35]

Decreasing surface recombination is another possible strategy to improve the performance of $ZnFe_2O_4$. Choi and co-workers showed that an Al treatment can be an effective way to passivate the surface of $ZnFe_2O_4$.[34] The Fe^{3+} ions exposed on the surface of $ZnFe_2O_4$ have imperfect coordination environments, which can generate surface states that facilitate surface recombination.[36] The authors postulated that forming a thin $ZnFe_{1-x}Al_xO_4$ solid solution layer on the surface could provide a means to reduce the number of Fe^{3+} ions exposed at the surface. The authors tested this postulation using a $Fe_2O_3/ZnFe_2O_4$ composite electrode where $ZnFe_2O_4$ served as an overlayer. The Al_2O_3 surface layer was added by drop-casting an aqueous $Al(NO_3)_3$ solution on the $Fe_2O_3/ZnFe_2O_4$ electrode followed by annealing in air at 520 °C. The excess Al_2O_3 was then removed by soaking in 1 M NaOH. The J-V plots for water oxidation by the $Fe_2O_3/ZnFe_2O_4$ electrodes performed in pH 14 NaOH showed that the photocurrent density at 1.23 V vs. RHE was improved from 0.04 to 0.30 mA/cm^2 by the Al treatment. When Co^{2+} ions were adsorbed on the surface of the Al-treated $Fe_2O_3/ZnFe_2O_4$ to serve as an OEC, the photocurrent density at 1.23 V vs. RHE increased to 0.39 mA/cm^2, and the photocurrent onset was shifted from 0.85 to 0.65 V vs. RHE.

To elucidate the major differences between $ZnFe_2O_4$ and Fe_2O_3 photoanodes, Bein and co-workers prepared 20 nm-thick $ZnFe_2O_4$ and Fe_2O_3 films by atomic layer deposition (ALD) followed by annealing at 600 °C.[28] The E_{FB} and carrier densities of the resulting films were 0.64 V vs. RHE and 2×10^{17} cm^{-3} for $ZnFe_2O_4$ and 0.75 V vs. RHE and 2×10^{18} cm^{-3} for Fe_2O_3. Although the carrier density of $ZnFe_2O_4$ was lower than that of Fe_2O_3, it possessed a more negative E_{FB}, probably because the CBM of $ZnFe_2O_4$ is located above that of Fe_2O_3. The J-V plots for water oxidation measured in pH 13 NaOH showed that while the photocurrent onset potential of $ZnFe_2O_4$ (0.9 V vs. RHE) was more negative than that of Fe_2O_3 (1.1 V vs. RHE), the photocurrent density at 1.23 V vs. RHE of $ZnFe_2O_4$ (0.05 mA/cm^2) was considerably lower than that of Fe_2O_3 (0.24 mA/cm^2). The UV-Vis absorption spectra showed that although $ZnFe_2O_4$ and Fe_2O_3 have comparable bandgaps, the absorbance of $ZnFe_2O_4$ was significantly lower in the visible region (Figure 4), suggesting that poor photon absorption by $ZnFe_2O_4$ is the major reason for its lower photocurrent density. (The lower carrier density of the $ZnFe_2O_4$ film compared to the Fe_2O_3 film used in this study could have also made a contribution to its lower photocurrent generation). Additionally, intensity-modulated photocurrent spectroscopy (IMPS) was used to compare the charge transfer properties of these two compounds for water oxidation. The results showed that the rates of charge transfer for water oxidation were comparable, while the rate of surface recombination of $ZnFe_2O_4$ was slower than that of Fe_2O_3. The room temperature carrier mobilities of $ZnFe_2O_4$ and Fe_2O_3 were previously reported to be 3×10^{-8} cm^2/V·s[37] and 6×10^{-6} cm^2/V·s,[38] respectively. These results suggest that the low mobility of $ZnFe_2O_4$ may be an additional factor that causes the photocurrent of $ZnFe_2O_4$ to be inferior to that of Fe_2O_3.

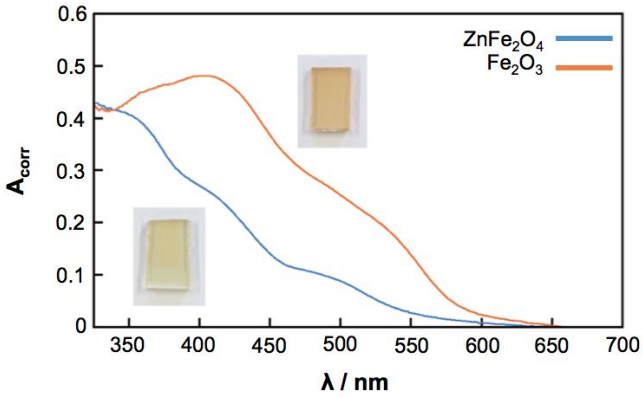

Figure 4. Reflectance-corrected absorbance (A_{corr}) spectra of ALD-deposited $ZnFe_2O_4$ and Fe_2O_3 films with corresponding photographs of the films. Adapted with permission from Ref. 28 John Wiley & Sons. Copyright 2016 WILEY-VCH Verlag GmbH & Co. KGaA, Weinheim.

Continuous improvement of the photoelectrochemical properties of $ZnFe_2O_4$ summarized here suggests that further enhancement of the performance of $ZnFe_2O_4$ may be achieved when multiple strategies are combined. However, remarkable improvements in the light absorption properties, bulk separation, and photocurrent onset potential will be necessary in order to consider using $ZnFe_2O_4$ as the primary photon absorber in a photoanode system.

$MgFe_2O_4$ and $CuFe_2O_4$ $MgFe_2O_4$ is an n-type oxide that also possesses a spinel structure with a bandgap of 2.0 − 2.2 eV.[16] However, only a few studies investigating the performance of $MgFe_2O_4$ as a photoanode have been reported to date.[21, 39-41] These reports include studies using $MgFe_2O_4$ as an overlayer on Fe_2O_3[40] and as an n-type layer on p-type $CaFe_2O_4$ to form a heterojunction.[41] Therefore, there is limited information available about the properties of $MgFe_2O_4$ used as a single photon absorber. The CBM of $MgFe_2O_4$ has been confirmed to be more negative than 0 V vs. RHE by both Mott-Schottky measurements and by detection of H_2 produced by $MgFe_2O_4$ when it was used as a photocatalyst.[42]

$CuFe_2O_4$ is another n-type oxide and its bandgap has been reported to be 1.3 - 1.5 eV.[16] $CuFe_2O_4$ has a disordered spinel structure where Cu^{2+} and Fe^{3+} ions readily occupy both T_d and O_h sites.[43, 44] The degree of inversion can vary depending on the synthesis method. The CBM of $CuFe_2O_4$ was also confirmed to lie above 0 V vs. RHE by detection of H_2 produced by $CuFe_2O_4$ when it was used as a photocatalyst.[45]

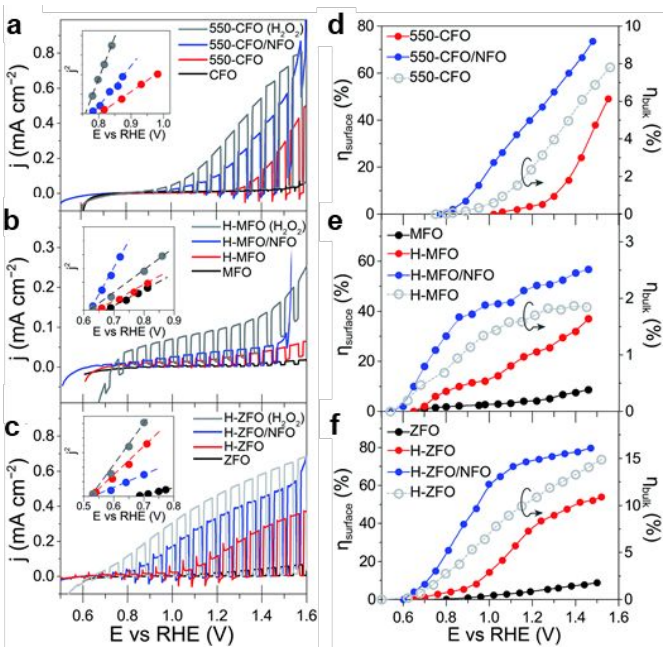

Figure 5. Photoelectrochemical properties of $CuFe_2O_4$ (CFO), $MgFe_2O_4$ (MFO), and $ZnFe_2O_4$ (ZFO) in pH 14 NaOH, where H, 550, and NFO represent H_2 heat treatment, annealing in air at 550 °C, and the addition of a $NiFeO_x$ OEC, respectively: (a-c) J-V plots obtained in pH 14 NaOH under AM 1.5G illumination with Butler plots (J^2 vs. E) shown as insets. For H_2O_2 oxidation, 0.5 M H_2O_2 was dissolved in the solution. (d-f) Efficiencies for bulk charge separation ($\eta_{bulk} = \eta_{sep}$) and the interfacial hole transfer reaction ($\eta_{surface} = \eta_{ox}$). Adapted with permission from Ref. 25. Copyright 2018 The Royal Society of Chemistry.

In a paper mentioned previously in the $ZnFe_2O_4$ section, Sivula and co-workers compared the photoelectrochemical properties of $MgFe_2O_4$ and $CuFe_2O_4$ with those of $ZnFe_2O_4$ (Figure 5).[25] To prepare their electrodes, FeOOH films were used as precursor films and the second metal atom was incorporated by drop-casting a solution containing Mg, Cu, or Zn ions followed by annealing. After forming the desired spinel compounds, the excess oxides were removed by soaking the films as follows: MgO and CuO were dissolved in 7 M HNO_3 and ZnO was dissolved in 5 M NaOH. The authors then annealed the $CuFe_2O_4$ films in air at 550 °C to improve crystallinity and annealed the $MgFe_2O_4$ and $ZnFe_2O_4$ films at 200 °C under H_2 flow to increase the carrier density by increasing oxygen vacancies, which was confirmed by XPS O 1s spectra.

The authors determined the indirect bandgaps of $MgFe_2O_4$ and $CuFe_2O_4$ to be 2.0 eV and 1.3 eV, respectively. When H_2O_2 was used as a hole scavenger, $MgFe_2O_4$ and $CuFe_2O_4$ generated photocurrent densities of 0.10 mA/cm^2 and 0.30 mA/cm^2, respectively, at 1.23 V vs. RHE in pH 14 NaOH. Based on these results, the η_{sep} at 1.23 V vs. RHE was determined to be 2% for $MgFe_2O_4$ and 3% for $CuFe_2O_4$ (Figure 5). These are both significantly lower than the η_{sep} of $ZnFe_2O_4$ (12%) reported in the same paper. The authors estimated the E_{FB} of $MgFe_2O_4$ to be ~0.65 V vs. RHE and the E_{FB} of $CuFe_2O_4$ to be ~0.8 V vs. RHE using the photocurrent onset potentials measured for H_2O_2 oxidation (i.e. construction of Butler plots using the J-V plots for H_2O_2 oxidation). It is not clear whether these positive E_{FB} values are due to insufficient doping levels or extremely fast surface recombination near the E_{FB}. If the latter is true, the injection rate

for H_2O_2 oxidation cannot be 100% in the potential region near the E_{FB} and the photocurrent onset potential does not accurately represent the E_{FB}.

Lastly, the water oxidation photocurrent densities at 1.23 V vs. RHE were 0.02 mA/cm^2 for $MgFe_2O_4$ and 0.01 mA/cm^2 for $CuFe_2O_4$. After the deposition of a $NiFeO_x$ OEC, the photocurrent densities increased to 0.04 mA/cm^2 and 0.15 mA/cm^2 for $MgFe_2O_4$ and $CuFe_2O_4$, respectively, at 1.23 V vs. RHE in pH 14 NaOH. Based on these results, the η_{ox} was calculated to be 50% for $MgFe_2O_4$ and 43% for $CuFe_2O_4$ at 1.23 V vs. RHE after the addition of the $NiFeO_x$ OEC (Figure 5). The performances of $MgFe_2O_4$ and $CuFe_2O_4$ for water oxidation are summarized in Table 2.

Since the limitations of $MgFe_2O_4$ and $CuFe_2O_4$ are very similar to those of Fe_2O_3 and $ZnFe_2O_4$, which have been intensively studied as photoanodes, the various methods that have been proven to enhance the photoelectrochemical properties of Fe_2O_3 and $ZnFe_2O_4$ may be applied to enhance the photoelectrochemical properties of $MgFe_2O_4$ and $CuFe_2O_4$. The most critical task for the consideration of $MgFe_2O_4$ and $CuFe_2O_4$ as viable photoanodes is the identification of effective methods to improve their extremely poor bulk charge separation.

Table 2. Comparison of solar water oxidation performances of $MgFe_2O_4$ and $CuFe_2O_4$ photoanodes.

Electrode	Preparation method	Onset (V_{RHE})	J at 1.23 V_{RHE} (mA/cm^2)	Electrolyte	IPCE at 1.1 V_{RHE}, 400 nm	Stability
$MgFe_2O_4$/ $NiFeO_x$[25]	Drop-casting a Mg solution on FeOOH followed by annealing and H_2 heat treatment	0.64	0.04	pH 14 NaOH	3.5%	1 h stable
$CuFe_2O_4$/ $NiFeO_x$[25]	Drop-casting a Cu solution on FeOOH followed by annealing and H_2 heat treatment	0.80	0.15	pH 14 NaOH	4.0%	24 h stable

$BiFeO_3$ $BiFeO_3$ has a rhombohedrally distorted perovskite structure in which the displacements of the Bi, Fe, and O atoms in the distorted structure remove the center of symmetry and cause $BiFeO_3$ to be ferroelectric.[46]

The bandgap of $BiFeO_3$ is reported to be 2.4 − 2.6 eV based on Tauc plots; however, UV-Vis absorption spectra of $BiFeO_3$ commonly show the light absorption onset to be around 600 nm.[47-49] This suggests that its bandgap could be as low as 2.1 eV, although its absorption coefficient near the absorption onset region may be low. One paper reported the color of $BiFeO_3$ to be red-orange, providing additional support that $BiFeO_3$ may have a lower bandgap energy than reported.[50] An E_{FB} of n-type $BiFeO_3$ as negative as -0.30 V to 0 V vs. RHE has been reported based on Mott-Schottky measurements, indicating that the CBM of $BiFeO_3$ is much more negative than 0 V vs. RHE.[48, 49] These advantageous features encourage the investigation of $BiFeO_3$ as a photoanode material for solar water splitting.

Without the addition of any extrinsic dopants, both n-type and p-type $BiFeO_3$ have been obtained, suggesting that intrinsic defects responsible for both n-type doping and p-type doping can readily form in $BiFeO_3$. The defects that can lead to n-type doping include oxygen vacancies[51] while the defects that can lead to p-type doping include Bi vacancies.[52] This means that the doping type of $BiFeO_3$ is determined by which type of defects preferentially form using a

given synthesis condition. For example, $BiFeO_3$ electrodes prepared by pulsed laser deposition[49] and by sputtering[53] are reported to be n-type as prepared. On the other hand, $BiFeO_3$ electrodes prepared by chemical bath deposition[47, 54] and by low pressure-CVD[48] are reported to be p-type as prepared.

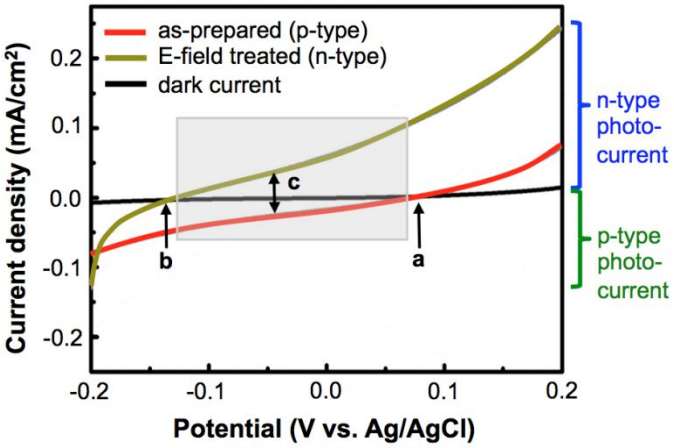

Figure 6. J-V plots of $BiFeO_3$ films in pH 7 Na_2SO_4 under illumination (power density not specified) before (red) and after (green) electric field treatment (i.e. applying -8 V vs. Ag/AgCl). The dark current is shown by the black line. (**a**: E_{FB} of as-prepared sample, **b**: E_{FB} of E-field-treated sample, **c**: arrow indicating the p-to-n conversion caused by the E-field-treatment. It should be noted that both the as-prepared and E-field-treated samples show p-to-n conversion within a single scan at the location of their E_{FB}s. Also, outside of the shaded area, the E-field-treatment does not result in p-to-n conversion). Adapted with permission from Ref. 47. Copyright 2016 American Institute of Physics Publishing LLC.

It has also been reported that the ferroelectric nature of $BiFeO_3$ allows the band bending at the $BiFeO_3$/electrolyte interface to flip (i.e. upward to downward or downward to upward) upon the application of an electric field resulting in n-to-p (or p-to-n) conversion.[47, 49, 54, 55] However, it is not clear whether the observed n-to-p (or p-to-n) conversion upon the application of an electric field is truly caused by the ferroelectricity of $BiFeO_3$. It is possible that the observed conversion may be caused by the creation of more defects that can serve as donors or acceptors during the application of the electric field, which altered the majority carrier type. If the as-prepared $BiFeO_3$ is very lightly doped and the E_{FB} is located near the middle of its bandgap, the conversion between n-type and p-type behaviors may be observed even with a small change in acceptor or donor concentration. In fact, some studies reporting n-to-p (or p-to-n) conversion of $BiFeO_3$ when an electric field was applied showed both n- and p-type behavior, which is demonstrated as a switching of the sign of the photocurrent (i.e. cathodic to anodic or anodic to cathodic) during a single potential sweep prior to the application of the electric field (Figure 6).[47, 49, 54] This behavior is typically observed with a very lightly doped semiconductor. After applying an electric field, the resulting samples also showed a change in the sign of the photocurrent during a single potential sweep (Figure 6), which means that even the electric field-treated samples are still very lightly doped. The only obvious change observed after the electric field treatment was a shift in the potential where the cathodic to anodic photocurrent conversion occurred (equivalent to the E_{FB}) (Figure 6).[47, 49, 54] (When n-to-p conversion was observed the E_{FB} was shifted to the positive direction and when p-to-n conversion was observed the E_{FB} was shifted to the negative direction.) We note that increasing the carrier density by applying a

potential (or an electric field) to a photoelectrode to create more defects has been achieved even when the photoelectrode is not ferroelectric.[56] Also, if the n-to-p (or p-to-n) conversion is achieved solely by flipping of the band bending associated with the ferroelectricity, it should be confirmed that the E_{FB} before and after applying the electric field remains unchanged. Therefore, more careful and systematic studies will be necessary to support the claim that the ferroelectricity of $BiFeO_3$ is the reason that n-to-p (or p-to-n) conversion of $BiFeO_3$ can easily change when an electric field is applied.

While the bandgap and band positions of $BiFeO_3$ look promising, there have been only a few studies investigating the photoelectrochemical properties of $BiFeO_3$.[47-49, 54, 55] The highest performing n-type $BiFeO_3$ showed a water oxidation photocurrent density of 0.17 mA/cm^2 at 0.85 V vs. RHE in a pH 6 Na_2SO_4 solution with a photocurrent onset potential of 0.15 V vs. RHE.[49] The highest performing p-type $BiFeO_3$ showed a water reduction photocurrent density of -0.05 mA/cm^2 at 0.10 V vs. RHE in a pH 6 Na_2SO_4 solution with a photocurrent onset potential of 0.55 V vs. RHE.[49] The photostability of n-type $BiFeO_3$ for water oxidation has also been demonstrated in pH 6 and pH 9 electrolytes by Moniz and co-workers.[48] The authors showed that when combined with a Ni borate OEC, n-type $BiFeO_3$ generated a photocurrent density of 0.6 mA/cm^2 at 1.7 V vs. RHE for 3 h. Evolved H_2 and O_2 gases were collected during the stability test, and Faradaic efficiencies for H_2 and O_2 evolution were calculated to be 85% and 70%, respectively.

The results obtained for $BiFeO_3$ so far clearly show that $BiFeO_3$ is an interesting compound that has the potential to be used as a photoelectrode with significant room for improvement. Most studies of $BiFeO_3$ to date have focused primarily on demonstrating switching of the doping type; however, facile conversion of the doping type means that both the as-prepared and converted $BiFeO_3$ electrodes are very lightly doped. The focus of future studies should lie in preparing optimally doped n-type or p-type $BiFeO_3$ to systematically assess its potential as a photoanode or photocathode for solar water splitting.

3-2. Metal Tungstates

$CuWO_4$ $CuWO_4$ is an extensively studied photoanode material with a bandgap of 2.2 − 2.3 eV. The α^{-1} of $CuWO_4$ has been reported as ~600 nm at λ = 450 nm by Hamann and co-workers.[57] The α^{-1} was determined from the UV-Vis absorption spectrum of an 80 nm-thick compact and smooth $CuWO_4$ film prepared by ALD. The authors noted that their measured α^{-1} value is shorter than a previously reported value (~2500 nm at λ = 450 nm)[58] and attributed this difference to different densities of the two films. The film with the longer light penetration depth was prepared by spray pyrolysis and was not a dense film.

$CuWO_4$ has several advantages when compared with WO_3. First, its bandgap is smaller than that of WO_3 (~2.6 eV), allowing utilization of a greater portion of visible light. The reduction in bandgap results from an upward shift of the VBM caused by the mixing of Cu 3d and O 2p orbitals, while the CBM remains similar to that of WO_3 (Figure 7a).[58] Additionally, $CuWO_4$ is reported to be chemically and photoelectrochemically stable in pH 7 – 9, where WO_3 is not stable.[59-61] (WO_3 is stable only in strongly acidic solutions).[62] Figure 7b shows J-t plots obtained for $CuWO_4$ and WO_3 photoanodes in pH 7 borate buffer under at an applied potential of 1.23 V vs. RHE. Both films used in this study were prepared by electrodeposition. $CuWO_4$ showed stable photocurrent generation for 12 h, while WO_3 showed a continuous photocurrent

decay.[58, 61] The fact that $CuWO_4$ is stable during water oxidation even without the addition of an OEC suggests that either $CuWO_4$ is thermodynamically stable against photocorrosion or the rate of photocorrosion of $CuWO_4$ is considerably slower than the rate of water oxidation.

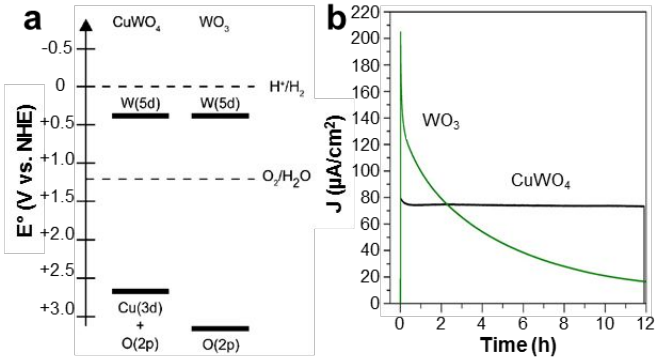

Figure 7. (a) Band diagrams for $CuWO_4$ and WO_3. Adapted with permission from Ref. 58. Copyright 2011 The Royal Society of Chemistry. (b) J-t plots of $CuWO_4$ and WO_3 photoanodes at 1.23 V vs. RHE in pH 7 borate buffer under AM 1.5G illumination. Adapted with permission from Ref. 61. Copyright 2016 American Chemical Society.

The fundamental limitation of $CuWO_4$ appears to be its extremely poor η_{sep}. Smith and co-workers examined photocurrent generation in pH 7 phosphate buffer using H_2O_2 as a hole scavenger and reported that the η_{sep} of their porous $CuWO_4$ film, which was prepared by spray pyrolysis, was only 3% at 1.23 V vs. RHE.[63] Considering that the oxidation of H_2O_2 can cause a current doubling effect, the actual η_{sep} may be even lower than this reported value.[64] Hamann and co-workers confirmed the current doubling effect of H_2O_2 by comparing photocurrents generated for the oxidation of H_2O_2 and sulfite in pH 9 borate buffer (Figure 8) using their ALD-deposited $CuWO_4$ electrodes.[65] Their results showed that the photocurrent obtained for H_2O_2 oxidation was much higher than the photocurrent obtained for sulfite oxidation. For example, the photocurrent densities at 1.23 V vs. RHE for the oxidation of H_2O_2 and sulfite were 0.29 mA/cm^2 and 0.16 mA/cm^2, respectively. The use of sulfite resulted in a shift of the onset potential from 0.85 to 0.6 V vs. RHE compared to water oxidation. However, although the sulfite oxidation photocurrent was enhanced in the low bias region (< 1.23 V vs. RHE), photocurrents for sulfite oxidation and water oxidation become comparable in the high bias region (> 1.23 V vs. RHE). This result suggests that the major challenge of using $CuWO_4$ as a photoanode is its extremely poor η_{sep}. Since the η_{ox} for water oxidation is not a serious limiting factor for $CuWO_4$, it is also expected that the use of an OEC will not drastically increase the photocurrent of $CuWO_4$ for water oxidation. Indeed, studies that report the combination of $CuWO_4$ with an OEC to achieve photocurrent enhancement have been very rare. Only an incremental increase in photocurrent for water oxidation has been observed when manganese phosphate was used as an OEC on a $CuWO_4$ or a $CuWO_4/WO_3$ composite photoanode.[61, 66]

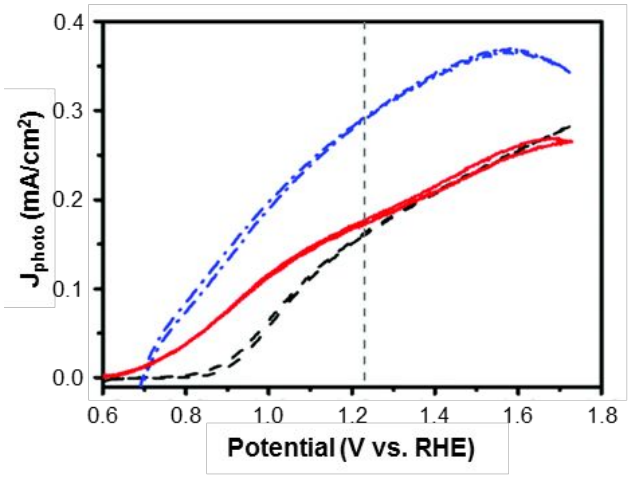

Figure 8. J–V plots of $CuWO_4$ for water oxidation (black), sulfite oxidation (red), and H_2O_2 oxidation (blue) in pH 9 borate buffer under AM 1.5G illumination. The vertical dashed gray line represents the thermodynamic potential for water oxidation (1.23 V vs. RHE). Adapted with permission from Ref. 65. Copyright 2017 The Royal Society of Chemistry.

As previously mentioned, one approach to increase η_{sep} is atomic doping, which can increase the carrier density and improve charge transport properties, thus improving electron-hole separation. Smith and co-workers introduced Fe^{3+} into the $CuWO_4$ lattice to substitute the octahedrally coordinated Cu^{2+} using a spray pyrolysis method.[63] The doped $CuWO_4$ showed an increase in photocurrent for both water oxidation (from 0.13 mA/cm^2 to 0.14 mA/cm^2) and H_2O_2 oxidation (from 0.27 mA/cm^2 to 0.42 mA/cm^2) at 1.23 V vs. RHE in pH 7 phosphate buffer. However, the exact role of the dopant was not confirmed in this study because no direct evidence was provided to confirm an increase in the charge carrier density of the doped sample. In addition to Fe^{3+}, Zn^{2+} and Co^{2+} have also been investigated as dopants to substitute Cu^{2+}, although the addition of these atoms has not been shown to improve the photoelectrochemical performance.[61, 67]

H_2-treatments have also been employed to increase the carrier density and η_{sep} of $CuWO_4$.[68, 69] For example, Diao and co-workers annealed their $CuWO_4$ film in a 5% hydrogen atmosphere (5% H_2 and 95% Ar) at 250 °C and observed an increase in the photocurrent density from 0.30 mA/cm^2 to 0.45 mA/cm^2 at 1.23 V vs. RHE in pH 7 phosphate buffer.[69] The authors confirmed that the carrier density was increased by 2.7 times using Mott-Schottky analysis, although the E_{FB} remained unchanged. They also used XPS to show that the oxygen vacancies generated by the H_2 treatment were accompanied by an increase in the concentration of W^{5+} in $CuWO_4$.

Other attempts to improve the performance of $CuWO_4$ have involved minimizing the bulk resistance of the material. For example, multi-walled carbon nanotubes (MWCNTs) were added to make composites with $CuWO_4$ to provide alternative conductive pathways for charge carriers.[70] In this study, $CuWO_4$ films were prepared by spray pyrolysis, and MWCNTs were added to the $CuWO_4$ precursor solution with a MWCNT:$CuWO_4$ ratio of 1:10,000 by weight. Although the addition of MWCNTs resulted in an enhancement of the photocurrent for water oxidation in pH 10 carbonate buffer solution, the degree of enhancement was not significant. (An increase from 0.20 mA/cm^2 to 0.225 mA/cm^2 at 1.23 V vs. RHE was observed).

Fabrication of nanostructured films with a particle size smaller than the charge carrier diffusion length is another important strategy to improve η_{sep}. The hole diffusion length of $CuWO_4$ was determined to be 30 nm by time-resolved microwave conductivity (TRMC) measurements of a $CuWO_4$ thin film grown by CVD.[71] The short carrier diffusion length of $CuWO_4$ provides a challenge when trying to design nanostructured materials that can effectively increase bulk charge separation. Several attempts have been made to develop high surface area $CuWO_4$ electrodes, including the conversion of nanostructured WO_3.[60, 69, 72] For example, Li and co-workers produced a $CuWO_4$ photoanode composed of vertically oriented $CuWO_4$ nanoflakes with dimensions of ~1 μm × ~1 μm × ~20 − 30 nm. This electrode showed the best performance among all undoped $CuWO_4$ photoanodes but the photocurrent density achieved by this sample for water oxidation in pH 9.5 borate buffer was still only ~0.4 mA/cm^2 at 1.23 V vs. RHE.[72]

A few groups have investigated the presence of surface states in $CuWO_4$ photoelectrodes as a possible cause for this low photocurrent generation. Bartlett and co-workers prepared a dense, polycrystalline $CuWO_4$ film by spin-coating a sol-gel precursor containing Cu and W and studied the presence of surface states using electrochemical impedance spectroscopy (EIS).[73] From Mott-Schottky analysis, the authors observed Fermi level pinning in the potential region of 0.81 − 1.01 V vs. RHE when low frequencies were used. This Fermi level pinning disappeared as the frequency was increased. The authors also observed that the Fermi level pinning was present both in the dark and under illumination in the same potential region. Based on these observations, the authors concluded that the Fermi level pinning was caused by the presence of permanent surface states in their $CuWO_4$, although the specific energetic locations of these states could not be determined. The authors discussed that the presence of these surface states can limit the rate of water oxidation and can also serve as recombination centers in the low bias region, thus delaying the photocurrent onset for water oxidation.

On the other hand, Hamann and co-workers reported that their $CuWO_4$ films prepared by ALD or spray pyrolysis commonly did not show Fermi level pinning in Mott-Schottky plots obtained in the dark or under illumination.[74] Instead, the authors used Bode plots, cyclic voltammetry (CV), and EIS analysis to show that surface states are formed only under electrochemical or photoelectrochemical water oxidation conditions. Based on these results, the authors concluded that surface states in their $CuWO_4$ electrodes are not intrinsic states but are formed due to water oxidation intermediates. The authors stated that recombination of these intermediate species with electrons in the conduction band of $CuWO_4$ is responsible for the difference in the photocurrent onset potentials for sulfite and water oxidation.

In addition to challenges related to bulk recombination and the presence of surface states, $CuWO_4$ has a relatively wide bandgap. Thus, an attempt to decrease the bandgap of $CuWO_4$ has been made to improve photon absorption. Choi and co-workers formed solid solutions of $CuWO_4$ and $CuMoO_4$ and produced $CuW_{1-x}Mo_xO_4$ films by electrodeposition followed by annealing at 500 °C in air.[75] The $CuW_{0.35}Mo_{0.65}O_4$ photoanode showed a successful decrease in the bandgap from 2.3 eV to 2.0 eV. In addition to an increase in the photon absorption, the $CuW_{0.35}Mo_{0.65}O_4$ photoanode also showed enhanced photocurrent generation for water oxidation (e.g. 0.06 mA/cm^2 for $CuWO_4$ and 0.15 mA/cm^2 for $CuW_{0.35}Mo_{0.65}O_4$ at 1.23 V vs. RHE in pH 7 phosphate buffer). However, using density functional theory (DFT) calculations, the authors showed that Mo doping decreases the bandgap by lowering the CBM of $CuWO_4$, rather than raising the VBM, which is thermodynamically unfavorable for solar H_2 production. Therefore,

the authors concluded that the bandgap reduction achieved by $CuW_{1-x}Mo_xO_4$ is not desirable for solar water splitting applications.

The results and understanding of $CuWO_4$ provided to date suggest that unless new strategies are developed to drastically increase η_{sep} of $CuWO_4$, further improving the photoelectrochemical properties of $CuWO_4$ for use as a single photon absorber will be challenging. Also, when compared with ternary metal ferrites that have the same bulk separation problem, both the CBM and bandgap of $CuWO_4$ are less favorable, making $CuWO_4$ less promising for future development as a photoanode.

α-$SnWO_4$ α-$SnWO_4$ has several attractive features for use as a photoanode; it possesses a bandgap of 1.64 − 2.1 eV[76-79] and it has a favorable α^{-1} of ~70 nm at λ = 450 nm.[77] The α^{-1} value was determined based on the UV-Vis transmittance and reflectance spectra of a dense and smooth 180 nm-thick α-$SnWO_4$ film prepared by DC magnetron sputtering. The E_{FB} determined using Mott-Schottky analysis is reported to be -0.14 V − 0 V vs. RHE.[78-80] This confirms that the CBM of α-$SnWO_4$ lies at a more negative potential than 0 V vs. RHE, which is advantageous for application in a water splitting PEC.

Despite the benefits outlined above, α-$SnWO_4$ has not yet shown promising photocurrent generation. Rao and co-workers compared the photocurrent for water oxidation and sulfite oxidation using nanoporous α-$SnWO_4$ electrodes prepared by hydrothermal conversion of WO_3 in an aqueous $SnCl_2$ solution.[79] The photocurrent generated by this electrode for sulfite oxidation was very low and was similar to that observed for water oxidation (0.08 mA/cm^2 at 1.23 V vs. RHE, pH 7 phosphate buffer) (Figure 9a). The negligible difference between the sulfite and water oxidation photocurrents suggests that the major limitation of α-$SnWO_4$ is not surface recombination but bulk recombination.

One difficulty in producing high quality α-$SnWO_4$ photoelectrodes is that α-$SnWO_4$ contains Sn^{2+}, which can be easily oxidized to Sn^{4+}. It has been reported that Sn^{4+} defects can behave as electron traps in Sn^{2+}-containing metal oxide photocatalysts, decreasing their photocatalytic activity.[79-82] Therefore, the use of an inert or vacuum atmosphere during annealing is necessary to produce highly crystalline α-$SnWO_4$.[76, 79, 83] Even when inert conditions such as Ar or N_2 atmospheres were used for annealing during the solid state syntheses of α-$SnWO_4$ powders, Mössbauer spectroscopy[83] and XPS[78] studies have revealed the presence of Sn^{4+} in the α-$SnWO_4$ samples. Therefore, special care is necessary to avoid the production of Sn^{4+} impurities or defects during the synthesis of α-$SnWO_4$.

In addition to challenges associated with Sn^{2+} oxidation during synthesis, some studies have reported that electrochemical oxidation of Sn^{2+} to Sn^{4+} can also readily occur in aqueous solutions.[76, 79] For example, Rao and co-workers and Bartlett and co-workers used nanoporous α-$SnWO_4$ films prepared by hydrothermal methods and reported that nonzero dark current was present in their J-V plots obtained in pH 7 phosphate buffer or pH 5 phosphate buffer, respectively, under chopped illumination (Figure 9a and 9b). The authors claimed that this may be due to the electrochemical oxidation of Sn^{2+} in α-$SnWO_4$. However, Takanabe and co-workers did not observe such dark current (Figure 9c) in a J-V plot obtained in 0.2 M sulfate (pH 3) for their dense and highly crystalline α-$SnWO_4$ film, which was prepared by DC magnetron sputtering followed by annealing at 600 °C in a N_2 environment.[80] The discrepancy in these studies suggests that the electrochemical instability of Sn^{2+} in the α-$SnWO_4$ lattice may not be an intrinsic problem of α-$SnWO_4$ and can be affected considerably by the quality of the film (i.e. crystallinity, surface defects). It may also be possible that the electrochemical dark current

observed by other groups may be due to the oxidation of Sn^{2+} in other Sn^{2+}-containing impurities, rather than the oxidation of Sn^{2+} in the α-$SnWO_4$ lattice.

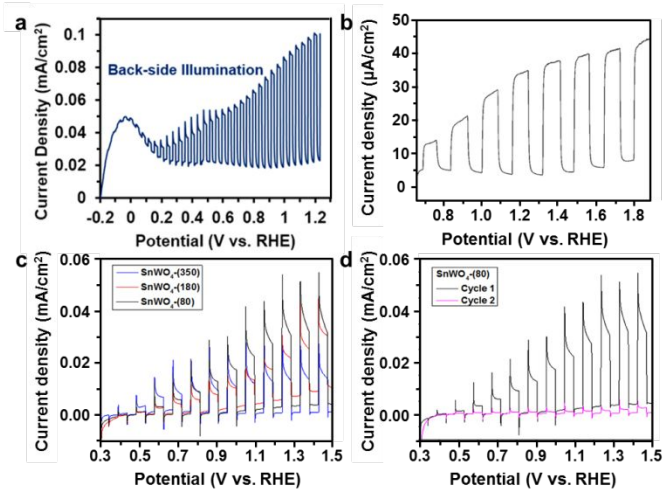

Figure 9. Chopped light J-V plots of α-$SnWO_4$ prepared by (a) Rao and co-workers measured in pH 7 phosphate buffer (Adapted with permission from Ref. 79. Copyright 2017 American Chemical Society), (b) Bartlett and co-workers measured in pH 5 phosphate buffer (Adapted with permission from Ref. 76. Copyright 2015 Elsevier), and (c) Takanabe and co-workers measured in a pH 3 sulfate solution. (d) Comparison between the first and second J-V scans of α-$SnWO_4$ prepared by Takanabe and co-workers. For (c) and (d), the numbers in parentheses refer to the thicknesses of the films in nm. Adapted with permission from Ref. 80. Copyright 2015 American Institute of Physics Publishing LLC. All J-V plots were measured under AM 1.5G illumination.

The photostability of Sn^{2+} in α-$SnWO_4$ is another concern because the oxidation of Sn^{2+} to Sn^{4+} may occur by photogenerated holes during photoelectrochemical water oxidation. For example, Takanabe and co-workers showed a significant decrease in the photocurrent for water oxidation after one LSV sweep under illumination. They attributed this decrease to the generation of Sn^{4+} during the first sweep, which can act as an electron trap site during subsequent sweeps (Figure 9d).[80] Rao and co-workers investigated the anodic photocorrosion of α-$SnWO_4$ by monitoring changes in photocurrent generation during three consecutive LSV sweeps under illumination.[79] They used three different electrolytes: aqueous pH 7 phosphate buffer, an aqueous solution containing $Fe(CN)_6^{4-/3-}$, and anhydrous acetonitrile containing 1 M $LiClO_4$ as a supporting electrolyte (Figure 10). The degree of surface oxidation of Sn^{2+} to Sn^{4+} was measured from the Sn $3d_{5/2}$ XPS spectra. The photocurrent for water oxidation measured in aqueous pH 7 phosphate buffer showed a significant decay between the first and third LSV sweeps, accompanied by the detection of a large amount of Sn^{4+} by XPS. However, photocurrent measured in an aqueous solution containing $Fe(CN)_6^{4-/3-}$ as a kinetically fast redox couple showed negligible photocurrent decay after three LSV sweeps. This result suggests that the photooxidation of Sn^{2+} on the α-$SnWO_4$ surface may not be a serious issue if α-$SnWO_4$ is coupled with an OEC that can increase the rate of water oxidation to be comparable to that of $Fe(CN)_6^{4-}$ oxidation. The authors also noted that the formation of Sn^{4+} in α-$SnWO_4$ did not occur in nonaqueous conditions, meaning that the oxidation of α-$SnWO_4$ requires the presence of water ($SnWO_4 + H_2O + 2h^+ \rightarrow SnO_2 + WO_3 + 2H^+$). This suggests that the addition of a protection

layer, which can prevent direct contact with water, may be an effective strategy to prevent photocorrosion of α-$SnWO_4$.

Judging from its bandgap, CBM, α^{-1}, and photocurrent onset potential, α-$SnWO_4$ has the possibility to become an efficient photoanode if methods to produce high quality α-$SnWO_4$ electrodes and strategies to effectively reduce bulk recombination in α-$SnWO_4$ can be developed.

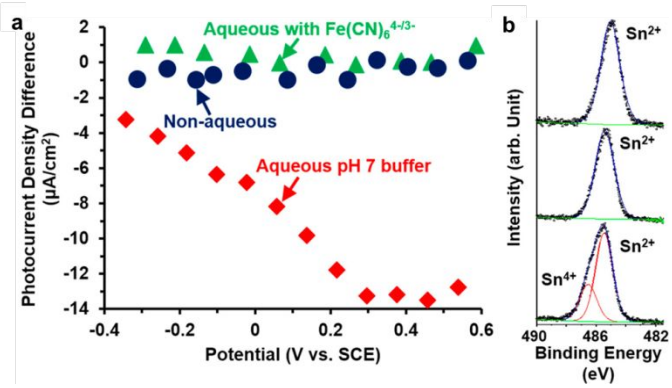

Figure 10. (a) Differences in photocurrent density at different applied potentials between the first and third LSV measurements of α-$SnWO_4$ under AM 1.5G illumination in aqueous pH 7 phosphate buffer, an aqueous electrolyte containing $Fe(CN)_6^{4-/3-}$, and nonaqueous anhydrous acetonitrile containing 1 M $LiClO_4$. (b) Sn $3d_{5/2}$ XPS spectra of α-$SnWO_4$ as-synthesized (top), after LSV measurements in the nonaqueous electrolyte (middle), and after LSV measurements in the aqueous electrolyte without a kinetically fast redox couple (bottom). Adapted with permission from Ref. 79. Copyright 2017 American Chemical Society.

Fe_2WO_6 Fe_2WO_6 is reported to have a favorable bandgap of 1.5 – 1.7 eV; however, there are only a few studies reporting its performance as a photoanode.[84, 85] Although this bandgap is well-suited for solar water splitting, Fe_2WO_6 has several limitations that may ultimately prevent its use as a photoanode for a water splitting PEC. Abdi and co-workers synthesized Fe_2WO_6 thin films using spray pyrolysis and found that its E_{FB} lies at 0.6 − 0.65 V vs. RHE using Mott-Schottky analysis.[85] The authors also estimated the VBM to be ~1.7 eV below the Fermi level from ultraviolet photoelectron spectroscopy (UPS) measurements. Since the bandgap of their Fe_2WO_6 was measured to be 1.7 eV, these results indicate that the CBM lies very close to the Fermi level (0.6 − 0.65 V vs. RHE). This positive CBM position will fundamentally limit the photovoltage gain for water oxidation by Fe_2WO_6.

Another major limitation of Fe_2WO_6 is its long α^{-1} of 1000 nm at λ = 450 nm, which indicates that Fe_2WO_6 is not a good photon absorber.[85] This α^{-1} value was determined by UV-Vis measurements using dense, polycrystalline Fe_2WO_6 films prepared by spray pyrolysis. Furthermore, the η_{sep} and hole diffusion length of this Fe_2WO_6 film were determined to be only 5% and 10 nm, respectively.[85] Due to the unfavorably positioned band edges, poor light absorption properties, and severe bulk recombination, Fe_2WO_6 is not likely to be a promising photoanode candidate for a water splitting PEC.

3-3. $BiVO_4$

$BiVO_4$ is an n-type semiconductor with a bandgap of 2.4 − 2.5 eV that has proven to be one of the most promising photoanodes for use in a water splitting PEC. The CBM is located at ~0 V vs. RHE, which is favorable for H_2 evolution.[15] $BiVO_4$ has been reported to have an E_{FB} as negative as ~0.1 V vs. RHE.[20, 86-92] Additionally, a photocurrent onset potential as negative as ~0.25 V vs. RHE has been demonstrated for water oxidation when $BiVO_4$ was combined with an OEC.[20, 86-91, 93-96] A photocurrent onset of 0.25 V vs RHE is equivalent to achieving a photovoltage of ~1 V for water oxidation. Photoanodes with a bandgap that can utilize visible light and achieve such a high photovoltage for water oxidation are rare. Because of this favorable photocurrent onset potential, $BiVO_4$ can achieve unassisted solar water splitting even when it is combined with an inexpensive single junction photocathode (e.g. p-Si, p-Cu_2O) whose photovoltage for water reduction is limited.[20, 97-99]

Another extraordinary feature of $BiVO_4$ is its exceptionally high η_{sep}. While typical oxide-based photoanodes demonstrate η_{sep}s of < 10% at 1.23 V vs. RHE, η_{sep} for $BiVO_4$ has been reported to be ≥ 90% at 1.23 V vs. RHE.[20, 87, 89] Even in the low bias region, $BiVO_4$ shows an exceptional η_{sep}, reaching as high as 70% at 0.6 V vs. RHE.[87] Additionally, $BiVO_4$ does not suffer from extremely fast surface recombination like many other oxide-based materials, meaning that all surface reaching holes can be used for sulfite oxidation. In other words, η_{ox} for sulfite oxidation can accurately be assumed to equal 1. As a result, the photocurrent onset for sulfite oxidation is very close to the E_{FB} of $BiVO_4$. (For oxides whose rate of surface recombination is faster than the rate of sulfite oxidation, the photocurrent onset potentials for sulfite oxidation are much more positive than their E_{FB}s). When $BiVO_4$ is combined with an OEC that can increase the rate of water oxidation to be equivalent to that of sulfite, the photocurrent onset for water oxidation also becomes very close to its E_{FB}. Another advantage of $BiVO_4$ is that although it is not thermodynamically stable against photocorrosion, its rate of photocorrosion is slow. This means that the photocorrosion of $BiVO_4$ can be kinetically suppressed as long as holes are quickly consumed by interfacial charge transfer reactions. Combined, these features make $BiVO_4$ an exceptional candidate for an oxide-based photoanode to be used in solar water oxidation. As a result, most recent PECs constructed to perform unassisted solar water splitting that generated sustainable photocurrent for at least 1 hour employed $BiVO_4$ as the sole photoanode or in conjunction with another photoanode.[20, 90, 93, 96-107] The configurations and performances of these PECs are summarized in Table 3. The most notable performances of $BiVO_4$ photoanodes for solar water oxidation where $BiVO_4$ was used as a single photon absorber are summarized in Table 4.

Table 3. STH efficiencies (η) achieved by $BiVO_4$-based PECs constructed for unassisted solar water splitting.

$BiVO_4$ photoanode	Coupled photocathode	Electrolyte	J_{op} (mA/cm^2)	STH η (%)	Stability
Si PV cells					

H_2-treated Mo-doped $BiVO_4$/ FeOOH/NiOOH with H_2-treated Ti-doped $Fe_2O_3/TiO_2/Ni_2FeO_x$[20]	Two 1-jn† Si	pH 9 carbonate	4.5 ($BiVO_4$) 3.2 (Fe_2O_3) 6.3 (together)	5.6 ($BiVO_4$) 3.9 (Fe_2O_3) 7.7 (together)	8 h stable
W-doped $BiVO_4$/Co-Pi[98]	2-jn† Si	pH 7 phosphate	4.2	5.2	1 h stable
W-doped $BiVO_4$/Co-Pi[97]	2-jn† Si 1-jn† Si	pH 7 phosphate	4.0 (2-jn) 3.0 (1-jn)	4.9 (2-jn) 3.6 (1-jn)	1 h stable
Perovskite PV cells					
Mo-doped $BiVO_4$/FeOOH/NiOOH on an inverse nanocone substrate[96]	$FA_{0.83}Cs_{0.17}PbI_2Br$	pH 7 phosphate	5.7	7.0	6 h stable
Mo-doped $BiVO_4$/FeOOH/NiOOH on a nanocone substrate[93]	$CH_3NH_3PbI_3$	pH 7 phosphate	5.0	6.2	10 h gradual decrease
H_2-treated Mo-doped $BiVO_4$/Co-Ci[90]	$CH_3NH_3PbI_3$	pH 9 carbonate	3.5	4.3	12 h stable
Metal oxide photocathode					
H_2-treated Mo-doped $BiVO_4$/ FeOOH/NiOOH[99]	$Cu_2O/Ga_2O_3/TiO_2$	pH 9 borate	2.5	3.0	12 h Stable

†1-jn and 2-jn stand for single junction and double junction, respectively.

Table 4. Comparison of solar water oxidation performances of $BiVO_4$ photoanodes where $BiVO_4$ was used as a single photon absorber.

Electrode	Preparation method	Onset (V_{RHE})	J at 1.23 V_{RHE} (mA/cm^2)	Electrolyte	Stability
$BiVO_4$/ FeOOH/NiOOH[87]	Electrodeposition of a BiOI film followed by annealing with a V solution	0.20	4.5	pH 7 phosphate	50 h stable
N_2-treated $BiVO_4$/ FeOOH/NiOOH[94]	Electrodeposition of a BiOI film followed by annealing with a V solution and post-treatment with N_2	0.24	4.7	pH 9 borate	450 h stable
$BiVO_4$/ $NiFeO_x$-B[95]	Electrodeposition of a BiOI film followed by annealing with a V solution	0.22†	4.9†	pH 9 borate	10 h stable

$BiVO_4$/ FeOOH/NiOOH[108]	Electrodeposition of an amorphous Bi film followed by annealing with a V solution	0.32†	5.9†	pH 9 borate	100 h stable
Mo-doped $BiVO_4$/ NiFeOOH[109]	Solid state reaction followed by ball milling and post annealing	0.28	3.8	pH 9 borate	1100 h stable
W-doped $BiVO_4$/ Co-Pi[98]	Spray pyrolysis followed by annealing	0.30	4.0	pH 7 phosphate	60 h stable
H_2-treated Mo-doped $BiVO_4$/ FeOOH/NiOOH[20]	Drop-casting followed by annealing and post-treatment with H_2	0.24	5.0	pH 9 carbonate	8 h stable
Mo-doped $BiVO_4$/ FeOOH/NiOOH on a nanocone substrate[93]	Drop-casting on a nanocone shaped glass/SiO_x/Pt/SnO_2 substrate followed by annealing	0.21	5.8	pH 7 phosphate	10 h gradual decrease
Mo-doped $BiVO_4$/ Fe(Ni)OOH on an inverse nanocone substrate[96]	Drop-casting on an inverse nanocone shaped glass/TiO_2/Pt/SnO_2 substrate followed by annealing	0.22	6.0	pH 7 phosphate	6 h stable

†Performances obtained by stacking two $BiVO_4$ films

Due to the unique and remarkable features of $BiVO_4$, which have enabled the generation of considerable photocurrent, $BiVO_4$ has been used as a model system to test various strategies to improve photoelectrochemical properties and stabilities of oxide-based photoanodes. For this reason, recent studies on $BiVO_4$ have provided a greater understanding of oxide-based photoelectrodes overall. Because we have previously reviewed the background of and progress made on $BiVO_4$ through 2013,[110] in this paper we chose to highlight the most significant developments made since 2013 in understanding and improving $BiVO_4$ photoanodes.

Morphology Tuning The effective hole diffusion length of pristine $BiVO_4$ is ~57 − 75 nm,[111-113] which is longer than that of many other oxides. Therefore, it should be relatively easy for $BiVO_4$ to achieve a high η_{sep} via nanostructuring. Choi and co-workers synthesized a high surface area porous $BiVO_4$ film (average particle size ~76 nm) using an electrodeposited BiOI film as the precursor film.[86, 87] An array of extremely thin BiOI plates were electrodeposited perpendicular to the FTO substrate with ample void space between the plates (Figure 11a). This BiOI film was converted to a $BiVO_4$ film by drop-casting a V-containing solution followed by annealing. During annealing, each BiOI plate formed multiple $BiVO_4$ particles that were interconnected with minimum grain boundaries between the particles, which ensured good electrical continuity all the way to the underlying FTO (Figure 11b-c). The void space between the BiOI plates in the pristine BiOI films ensured that the $BiVO_4$ particles formed from different BiOI sheets remained separate, resulting in the formation of high surface area $BiVO_4$ (31.8 m^2/g).[87] Any excess V_2O_5 formed during annealing was removed by dissolution in 1 M NaOH. The resulting $BiVO_4$ achieved η_{sep}s of 70 % and 90 % at 0.6 and 1.23 V vs. RHE, respectively.[87]

In a more recent study, Choi and co-workers modified the deposition conditions of BiOI to grow thicker and more densely packed BiOI plates (Figure 11d). This resulted in the formation of larger, columnar-type $BiVO_4$ particles (Figure 11e-f), which are more crystalline than the $BiVO_4$ particles discussed above. The average diameter of the particles (~110 nm) was still sufficiently small to maintain a high η_{sep} while the thick, dense-$BiVO_4$ film increased photon absorption per unit area of the film. As a result, an enhancement in the photocurrent density of $BiVO_4$ was observed (Figure 11g).[94] We found that most of the high-performing $BiVO_4$ films reported to date, which can generate a photocurrent density for sulfite oxidation of ~5 mA/cm^2 at 1.23 V vs. RHE, are commonly composed of $BiVO_4$ nanoparticles with an average particle size in the range of 100 nm – 200 nm.[20, 93, 94, 96, 108]

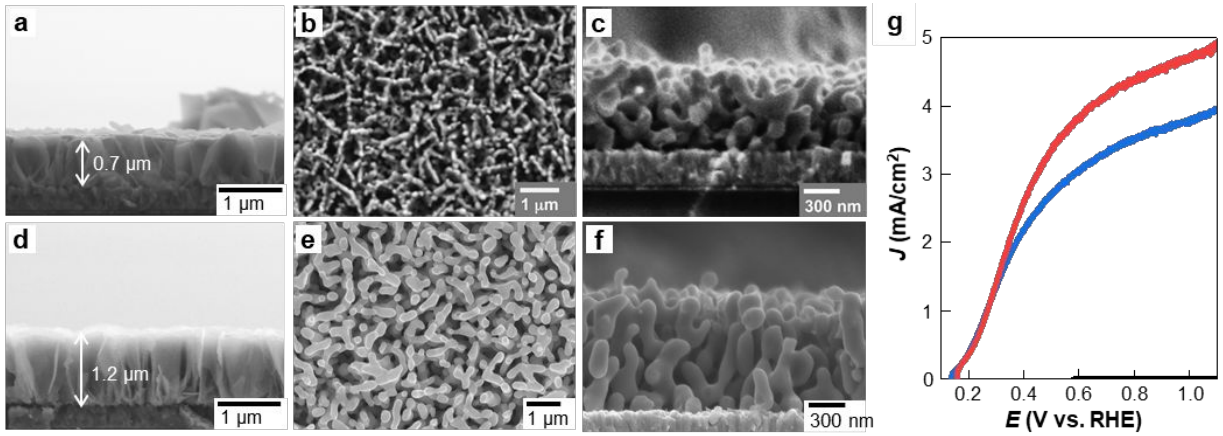

Figure 11. SEM images of (a) a BiOI precursor film on FTO (side view) and (b) top and (c) side view images of a $BiVO_4$ film obtained from the BiOI film. Adapted with permission from Ref. 87. Copyright 2014 American Association for the Advancement of Science. SEM images of (d) a thicker and more densely packed BiOI film and (e-f) a resulting $BiVO_4$ film. Adapted with permission from Ref. 94. Copyright 2018 Macmillan Publishers Limited, part of Springer Nature. (g) J-V plots of $BiVO_4$ films shown in b-c (blue) and e-f (red) for sulfite oxidation in pH 9 borate buffer containing 0.2 M sulfite under AM 1.5G illumination. The black line represents the dark current.

Increasing the Majority Carrier Density Atomic doping has been used to increase the majority carrier density of $BiVO_4$. The most commonly reported successful doping studies of $BiVO_4$ involve Mo^{6+} or W^{6+} doping into the V^{5+} site.[88, 97, 114-119] An optimum level of doping can increase the carrier density and thus the electrical conductivity of $BiVO_4$, resulting in an increase in η_{sep}. One interesting doping strategy reported by van de Krol and co-workers is gradient doping.[97] They demonstrated this concept using a dense, 200 nm-thick $BiVO_4$ film prepared by spray pyrolysis. They incorporated W^{6+} into their film with a doping level of 1% at the bottom and 0% at the top of the $BiVO_4$ film. Their goal was to allow band bending to extend across the entire thickness of the $BiVO_4$ film, thus increasing η_{sep}. The resulting film showed a η_{sep} of 60% at 1.23 V vs. RHE, which was significantly higher than that of the uniformly 1% W-doped $BiVO_4$ film (38 % at the same potential).

In addition to doping the V^{5+} site of $BiVO_4$, Choi and co-workers investigated a series of lanthanide (Ln) metal ions as dopants into the Bi^{3+} site.[120] The authors observed a systematic change in the size of the $BiVO_4$ lattice according to the size of the lanthanide ion incorporated

and also confirmed no change in morphology after doping, which is important to conduct a meaningful doping study. If the morphology of a doped sample is different from that of the pristine sample, it is extremely difficult to isolate the effect of doping. They reported that Sm and Yb doping resulted in photocurrent enhancement for both sulfite and water oxidation, while La and Ce doping resulted in the opposite effect. These effects were explained by changes in the electronic structure of the doped $BiVO_4$ samples compared to the pristine one, as elucidated by DFT calculations. To explain the experimental results observed for Sm and Yb doping, both Ln doping and O vacancies (the intrinsic defect of $BiVO_4$) needed to be considered simultaneously in the calculations. This suggests that understanding the interactions between intrinsic defects and extrinsic dopants may be important to more accurately understand the behavior of doped semiconductors.

Another commonly used method to increase the carrier density of $BiVO_4$ without introducing metal ion dopants is the use of post-synthesis gas treatments. For example, annealing $BiVO_4$ films in a H_2 atmosphere, referred to as H_2-treatment, has been reported to increase the carrier density and therefore the η_{sep} and photocurrent generation of $BiVO_4$.[113, 121, 122] A few studies reported that H_2 treatment of $BiVO_4$ can not only create O vacancies but also incorporate H atoms into the $BiVO_4$ lattice.[113, 122] Sharp and co-workers[122] and Abdi and co-workers[113] reported that the presence of H in O vacancies plays a critical role in the charge transport properties of H_2-treated $BiVO_4$. Abdi and co-workers attempted to create O vacancies without H incorporation using Ar treatment instead of H_2 treatment and did not observe any increase in photocurrent.[113] They concluded that O vacancies alone are not responsible for the observed photocurrent enhancement. However, the authors did not comment on whether Ar treatment was able to generate the same level of oxygen vacancies as H_2 treatment. Since Ar is an inert gas and may not interact with O in the $BiVO_4$ lattice in the same way as H_2 gas, it is possible that the concentration of O vacancies created by Ar treatment may have been significantly less than the concentration of O vacancies created by H_2 treatment. Therefore, it is not clear whether the difference in photocurrent obtained after Ar treatment and H_2 treatment was due to the incorporation of H in O vacancies or due to the different amounts of O vacancies created. In order to clearly isolate the effect of H incorporation into O vacancies, comparing the performances of $BiVO_4$ electrodes containing the same concentration of O vacancies with and without the presence of H will be necessary.

Abdi and co-workers also compared the charge transport properties of H_2-treated $BiVO_4$ and W-doped $BiVO_4$ (Table 5).[113] Their results showed that while both H_2 treatment and W doping commonly increased the majority carrier density, they had drastically different effects on other charge transport properties. The H_2 treatment marginally improved the mobility of both electrons and holes while significantly improving the hole lifetime. As a result, the diffusion length of the holes was greatly improved in the H_2-treated $BiVO_4$. In contrast, W doping decreased the mobility of both electrons and holes significantly and also decreased the lifetime of the holes, significantly decreasing the diffusion length of the holes. The authors explained that W ions in the $BiVO_4$ lattice can serve as recombination centers by trapping photogenerated charge carriers.

Table 5. Bulk charge transport properties of pristine, H_2-treated, and 1% W-doped $BiVO_4$ photoanodes.[113] (μ: carrier mobility, μ_e: electron mobility, μ_h: hole mobility, τ: carrier lifetime, L_h: carrier diffusion length, N_d: carrier density)

	μ ($cm^2\ V^{-1}\ s^{-1}$)	μ_e ($cm^2\ V^{-1}\ s^{-1}$)	μ_h ($cm^2\ V^{-1}\ s^{-1}$)	τ (ns)	L_h (nm)	N_d (cm^{-3})
$BiVO_4$	0.07	0.04	0.03	43	57	$7.0 \pm 1.7 \times 10^{18}$
H_2-$BiVO_4$	0.08	0.045	0.035	109	101	$1.1 \pm 0.3 \times 10^{21}$
W-$BiVO_4$	0.02	0.01	0.01	32	28	$2.9 \pm 0.8 \times 10^{21}$

Another method employed to increase O vacancies in $BiVO_4$ is N_2 treatment. Choi and co-workers treated their nanoporous $BiVO_4$ films using N_2 (350 °C for 2 h while flowing N_2) and observed an increase in the carrier density and a corresponding increase in η_{sep}.[89] They compared the properties of their N_2-treated sample with a H_2-treated sample and saw comparable effects on η_{sep}. Additionally, the authors observed that N_2 treatment resulted in nitrogen incorporation into the $BiVO_4$ lattice, which was confirmed by electron probe micro-analysis (EPMA) and XPS. This result is surprising because incorporation of nitrogen into an oxide lattice typically requires the use of NH_3 at much higher temperatures ($\geq$ 500 °C). However, nitrogen incorporation into mesoporous V_2O_5 by annealing under N_2 flow has been reported previously,[123, 124] suggesting a high affinity of mesoporous vanadium-containing oxides for nitrogen. The authors computationally showed that nitrogen incorporation can decrease the bandgap of $BiVO_4$ by raising the VBM, which is highly desirable for application in water splitting PECs (Figure 12a). The authors also experimentally confirmed a decrease of 0.2 eV in the bandgap by IPCE measurements (Figure 12b) and UV-Vis absorption spectra.

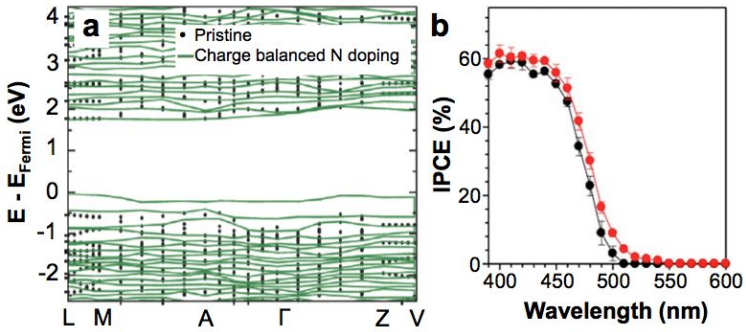

Figure 12. (a) Electronic band structure of pristine $BiVO_4$ and $BiVO_4$ with charge-balanced N doping (9% O replaced with 6% N and 3% O vacancies) (b) IPCE of $BiVO_4$ (black) and N_2-treated $BiVO_4$ (red) at 0.6 V vs. RHE in pH 7 phosphate buffer containing 1 M Na_2SO_3 showing a decrease in bandgap by 0.2 eV after N incorporation. Adapted with permission from Ref. 89. Copyright 2015 Macmillan Publishers Limited, part of Springer Nature.

Choi and co-workers also discussed the possibility that N incorporation can influence the charge carrier mobility of $BiVO_4$.[89] Electron transport in most oxide-based photoelectrodes, including $BiVO_4$, is achieved through small polaron hopping,[125] in which the transport of charge carriers also involves a deformation of the crystal lattice. The authors noted that N incorporation can change the static dielectric constant of $BiVO_4$, which would lower the activation energy of small polaron hopping and improve the polaron mobility. Since they did not directly measure a change in mobility, it is not clear whether this change in mobility truly contributed to the increased photocurrent generation caused by N doping. However, an important message

delivered by this work is that a dopant atom that is introduced into a host oxide material may have multiple effects that alter the photoelectrochemical properties of that material via different mechanisms. This study, along with the study by Abdi and co-workers comparing the effects of H_2 treatment and W doping,[113] illustrates that a comprehensive understanding of doping effects is critical to effectively control the charge transport properties of a photoanode by composition tuning.

To date, studies that have attempted to increase the mobility of small polarons have been rare. One interesting study reported by Chueh and co-workers showed the effect of temperature on the mobility of small polarons.[126] The authors compared photocurrent generation by Mo-doped $BiVO_4$ coupled with a CoPi OEC for water oxidation at various temperatures. As the temperature increases, the deformation of a crystal lattice becomes easier. This causes an increase in the polaron mobility, resulting in an increase in the photocurrent density (Figure 13). For example, increasing the temperature from 25 °C to 42 °C resulted in an increase in photocurrent from 2.6 to 4.0 mA/cm^2 at 1.0 V vs. RHE. It should be noted that for covalent semiconductors, such as Si, where the electrons are delocalized and transport occurs through the conduction band, the electron mobility decreases when the temperature increases due to enhanced phonon scattering.[127, 128] Therefore, an increase in mobility caused by an increase in temperature is unique for semiconductors in which charge transport occurs through small polaron hopping. The operating temperature of a PEC is expected to be greater than room temperature under solar illumination, which may be advantageous for PECs which use oxide-based photoelectrodes whose charge transport involves small polaron hopping.

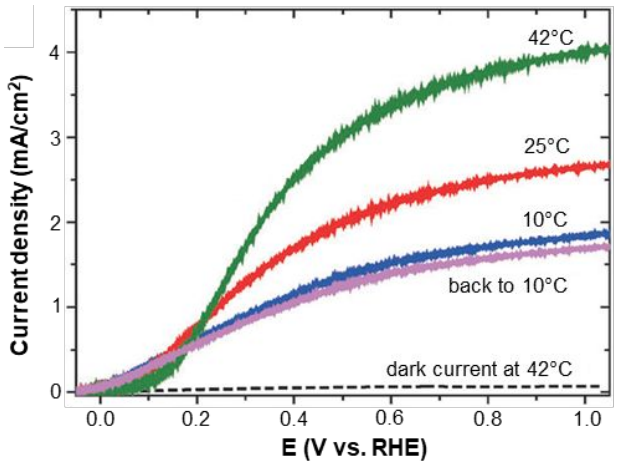

Figure 13. Temperature-dependent J-V plots of the CoPi/Mo:$BiVO_4$/SnO_2/Si photoanode in pH 7 phosphate buffer under AM 1.5G illumination. Adapted with permission from Ref. 126. Copyright 2016 The Royal Society of Chemistry.

Coupling with Oxygen Evolution Catalysts In general, the rate of water oxidation on the bare $BiVO_4$ surface is significantly slower than that of sulfite oxidation. After a few initial studies demonstrated that the photocurrent achieved by $BiVO_4$ for water oxidation could be considerably increased by the addition of OECs such as Co-Pi,[129] RhO_2,[118] and FeOOH,[130] various OECs have been coupled with $BiVO_4$ photoanodes.[131-134]

When an OEC is used as an electrocatalyst on a conducting substrate, it increases the rate of water oxidation only through an increase in the rate constant for water oxidation (k_{ox}). However, when an OEC is coupled with a photoanode to utilize photogenerated holes for water

oxidation, OECs can also increase the rate of water oxidation by increasing the number of holes available for water oxidation. This is achieved when an OEC improves bulk or surface electron-hole separation in some way. For instance, the OEC can serve as a hole sink, which affects the band bending of the photoanode, or it can decrease surface recombination by passivating surface states.[135-137] Broadly speaking, any compound that can increase the rate of water oxidation when coupled with a photoanode can be regarded as an oxygen evolution catalyst. However, some studies use the term "catalyst" only when the rate of water oxidation is increased through an increase in k_{ox}. Therefore, when a study states that an additional layer is not truly acting as an OEC, although the rate of water oxidation increases, this means that the rate of water oxidation is increased by a mechanism that does not involve an increase in k_{ox}.

Since the rate of photoelectrochemical water oxidation is affected not only by k_{ox} but also by the number of holes available for water oxidation, which can increase by decreasing the rate of surface recombination (k_{rec}), an OEC should be chosen while taking into account its effect on both k_{rec} and k_{ox}.[136, 138] For example, even if an OEC can increase k_{ox}, if it increases k_{rec} more drastically, a decrease in the rate of water oxidation may result. In the same manner, even if an OEC does not significantly increase k_{ox}, if it can effectively decrease k_{rec}, it can improve the rate of water oxidation. While k_{ox} is an intrinsic property of an OEC, k_{rec} depends critically on the interfacial structure at the photoanode/OEC junction. Therefore, even for one photoanode material, the optimum OEC may be different depending on the surface structure of the photoanode, which can be affected by the synthesis condition.

Choi and co-workers demonstrated the importance of minimizing recombination at the photoanode/OEC junction by comparing the effects of FeOOH and NiOOH OECs on water oxidation by a $BiVO_4$ photoanode.[87] (Figure 14) The authors showed that when tested as an electrocatalyst on a FTO substrate, NiOOH showed a better catalytic performance, meaning that NiOOH possessed a higher k_{ox} under their experimental conditions. However, when placed on $BiVO_4$, FeOOH performed better than NiOOH. The authors postulated that this is due to decreased recombination at the $BiVO_4$/FeOOH interface compared to the $BiVO_4$/NiOOH interface. This postulation was supported by comparing the photocurrents of $BiVO_4$/FeOOH and $BiVO_4$/NiOOH electrodes for sulfite oxidation. Since the rate of sulfite oxidation should be equally fast on $BiVO_4$, FeOOH, and NiOOH surfaces, a decrease in photocurrent observed after the addition of a FeOOH or NiOOH layer on $BiVO_4$ can only be due to loss of holes to recombination at the $BiVO_4$/OEC interface. The authors showed that the photocurrent for sulfite oxidation achieved by $BiVO_4$/NiOOH was significantly lower than that achieved by $BiVO_4$/FeOOH, confirming that FeOOH forms a better interface with $BiVO_4$ and thus experiences reduced interfacial recombination. The authors also prepared a $BiVO_4$/FeOOH/NiOOH photoanode, where FeOOH and NiOOH were deposited consecutively. This electrode performed better than $BiVO_4$/FeOOH and $BiVO_4$/NiOOH because it utilized the advantages of both OECs: the minimum recombination achieved by the $BiVO_4$/FeOOH interface and the fast water oxidation kinetics achieved by the NiOOH/electrolyte interface. The authors also constructed $BiVO_4$/NiOOH/FeOOH films to confirm that this electrode showed the worst performance due to opposite effects. As mentioned earlier, recombination at the photoanode/OEC junction depends on the surface structure of the photoanode (e.g. surface termination, surface composition). Therefore, we note that although FeOOH formed the best interface with the $BiVO_4$ synthesized by Choi and co-workers, this does not necessarily mean that FeOOH will be the best OEC for $BiVO_4$ with different surface terminations produced by other synthesis methods.

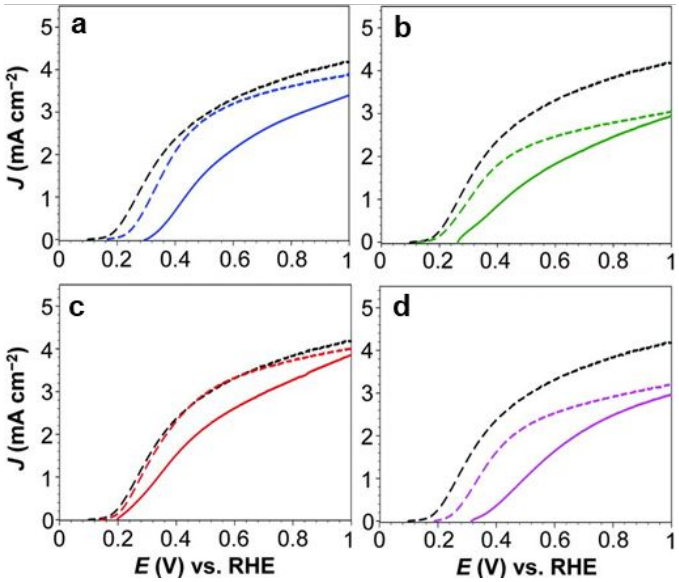

Figure 14. J-V plots of (a) $BiVO_4$/FeOOH, (b) $BiVO_4$/NiOOH, (c) $BiVO_4$/FeOOH/NiOOH, and (d) $BiVO_4$/NiOOH/FeOOH comparing photocurrent generation for 1.0 M sulfite oxidation (dashed) and water oxidation (solid) measured in pH 7 phosphate buffer. Photocurrent for sulfite oxidation achieved by bare $BiVO_4$ is shown as the black dashed line for comparison. All J-V plots were measured under AM 1.5G illumination. Adapted with permission from Ref. 87. Copyright 2014 American Association for the Advancement of Science.

Stability Stable operation of photoelectrodes is another critical factor to consider for the practical construction of PECs. According to the Pourbaix diagram constructed for $BiVO_4$, $BiVO_4$ is thermodynamically stable in the water stability region (0 − 1.23 V vs. RHE) between pH 1 and 11.[139] However, experimentally observed stabilities of $BiVO_4$ can vary depending on the sample quality. This is because V_2O_5 is a highly soluble oxide[62] and the solubility of any V-containing ternary oxide can be significantly affected by its crystallinity as well as its V content. Since the anodic photocorrosion of $BiVO_4$ involves its dissolution, and the dissolution is affected by the crystallinity of the electrode, the crystallinity of $BiVO_4$ is a critical factor that can affect its rate of photocorrosion. The $BiVO_4$ films used for solar water splitting applications are typically produced via low temperature annealing and are composed of nanocrystalline particles, meaning that they cannot have the perfect crystallinity of single crystalline $BiVO_4$. As a result, the chemical and photoelectrochemical stabilities of $BiVO_4$ can be seriously underestimated if the $BiVO_4$ films used for stability tests are not highly crystalline. One simple way to check the crystallinity of a sample is to calculate the crystalline domain size using the Scherrer equation based on the FWHM of XRD peaks. If the crystalline domain size calculated from the Scherrer equation is significantly smaller than the particle size observed by SEM, a significant portion of each $BiVO_4$ particle (i.e. the outer region of each particle) has poor crystallinity or is amorphous. These samples are expected to show poor chemical and photoelectrochemical stabilities.

Domen and co-workers demonstrated impressive photostability of Mo-doped $BiVO_4$ with a Ni-Fe OEC for over 1100 hours in 1.0 M borate buffer (pH 9) with a photocurrent density of 2.6 mA/cm^2 at 0.6 V vs. RHE.[109] The authors synthesized highly crystalline $BiVO_4$ particles (particle size ~300 − 500 nm) by annealing at 800 °C for 2 h, ball milling to crush the particles,

and re-annealing at 700 °C for 2 h. The resulting $BiVO_4$ showed excellent crystallinity and its XRD pattern showed well-resolved Bragg diffraction peaks even in the high two theta region (> 55°) (Figure 15). The authors showed that their highly crystalline $BiVO_4$ generated stable photocurrent at 1.23 V vs. RHE in pH 9 borate buffer for 2 hours without the use of an OEC. The authors also noted that a less crystalline $BiVO_4$ film that they used as a control sample did not show any signs of photocorrosion when the photocurrent was measured in pH 9 borate buffer at 0.6 V vs. RHE under AM 1.5G illumination or at 2 V vs. RHE in the dark. This suggests that the photoanodic dissolution of $BiVO_4$ occurs only under conditions where a considerable number of holes are generated and accumulate on the $BiVO_4$ surface. This also implies that the addition of an OEC that can minimize hole accumulation on the $BiVO_4$ surface is critical to achieve photostability. To attain longer-term photostability for water oxidation, the authors added a Ni-source (dissolved from the substrate) and a Fe-source (impurity from the electrolyte) to the PEC so that the Ni-Fe OEC could be deposited on $BiVO_4$ during water oxidation and continuously regenerated if the OEC layer was damaged during the test. Thus, the two critical factors enabling long-term operation were the high crystallinity of $BiVO_4$ and prevention of OEC loss during water oxidation.

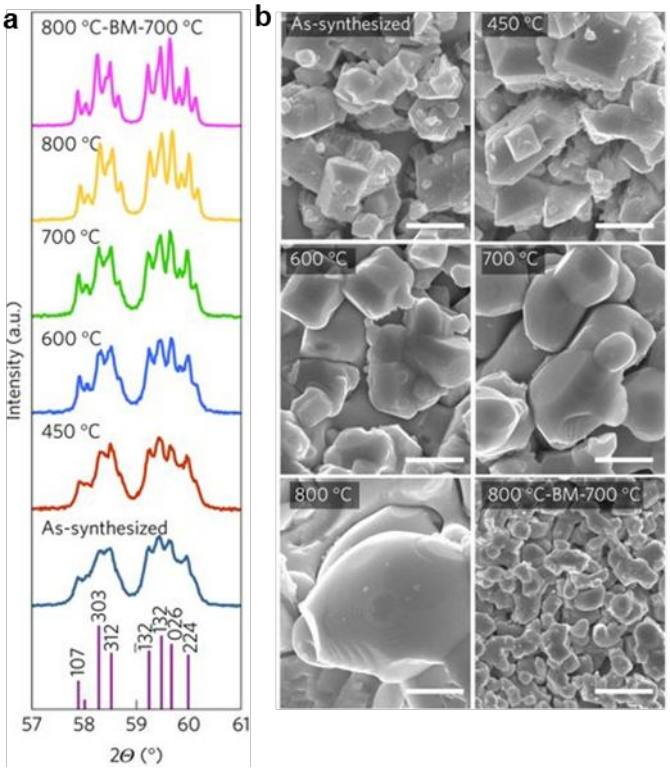

Figure 15. (a) XRD patterns of Mo-doped $BiVO_4$ particles annealed at different temperatures. BM stands for "ball milling." The miller indices of $BiVO_4$ (JCPDS, No. 83-1699) are shown at the bottom. (b) SEM images of the corresponding $BiVO_4$ particles (scale bar = 1 μm). Adapted with permission from Ref. 109. Copyright 2016 Macmillan Publishers Limited, part of Springer Nature.

Choi and co-workers performed a systematic investigation of the chemical stability, photoelectrochemical stability for sulfite oxidation, and photoelectrochemical stability for water oxidation using their nanoporous $BiVO_4$ photoelectrode.[94] The authors showed that their nanoporous $BiVO_4$ did not show any signs of chemical dissolution after being immersed in pH 9

borate solution in the dark for 2 months (Figure 16). Judging from the FWHMs of XRD peaks, the nanoporous $BiVO_4$ used in this study is very crystalline relative to $BiVO_4$ prepared from other methods. The authors also showed that $BiVO_4$ can achieve photostability for sulfite oxidation for 500 hours when operated at 0.6 V vs. RHE in pH 9 borate buffer (Figure 17a). However, $BiVO_4$ coupled with a FeOOH/NiOOH OEC showed photoanodic dissolution when water oxidation was performed under the same conditions for more than 50 hours. The authors noted that the photocurrent generated by $BiVO_4$/FeOOH/NiOOH for water oxidation was less than that generated by $BiVO_4$ for sulfite oxidation, meaning that $BiVO_4$/FeOOH/NiOOH did not utilize all of the surface-reaching holes for water oxidation. Thus, the slower rate of water oxidation compared to sulfite oxidation resulted in the accumulation of holes at the $BiVO_4$ surface, leading to photocorrosion.

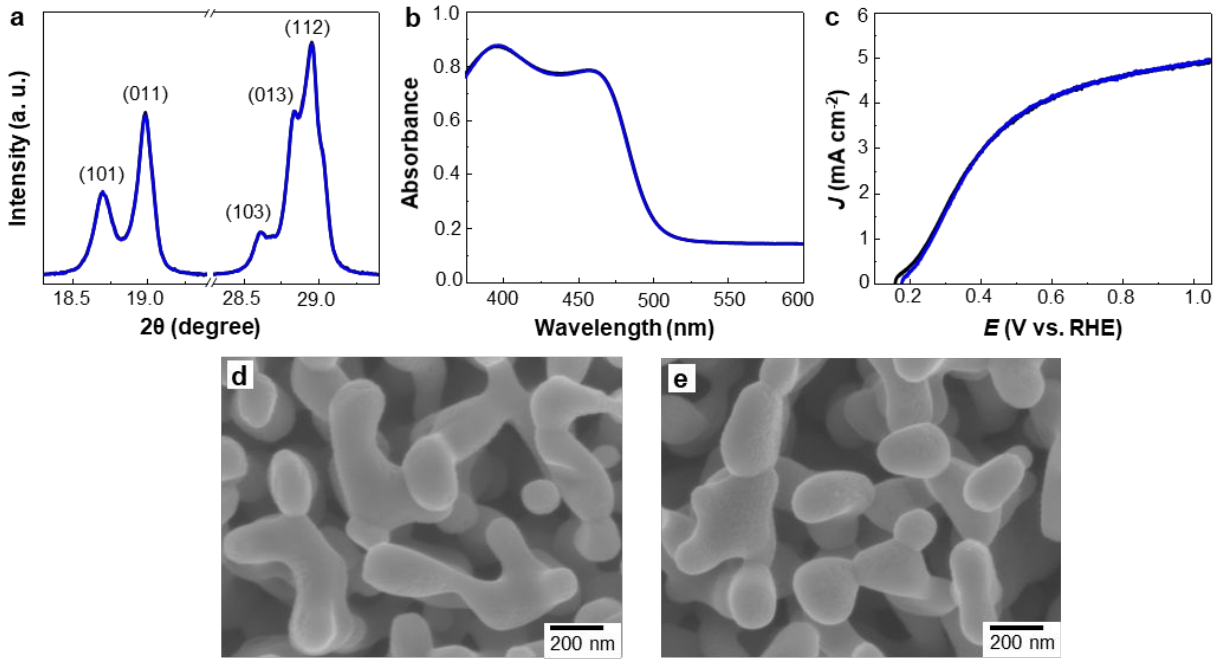

Figure 16. (a) XRD patterns, (b) UV-Vis spectra, and (c) photocurrent measurements for sulfite oxidation (0.2 M) of $BiVO_4$ in pH 9 borate buffer under AM 1.5G illumination before (black) and after (blue) immersion in pH 9 borate for 50 days in the dark. SEM images (d) before and (e) after immersion are also shown. Adapted with permission from Ref. 94. Copyright 2018 Macmillan Publishers Limited, part of Springer Nature.

When a photoanode is photostable for sulfite oxidation but not for water oxidation, the rate of photocorrosion is significantly slower than the rate of sulfite oxidation but faster than the rate of water oxidation. In this case, the photocorrosion of the photoanode can be kinetically suppressed if the surface-reaching holes can be consumed with a rate comparable to that for sulfite oxidation. Therefore, one way to enhance the photostability of $BiVO_4$ during water oxidation is to increase the rate of water oxidation to the level of sulfite oxidation by improving the OEC. We note that when a higher performing $BiVO_4$ photoanode is used, (i.e. greater number of surface-reaching holes) the prevention of photocorrosion during water oxidation becomes more difficult and requires a better OEC.

Another possible route to kinetically suppress photocorrosion is to force the rate of photocorrosion to be slower than the rate of water oxidation. When the rate of water oxidation is slower than the rate of sulfite oxidation, a fraction of the surface-reaching holes may accumulate at the surface. The accumulated holes can destabilize the $BiVO_4$ lattice at the surface, increasing its solubility and resulting in V leaching. Choi and co-workers postulated that V^{5+} loss may not be a consequence of photocorrosion but instead may serve as a key intermediate step in the photocorrosion of $BiVO_4$.[94] In other words, the loss of V^{5+} may facilitate the photooxidation of Bi^{3+} and/or lattice oxide ions in $BiVO_4$ by making reorganization around these ions easier. In this case, preventing V^{5+} leaching may be an effective strategy to slow the rate of $BiVO_4$ photocorrosion. The authors tested this postulation by using a V^{5+}-saturated electrolyte, which can suppress V^{5+} leaching by Le Châtelier's principle, and demonstrated stable generation of a photocurrent density of 3.2 mA/cm^2 at 0.6 V vs. RHE in pH 9 borate buffer over 450 hours (Figure 17b).[94]

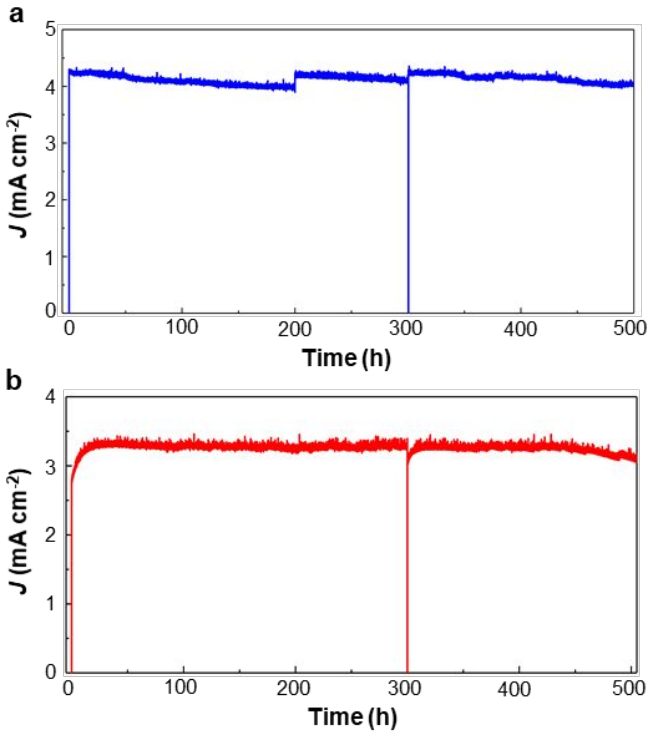

Figure 17. (a) J-t plot of $BiVO_4$ for sulfite oxidation at 0.6 V vs. RHE in pH 9 borate buffer containing 0.7 M Na_2SO_3. The slight photocurrent decrease observed over time was not due to photocorrosion but due to the depletion of sulfite. When the electrolyte was replenished at 200 h and 300 h, the photocurrent increased to its initial level. (b) J–t plot of the $BiVO_4$/FeOOH/NiOOH film in a V^{5+}-saturated pH 9 borate electrolyte at 0.6 V vs. RHE. Unlike the sulfite measurement where the electrolyte was replaced only twice over 500 h, the electrolyte was replenished every 24 h to maintain a constant photocurrent level. All measurements were performed under AM 1.5G illumination. Adapted with permission from Ref. 94. Copyright 2018 Macmillan Publishers Limited, part of Springer Nature.

Another major research focus for $BiVO_4$ has been to extend its chemical stability to higher pH conditions using protection layers. The use of a strongly basic solution eliminates the need for buffers and can help $BiVO_4$ to be paired with a broad range of photocathodes. ALD is one of the most commonly used methods to deposit a protection layer on $BiVO_4$.[140, 141] For

example, Lewis and co-workers deposited an amorphous 1 nm-thick TiO_2 layer on a flat $BiVO_4$ film using ALD.[140] The resulting $BiVO_4/TiO_2$/Ni OEC photoanode generated a stable photocurrent density of 1.3 mA/cm^2 at 1.23 V vs. RHE for 2 hours in pH 13 KOH. Choi and co-workers demonstrated the use of $ZnFe_2O_4$ as a protection layer[35] that can also provide additional photon absorption. They deposited the $ZnFe_2O_4$ layer on the $BiVO_4$ surface by photodeposition of FeOOH followed by drop-casting an aqueous $Zn(NO_3)_3$ solution and annealing. This resulted in a 10 nm-thick $ZnFe_2O_4$ layer conformally coated on a nanoporous $BiVO_4$ photoanode. When Co^{2+} was adsorbed on the $BiVO_4/ZnFe_2O_4$ photoanode surface to serve as an OEC, a stable photocurrent of 2.5 mA/cm^2 was obtained at 1.23 V vs. RHE for 1 hour in pH 13 KOH.

More recently, Choi and co-workers demonstrated the use of an electrodeposited TiO_2 layer as an excellent protection layer for $BiVO_4$.[142] Compared with ALD, electrodeposition is inexpensive, easily accessible, and fast (e.g. less than 1 min to deposit a 5 nm-thick TiO_2 layer). The excellent conformal nature of the electrodeposited TiO_2 coating layer was confirmed by comparing the chemical stability of $BiVO_4$ with and without the TiO_2 layer immersed in pH 12 solution for one month. (Figure 18) The $BiVO_4$ of the $BiVO_4/TiO_2$ electrode showed no change in crystallinity while the unprotected $BiVO_4$ electrode showed signs of dissolution and loss of crystallinity.

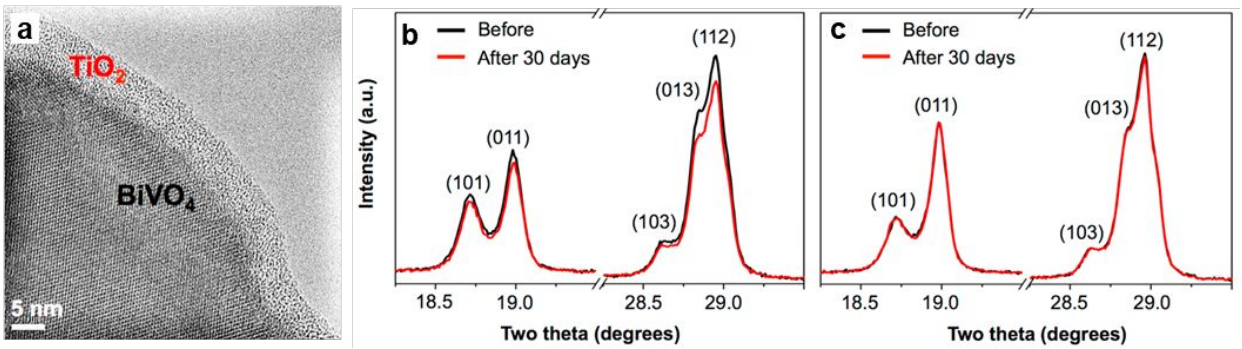

Figure 18. (a) A high-resolution transmission electron microscopy (HRTEM) image of a $BiVO_4/TiO_2$ film. XRD patterns of (b) $BiVO_4$ and (c) $BiVO_4/TiO_2$ electrodes before (black) and after (red) 30 days of immersion in pH 12 phosphate buffer. Adapted with permission from Ref. 142. Copyright 2018 American Chemical Society.

The authors also reported that the $BiVO_4/TiO_2$ electrode showed photoelectrochemical stability for sulfite oxidation (Figure 19a) but not for water oxidation at 0.6 V vs. RHE in pH 12 phosphate buffer for 40 hours. Therefore, the chemical stability gained by the addition of TiO_2 was sufficient to achieve stable photoelectrochemical sulfite oxidation but not stable photoelectrochemical water oxidation. As we explained above, the solubility of $BiVO_4$ when holes have accumulated at the surface is not the same as the solubility of $BiVO_4$ in the dark. Therefore, to ensure the photostability of $BiVO_4/TiO_2$ for water oxidation, the addition of an OEC that can prevent the accumulation of holes on the $BiVO_4$ surface is critical. Indeed, the authors demonstrated that a stable photocurrent density of 1.6 mA/cm^2 could be achieved at 0.6 V vs. RHE in pH 12 phosphate buffer for 20 h when the $BiVO_4/TiO_2$ electrode was combined with a FeOOH/NiOOH OEC (Figure 19b).

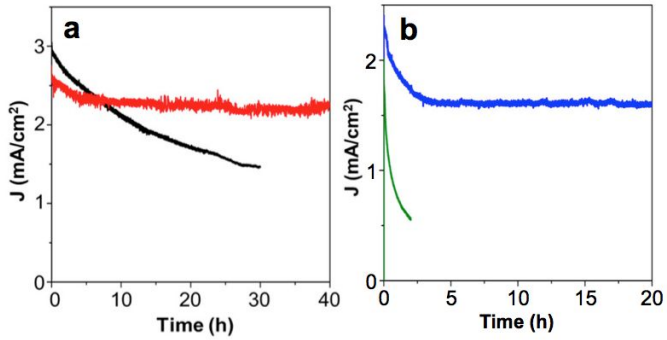

Figure 19. (a) J–t plots at 0.6 V vs. RHE of $BiVO_4$ (black) and $BiVO_4/TiO_2$ (red) electrodes for sulfite oxidation measured in pH 12 phosphate buffer containing 1 M Na_2SO_3. (b) J–t plots at 0.6 V vs. RHE of $BiVO_4$/FeOOH/NiOOH (green) and $BiVO_4/TiO_2$/FeOOH/NiOOH (blue) electrodes for water oxidation measured in pH 12 phosphate buffer. All measurements were obtained under AM 1.5G illumination. Adapted with permission from Ref. 142. Copyright 2018 American Chemical Society.

Light Management Another important factor to consider in further improving photocurrent generation by a photoelectrode is light management that can increase photon absorption. Pilosh and co-workers demonstrated that the insertion of a thin Pt layer between two indium-doped tin oxide (ITO) layers (i.e. glass/ITO/Pt/ITO) increased light absorption through reflection of light off the Pt layer.[143] Cui and co-workers demonstrated that using a cone-shaped $SiO_x/Pt/SnO_2$ substrate increased light absorption by Mo-doped $BiVO_4$ by offering multiple light scattering in the nanocone structure while simultaneously enhancing bulk charge separation.[93] (Figure 20) The resulting nanocone Mo-doped $BiVO_4$ generated a photocurrent for sulfite oxidation of 6.05 ± 0.3 mA/cm^2 at 1.23 V vs. RHE (0.5 M Na_2SO_3, pH 7 phosphate). For comparison, a flat Mo-doped $BiVO_4$ film with the same thickness (700 nm) generated a photocurrent of 2.93 ± 0.12 mA/cm^2 at the same potential. When combined with a FeOOH/NiOOH OEC, nanocone Mo-doped $BiVO_4$ generated a photocurrent for water oxidation of 5.8 mA/cm^2 at 1.23 V vs. RHE in pH 7 phosphate buffer. This is one of the best performances reported for $BiVO_4$ to date. This result shows the importance of optimizing light management to maximize the performance of each photoanode.

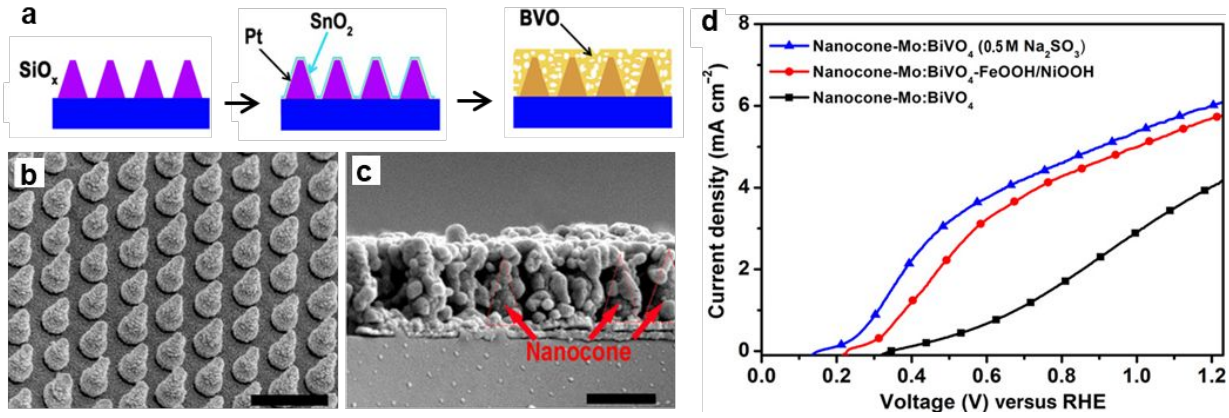

Figure 20. (a) Synthesis process for $BiVO_4$ deposited on SiO_x nanocone arrays. (b) SEM image of $SiO_x/Pt/SnO_2$ nanocone arrays and (c) cross-sectional SEM image of Mo-doped $BiVO_4$ on the $SiO_x/Pt/SnO_2$ nanocone substrate (scale bars = 500 nm), (d) J-V plots of the nanocone Mo-doped $BiVO_4$

films in pH 7 phosphate buffer under AM 1.5G illumination. Adapted with permission from Ref. 93. Copyright 2016 American Association for the Advancement of Science.

The progress made in the past five years in understanding and improving $BiVO_4$ photoanodes has been truly impressive and has led to the achievement of a photocurrent density for water oxidation as high as ~6 mA/cm^2 at 1.23 V vs. RHE (Table 4). The fundamental limitation of using $BiVO_4$ as a photoanode is its relatively wide bandgap. When $BiVO_4$ is used in a PEC composed of a photoanode and a photocathode in tandem, the bandgap of $BiVO_4$ is too wide to achieve a STH efficiency ≥ 10%.[144-146] However, we note that a photoanode can be composed of more than one photon absorber; $BiVO_4$ can be coupled with one or more smaller bandgap n-type semiconductors. Since there is no other photoanode developed to date that can achieve a η_{sep} of close to 100 % like $BiVO_4$, keeping $BiVO_4$ as one of the photon absorbers in the photoanode will allow for the most efficient utilization of photons with energy ≥ 2.4 eV and can result in a higher photocurrent than that achieved by the smaller bandgap photoanode alone. This postulation is well-supported by a recent study by Lee, van de Krol, and co-workers where $BiVO_4$ and Fe_2O_3 were used as dual photoanodes.[20] Although Fe_2O_3 possesses a much smaller bandgap than $BiVO_4$ and should ideally utilize all photons that can be utilized by $BiVO_4$, the combination of $BiVO_4$ and Fe_2O_3 photoanodes resulted in a higher photocurrent density than that demonstrated by Fe_2O_3 alone (Figure 21). Designing optimum multilayer photoanodes containing $BiVO_4$ should be one focus of future research to achieve a PEC with a STH efficiency ≥ 10%.

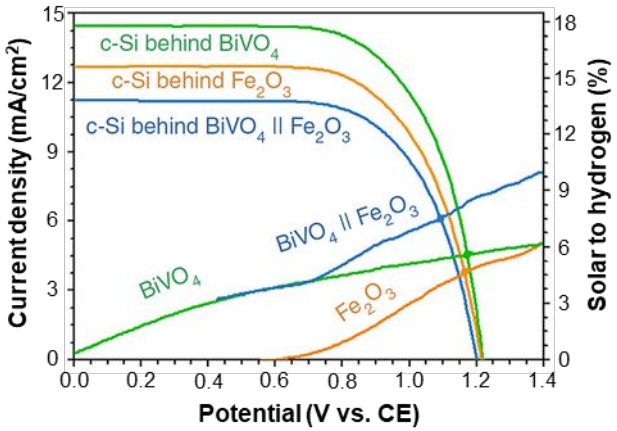

Figure 21. J-V plots of $BiVO_4$, Fe_2O_3, and $BiVO_4$||Fe_2O_3, where $BiVO_4$ and Fe_2O_3 are used as dual photoanodes, intersected with J-V plots of two serially connected c-Si solar cells in pH 9 carbonate buffer under AM 1.5G illumination. The c-Si solar cells were placed behind the photoanodes. Adapted with permission from Ref. 20. Copyright 2016 Macmillan Publishers Limited, part of Springer Nature.

3-4. Other Metal Vanadates

Copper Vanadates Copper vanadates have recently received growing attention as photoanode candidates for water splitting PECs. Neale and co-workers first investigated γ-$Cu_3V_2O_8$ as a photoanode in 2015.[147] An aqueous precipitation reaction was used to form $Cu_3V_2O_7(OH)_2{\cdot}2H_2O$ followed by dip-coating onto FTO and annealing to form γ-$Cu_3V_2O_8$. The resulting films were

composed of interconnected nanoparticles with diameters of ~20 nm. They demonstrated a photocurrent for water oxidation of 10 μA/cm^2 at 1.23 V vs. RHE and a photocurrent for sulfite oxidation of 100 μA/cm^2 at 1.0 V vs. RHE in pH 9.2 borate buffer. The hole diffusion length of γ-$Cu_3V_2O_8$ has been measured to be ~20 - 40 nm.[148] High-throughput screening studies of the CuO-V_2O_5 phase space have reported several additional copper vanadate phases with bandgaps of ~2 eV.[149, 150] Of these, α-CuV_2O_6, β-$Cu_2V_2O_7$, γ-$Cu_3V_2O_8$, $Cu_{11}V_6O_{26}$, and $Cu_5V_2O_{10}$ have been systematically investigated as photoanodes for solar water splitting.[147, 148, 151-156] All of these copper vanadate compounds commonly show a bandgap in the range of 1.8 – 2.0 eV, which is favorable for utilizing a significant portion of visible light. However, the water oxidation photocurrent for this class of compounds remains below 100 μA/cm^2 at 1.23 V vs. RHE, regardless of the phase or electrode preparation conditions.

One strategy that has been used to improve the photocurrent generation of copper vanadate photoanodes is Mo and W doping into the V-site. Doping that substitutionally replaces V^{5+} ions with Mo^{6+} or W^{6+} ions in ternary vanadate oxides, such as $BiVO_4$, has been shown to effectively increase the carrier densities of the host oxide materials.[110, 157] For example, Neale and co-workers showed that Mo doping of γ-$Cu_3V_2O_8$ increased the photocurrent density for water oxidation from 10 μA/cm^2 to 25 μA/cm^2 at 1.23 V vs. RHE and for sulfite oxidation from 100 μA/cm^2 to 180 μA/cm^2 at 1.0 V vs. RHE in pH 9.2 borate buffer.[147] The authors confirmed that the increase in photocurrent was due to an increase in the carrier density as observed by Mott-Schottky analysis. However, Mo doping did not shift the photocurrent onset potential for either water or sulfite oxidation.

Choi and co-workers prepared Mo-doped and W-doped $Cu_{11}V_6O_{26}$ using nanofibrous CuO films as precursor films[158] and annealing with a $VO(acac)_2$ solution containing Mo or W precursors.[155] Dopant atom incorporation was confirmed by slight peak shifts in the XRD patterns to lower two theta values. Mott-Schottky analysis was also used and a decrease in the slope and a shift in the E_{FB} to the negative direction was observed for both Mo and W doping, indicating an increase in the carrier concentration (E_{FB}s: $Cu_{11}V_6O_{26}$ = 0.64 – 0.73 V vs. RHE, Mo:$Cu_{11}V_6O_{26}$ = 0.51 – 0.60 V vs. RHE, W:$Cu_{11}V_6O_{26}$ = 0.51 – 0.60 V vs. RHE). An example of the photocurrent enhancement observed for sulfite oxidation in pH 9.2 borate buffer after doping of $Cu_{11}V_6O_{26}$ is shown in Figure 22. The highest photocurrent density seen in this study was achieved by the optimally doped W:$Cu_{11}V_6O_{26}$ film and reached a value of 70 μA/cm^2 for water oxidation at 1.23 V vs. RHE and 145 μA/cm^2 for sulfite oxidation at 1.0 V vs. RHE in pH 9.2 borate buffer. In addition to this enhancement, W doping caused a shift in the onset potential from 0.99 to 0.87 V vs. RHE for water oxidation and 0.65 to 0.58 V vs. RHE for sulfite oxidation (inset Figure 22), which agrees well with the Mott-Schottky results.

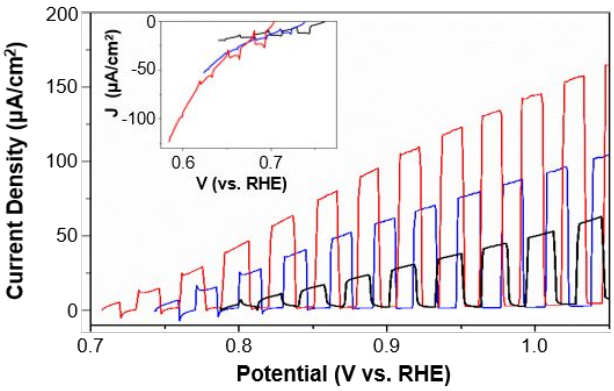

Figure 22. Chopped light J-V scans for pristine (black), Mo-doped (blue), and W-doped (red) $Cu_{11}V_6O_{26}$ for sulfite oxidation in pH 9.2 borate buffer under AM 1.5G illumination. The inset shows the photocurrent obtained by sweeping the potential from the open circuit potential (OCP) under illumination to the negative direction to accurately determine the photocurrent onset potentials. Adapted with permission from Ref. 155. Copyright 2017 American Chemical Society.

As there are many different copper vanadate phases that exist, Gregoire and co-workers investigated the effect of the Cu:V ratio on the chemical, electrochemical, and photoelectrochemical stabilities of copper vanadates. They sputter coated libraries with the composition $Cu_{1-x}V_xO_z$, with x ranging from 0.1 to 0.75.[159] The authors performed chemical (48 hour soak), electrochemical (2 hours of operation at 1.23 V vs. RHE), and photoelectrochemical (40 minutes of operation at 1.23 V vs. RHE under AM 1.5G illumination) stability tests in pH 9.2 borate buffer. They found that all phases with $x < 0.67$ were chemically stable and all phases with $x < 0.57$ were electrochemically stable under these conditions. This means that all phases discussed above, excluding α-CuV_2O_6, should be both chemically and electrochemically stable in pH 9.2 solution. Photoelectrochemical stability tests were performed for all phases with $x < 0.5$ and the results showed that that the phases with a higher Cu:V ratio (e.g. $Cu_{11}V_6O_{26}$ and γ-$Cu_3V_2O_8$) appeared to be more photostable. Indeed, Sharp and co-workers showed stable photocurrent generation of ~65 μA/cm^2 at 1.23 V vs. RHE in pH 9.2 borate buffer for water oxidation for more than 20 h using γ-$Cu_3V_2O_8$ prepared by reactive co-sputtering.[148] In addition, Choi and co-workers showed that $Cu_{11}V_6O_{26}$ can be operated even in pH 13 KOH solution for 2 hours at 1.4 V vs. RHE without significant photocurrent decay, which is impressive for a V-containing photoelectrode.[155]

Recently, Sharp and co-workers also performed a systematic investigation to elucidate the effects of the varying Cu and V stoichiometries on the photoelectrochemical properties of copper vanadates using β-$Cu_2V_2O_7$, γ-$Cu_3V_2O_8$, $Cu_{11}V_6O_{26}$, and $Cu_5V_2O_{10}$ electrodes prepared by reactive co-sputtering.[156] They first measured the performance of copper vanadate photoelectrodes for sulfite oxidation in pH 9.3 borate buffer and found that the phases with the highest Cu:V ratio (e.g. $Cu_5V_2O_{10}$) showed the highest photocurrent generation. They determined that $Cu_5V_2O_{10}$ had the highest absorption coefficient and the highest IPCE and APCE values for sulfite oxidation. (IPCE = 7% and APCE = 10% at 350 nm and 1.23 V vs. RHE). These results indicate that the phases with a higher Cu:V ratio exhibit better photon absorption and charge separation properties.

Although copper vanadate photoanodes represent an interesting class of materials to study because of the rich Cu-V-O phase space that exists, they appear to commonly suffer from

serious bulk recombination judging from their very low photocurrent generation. Another critical limitation of this class of compounds appears to be their extremely positive photocurrent onsets for water oxidation. The most negative onset potential achieved for water oxidation by a copper vanadate photoanode to date is only 0.82 V vs. RHE using 3% W-doped $Cu_{11}V_6O_{26}$.[155] Additionally, the E_{FB} of this photoelectrode is the most negative reported to date but still lies at 0.58 V vs. RHE, even after optimum doping levels were achieved for maximum photocurrent generation. This suggests that the E_{FB} positions of copper vanadates may be fundamentally limited by their CBM positions, which will prevent copper vanadate photoanodes from achieving considerable photovoltages for water oxidation. Accurate measurements of the CBM positions of copper vanadates would be useful to determine their viability as photoanodes for solar water splitting.

Iron Vanadates There are several polymorphs of iron vanadate with the formula $FeVO_4$ but triclinic $FeVO_4$ is the only phase that can form under ambient conditions. The potential of triclinic $FeVO_4$ as a photoanode was first reported from a high-throughput screening study performed in 2007 by Sayama and co-workers.[160] Although $FeVO_4$ has a chemical formula reminiscent of $BiVO_4$, it is has a distinctly different crystal structure from that of $BiVO_4$. For example, while Bi in $BiVO_4$ is coordinated by 8 oxygen atoms, Fe in $FeVO_4$ is coordinated by either 5 or 6 oxygen atoms.[110, 161] The bandgap of $FeVO_4$ is ~2.0 eV,[162-166] which is smaller than that of $BiVO_4$. However, similar to the copper vanadate family discussed above, the most negative E_{FB} reported for $FeVO_4$ to date is ~700 mV below the water reduction potential,[165] which limits the maximum photovoltage achievable by this compound for water oxidation to ~500 mV. This suggests that the smaller bandgap of $FeVO_4$ is most likely caused by the very positive position of its CBM, which is not favorable for achieving a high STH efficiency.

To date, the photocurrent reported for $FeVO_4$ remains quite low, and substitutional doping into the V-site has been investigated as one possibility to improve the photocurrent generation, as discussed for copper vanadates and $BiVO_4$ above. Baeg and co-workers compared $FeVO_4$ and 5% W-doped $FeVO_4$ electrodes prepared by spin-coating metal-organic precursors onto FTO substrates followed by thermal annealing.[163] The incorporation of W into the lattice was confirmed by a slight shift of the main XRD peak to a lower two theta value due to the larger ionic radius of W^{6+} compared to V^{5+}. The pristine film showed a photocurrent generation of 50 $\mu A/cm^2$ for water oxidation at 1.23 V vs. RHE in pH 7 phosphate buffer, which was increased to 100 $\mu A/cm^2$ for the W-doped film. The onset for photoelectrochemical water oxidation for both samples was ~0.7 V vs. RHE. The enhancement in the photocurrent implies an increase in the carrier density after doping; however, Mott-Schottky analysis was not performed to confirm this. IPCE of the W-doped sample was also measured and reached a maximum value of 6.5% at 400 nm with an applied bias of 1.7 V vs. RHE in the same solution.

In addition to doping, the synthesis of nanoporous $FeVO_4$ electrodes has been investigated as a strategy to try to shorten the charge extraction path length.[164] A nanoporous $FeVO_4$ film was prepared by a drop-casting method with the addition of citric acid to facilitate the formation of pores. SEM images of the films after annealing revealed interconnected nanoparticles with a diameter of ~50 - 100 nm and a pore size of ~50 - 200 nm. The nanoporous $FeVO_4$ photoelectrode showed a photocurrent for water oxidation of 100 $\mu A/cm^2$ at 1.23 V vs. RHE (pH 7 phosphate buffer), which is higher than the photocurrent generated by undoped $FeVO_4$ photoanodes prepared by other methods but still remains low.

Most recently, Abdi and co-workers performed in-depth studies on pristine and Mo-doped $FeVO_4$ photoanodes to determine the origin of this low photocurrent generation.[165] $FeVO_4$ and Mo-doped $FeVO_4$ films were prepared by spray pyrolysis onto FTO followed by annealing in air. SEM images revealed densely packed particles with a diameter of ~500 nm. The thickness of the films was varied from 25 - 800 nm and films with a thickness of 200 - 400 nm were found to generate the highest photocurrent. Moving forward, all samples discussed will be 200 nm-thick samples. The Mo-doped samples showed slight shifts in their XRD peaks to lower two theta values, indicating that Mo^{6+} was indeed incorporated into the lattice. The authors determined that the 2% Mo-doped sample showed the highest photocurrent generation (Figure 23), and Mott-Schottky analysis revealed a decrease in the slope of this sample compared to that of the undoped sample, indicating an increase in the carrier concentration. However, the E_{FB}s of both pristine and 2% Mo-doped samples were equal at 0.7 V vs. RHE. By comparing the photocurrent for sulfite oxidation and water oxidation, the authors determined that Mo doping increased η_{sep} from 2% to 2.5% at 1.6 V vs. RHE. In addition, η_{ox} for water oxidation at 1.6 V vs. RHE was found to increase from 80% to 100% after Mo doping. These results show that severe bulk recombination is one of the major limitations of $FeVO_4$ and the improvement in η_{sep} that resulted from Mo doping was negligible**.** The maximum IPCE achieved by the pristine and Mo-doped $FeVO_4$ films for water oxidation at 1.6 V vs. RHE in pH 7 phosphate buffer were 2% and 8%, respectively, at 375 nm**.** The authors also used TRMC to determine the carrier transport properties of $FeVO_4$ and Mo-doped $FeVO_4$. They found a hole mobility of 4.6 x 10^{-5} cm^2 V^{-1} s^{-1} for their pristine sample and 1.3 x 10^{-4} cm^2 V^{-1} s^{-1} for their 2% Mo-doped sample. The hole diffusion length was determined to be ~2 nm for the undoped sample and ~7 nm for the Mo-doped sample. The extremely short diffusion length of $FeVO_4$ also suggests that improving bulk separation by nanostructuring may be difficult.

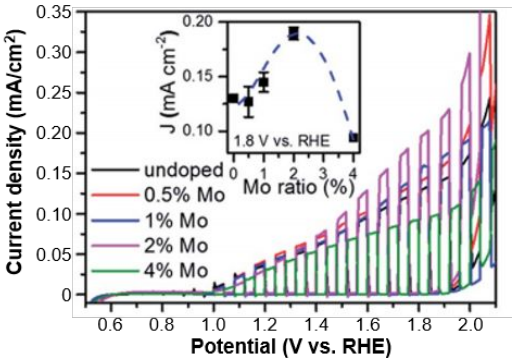

Figure 23. Chopped light J-V plots of undoped and Mo-doped $FeVO_4$ for water oxidation in pH 7 phosphate buffer under AM 1.5G illumination. The inset shows the change of the current density with the Mo doping level at 1.8 V vs. RHE. Adapted with permission from Ref. 165. Copyright 2018 The Royal Society of Chemistry.

While triclinic $FeVO_4$ is the most well-studied iron vanadate phase, there are a few other iron vanadates that have been investigated as photoanodes (e.g. Fe_2VO_4, FeV_2O_4, $Fe_2V_4O_{13}$).[167, 168] Among these compounds, we note that Fe_2VO_4 and FeV_2O_4 contain reduced iron and vanadium species (Fe^{2+}, V^{3+}, and V^{4+}) that may not be stable during photoelectrochemical water oxidation. Therefore, their photostabilities need to be investigated carefully. Indeed, Bhattacharya and co-workers performed J-t scans for water oxidation in pH 7 phosphate buffer at

1.6 V vs. RHE and observed that $FeVO_4$, Fe_2VO_4, and FeV_2O_4 all showed significant photocurrent decay after 30 minutes of testing.[167]

The studies reported so far indicate that iron vanadates commonly suffer from extremely short hole diffusion lengths and severe bulk recombination. Successful atomic doping that can result in a considerable increase in η_{sep} of iron vanadates has not yet been demonstrated. Nanostructuring may be one strategy to alleviate the low photocurrent generation caused by extremely short hole diffusion lengths. However, another fundamental limitation for iron vanadates is their E_{FB} positions that remain very positive (≥ 0.5 V vs. RHE) even with doping.[165, 168] This suggests that iron vanadates will have the same challenges as copper vanadates for use as photoanodes in a water splitting PEC.

3-5. Others

Fe_2TiO_5 Fe_2TiO_5 has a narrow bandgap of 2.0 − 2.1 eV,[169-171] is composed of cheap and abundant materials, and exhibits chemical stability in neutral and basic conditions (pH 7 - 14).[172-174] Various techniques such as single crystal growth by the Czochralski method,[170, 172] dip-coating sol-gel precursors,[173, 175] solvothermal synthesis,[171] and template-based methods using polystyrene opals[169] or aluminum oxide templates[176] have been used to make Fe_2TiO_5 thin films.

Compared with TiO_2, the bandgap of Fe_2TiO_5 is significantly smaller. While the bandgap of Fe_2TiO_5 is comparable to that of Fe_2O_3, the CBM and VBM of Fe_2TiO_5 are believed to straddle the water reduction and oxidation potentials, making Fe_2TiO_5 more suitable than Fe_2O_3 for solar water splitting applications (Figure 24).[171, 175, 177, 178]

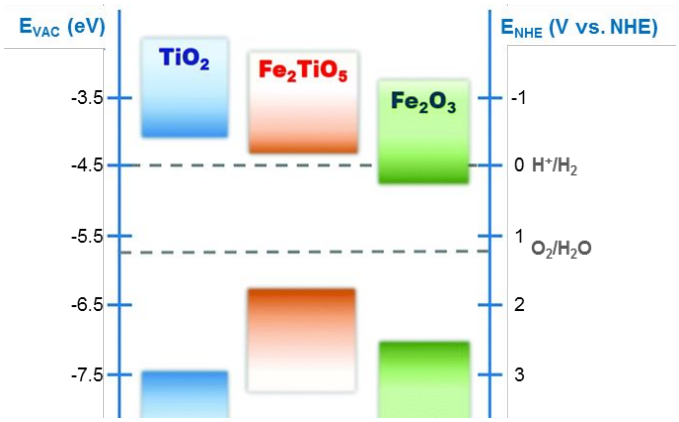

Figure 24. Band energy diagrams for TiO_2, Fe_2TiO_5, and Fe_2O_3. Adapted with permission from Ref. 178 Copyright 2017 The Royal Society of Chemistry.

Lee and co-workers showed that Fe_2TiO_5 can produce a photocurrent for water oxidation as high as 0.93 mA/cm^2 at 1.23 V vs. RHE in 1 M NaOH after optimization of synthesis conditions and the addition of appropriate underlayers and catalysts.[176] The authors prepared a nanotubular Fe_2TiO_5 film by a spin-coating method using porous alumina as a hard template. The alumina template was removed after the synthesis by dissolution in 0.25 M NaOH. The authors determined that the optimum wall thickness of the Fe_2TiO_5 nanotubes was 10 − 15 nm, and an increase in the wall thickness to 20 − 25 nm resulted in a decrease in photocurrent. This suggests that Fe_2TiO_5 suffers from a short carrier diffusion length like Fe_2O_3 and other Fe-containing

oxide-based photoanodes. The as-prepared nanotubular Fe_2TiO_5 electrode showed a photocurrent density for water oxidation of 0.34 mA/cm^2 at 1.23 V vs. RHE with a photocurrent onset potential of 0.8 V vs. RHE (Figure 25a). To further increase the photocurrent, the authors added a TiO_2 underlayer between the Fe_2TiO_5 nanotubes and the FTO substrate. The TiO_2 layer can serve as a barrier to block electron injection from FTO to the electrolyte, which can occur when the FTO substrate is in direct contact with the electrolyte.[179] When photoexcited electrons are consumed on the FTO substrate of the photoanode, it is equivalent to the loss of charge carriers by recombination. Furthermore, since the VBM of TiO_2 is below that of Fe_2TiO_5, TiO_2 can serve as a hole blocking layer that prevents the injection of holes from the VBM of Fe_2TiO_5 to FTO, suppressing recombination loss at the FTO/Fe_2TiO_5 interface.[180] The addition of the TiO_2 underlayer resulted in a negative shift of the onset potential by 200 mV and a slight enhancement of the photocurrent (Figure 25a).

Lee and co-workers also treated their Fe_2TiO_5 with H_2 at 300 °C for 4 h to increase the donor density by creating oxygen vacancies, which was confirmed by Mott-Schottky analysis.[176] The H_2-treated sample showed an improvement in photocurrent generation in the high bias region (≥ 0.95 V vs. RHE) resulting from improved electron-hole separation. Finally, a $FeNiO_x$ OEC was deposited to facilitate hole transfer for water oxidation.[176] With all of these modifications combined, the resulting TiO_2/H_2-treated Fe_2TiO_5/$FeNiO_x$ photoanode demonstrated a significantly improved photoelectrochemical performance for water oxidation with an onset potential of 0.5 V vs. RHE and a photocurrent of 0.93 mA/cm^2 at 1.23 V vs. RHE. Additionally, this photoelectrode demonstrated stable photocurrent generation for water oxidation over 2.5 h at 1.23 V vs. RHE (Figure 25b). We note that the E_{FB} of this nanotubular Fe_2TiO_5 film determined by Mott-Schottky analysis was between 0.3 and 0.45 V vs. RHE, which is far below its reported CBM.[176] This suggests that atomic doping that can further increase the carrier density and raise the E_{FB} may further improve its performance.

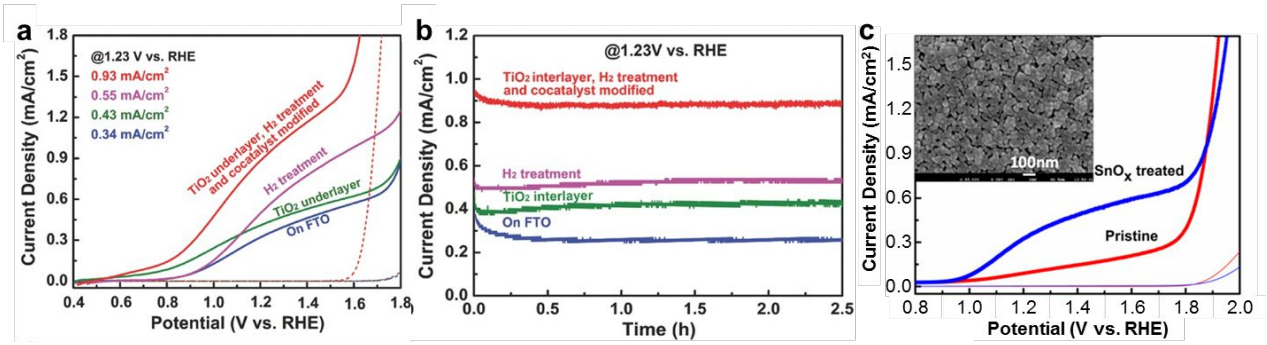

Figure 25. (a) J-V plots and (b) J-t plots of Fe_2TiO_5 nanotube arrays on FTO substrates with different modifications: pristine Fe_2TiO_5 on FTO (blue); Fe_2TiO_5 with a TiO_2 underlayer (green); H_2-treated Fe_2TiO_5 (purple); and combined TiO_2 underlayer, H_2 treatment, and cocatalyst ($FeNiO_x$) modified Fe_2TiO_5 (red). Adapted with permission from Ref. 176 John Wiley & Sons. Copyright 2017 WILEY-VCH Verlag GmbH & Co. KGaA, (c) J-V plots of pristine (red) and SnO_x treated (blue) Fe_2TiO_5 films. Adapted with permission from Ref. 171. Copyright 2014 American Chemical Society. All measurements were performed in 1 M NaOH under AM 1.5G illumination.

Another strategy to improve the performance of Fe_2TiO_5 was reported by Wong and co-workers.[171] In this study, a porous Fe_2TiO_5 film with a particle size of 30 − 50 nm was prepared by solvothermal synthesis. An extremely thin layer of SnO_x was then coated on top of the

Fe_2TiO_5 film by drop-casting an aqueous $SnCl_4 \cdot 5H_2O$ solution and annealing in air at 750 °C for 20 min. The authors reported that the presence of SnO_x on the surface of Fe_2TiO_5 effectively passivated existing surface states and significantly increased the photocurrent by reducing surface recombination (Figure 25c). For example, after the SnO_x treatment, the photocurrent for water oxidation increased from 0.1 mA/cm^2 to 0.36 mA/cm^2 at 1.23 V vs. RHE in 1 M NaOH.

The highest performing Fe_2TiO_5 photoelectrode reported to date was prepared by cathodic electrodeposition of $Fe(OH)_3$ on a vertically aligned nanotube array of TiO_2 followed by annealing in air at 550 °C for 2 h.[181] Although Fe_2TiO_5 was deposited as an extremely thin layer (2 − 3 nm) (Figure 26a), the high surface area of the TiO_2 nanotubes (tube length of 7.8 μm, tube wall thickness of 10 nm, and pore size of ~50 nm) (Figure 26b) resulted in considerable photon absorption by Fe_2TiO_5. At the same time, the use of a thin Fe_2TiO_5 layer reduced the distance that holes and electrons need to travel, significantly decreasing bulk recombination. Since the VBM of Fe_2TiO_5 lies above that of TiO_2, TiO_2 can serve as a hole blocking layer while also efficiently transferring any photogenerated holes from TiO_2 to the Fe_2TiO_5 layer. The CBMs of TiO_2 and Fe_2TiO_5 are comparable (~0 V vs. RHE), and it appears that electron injection from the Fe_2TiO_5 layer to TiO_2 occurred without any problem. After the addition of a Co-based OEC, which was denoted as Co_{ox} in their study, an impressive photocurrent for water oxidation of 4.1 mA/cm^2 at 1.23 V vs. RHE was achieved in 1 M KOH solution by the Fe_2TiO_5-TiO_2/Co_{ox} photoanode (Figure 26c). The TiO_2 nanotube arrays contributed a photocurrent of only 0.8 mA/cm^2 at this potential, meaning that the Fe_2TiO_5 layer was responsible for generating an additional 3.3 mA/cm^2. Furthermore, APCE spectra of Fe_2TiO_5-TiO_2/Co_{ox} confirmed that photons absorbed by Fe_2TiO_5 were effectively utilized in this system for photocurrent generation. The Fe_2TiO_5-TiO_2/Co_{ox} photoanode also demonstrated photostability; it maintained a photocurrent density of 3 mA/cm^2 at 0.4 V vs. RHE for 2 h (Figure 26d).

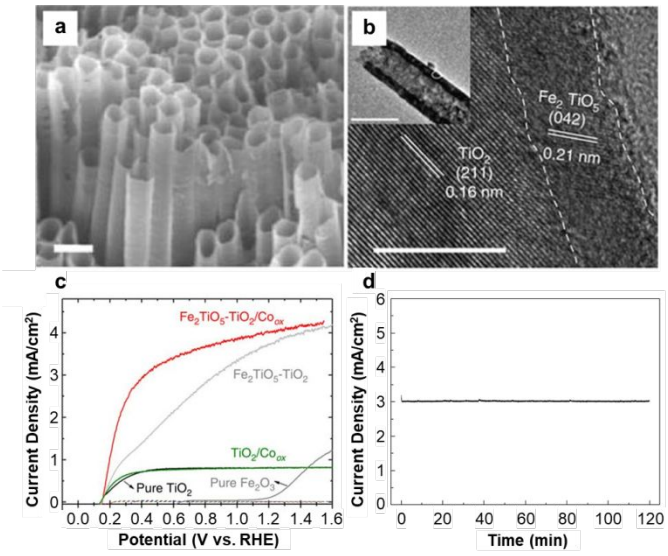

Figure 26. (a) SEM and (b) HRTEM images of a Fe_2TiO_5-TiO_2/Co_{ox} nanotube array (scale bars: 200 nm, 100 nm, and 5 nm for a, inset of b, and b, respectively). (c) J-V plots (solid lines) for pure Fe_2O_3 (dark grey), pure TiO_2 (black), TiO_2/Co_{ox} (green), Fe_2TiO_5-TiO_2 (light grey), and Fe_2TiO_5-TiO_2/Co_{ox} (red). Dashed lines denote dark current. (d) J-t plot for the Fe_2TiO_5-TiO_2/Co_{ox} photoanode measured at 0.4 V vs. RHE in 1 M KOH under AM 1.5G illumination. Adapted with permission from Ref. 181. Copyright 2015 Macmillan Publishers Limited, part of Springer Nature.

There have also been several studies using Fe_2TiO_5 as an additional layer on Fe_2O_3 photoanodes.[174, 177, 178, 182, 183] Although Fe_2TiO_5 cannot enhance the photon absorption of Fe_2O_3 because Fe_2TiO_5 and Fe_2O_3 have similar bandgaps, the formation of the Fe_2TiO_5/Fe_2O_3 junction has been shown to improve electron-hole separation in both layers. This is because the CBMs and VBMs of these two compounds are aligned such that holes move toward the Fe_2TiO_5 layer while electrons move toward the Fe_2O_3 layer.[174, 177, 178, 183] For example, Kaunisto and co-workers used transient absorption spectroscopy to observe a slower decay of long-lived hole signals when Fe_2TiO_5 was present as a top layer on Fe_2O_3 compared to Fe_2O_3 alone.[183] These long-lived surface holes resulted in an increase in photocurrent for water oxidation obtained in 0.1 M NaOH from ~0.02 mA/cm^2 by Fe_2O_3 to ~0.75 mA/cm^2 by Fe_2TiO_5/Fe_2O_3 at 1.23 V vs. RHE. In this study, the authors prepared the Fe_2TiO_5 shell on the Fe_2O_3 core by mixing Fe_2O_3 and TiO_2 nanoparticles, spin-coating onto a FTO substrate, and annealing at 680 °C in air. The Fe_2TiO_5/Fe_2O_3 composite prepared with 15 molar-% TiO_2 showed the best improvement of the photocurrent without forming a segregated TiO_2 phase.

Schmuki and co-workers reported that another possible advantage of using a Fe_2TiO_5 overlayer on Fe_2O_3 is to decrease surface recombination.[182] The authors thermally oxidized Fe foil to produce Fe_2O_3 nanoflakes followed by sequential immersion in a $Fe(NO_3)_3$ solution and a $TiCl_3$ solution. These films were then annealed in air at 850 °C for 1 min to form an Fe_2TiO_5 overlayer. From HRTEM images, the formation of a 10 − 15 nm-thick Fe_2TiO_5 coating layer was confirmed. The authors showed that the addition of the Fe_2TiO_5 overlayer resulted in a decrease in the transient photocurrent observed in the J-V plots for water oxidation, an increase in photocurrent (from 0.22 mA/cm^2 to 0.78 mA/cm^2 at 1.23 V vs. RHE), and a cathodic shift of the onset potential compared to pristine Fe_2O_3 (from 0.7 to 0.62 V vs. RHE) in 1 M KOH.[184] The authors also observed a decrease in the semiconductor-electrolyte charge transfer resistance when Fe_2TiO_5 was present. They concluded that all observed changes were caused by Fe_2TiO_5 serving as a surface passivation layer.

Judging from the band positions and photoelectrochemical performances demonstrated thus far, it appears that Fe_2TiO_5 is one of the most promising photoanode candidates among the Fe-containing oxides. Although it suffers from bulk recombination, a considerable amount of photocurrent was generated when Fe_2TiO_5 was deposited as a thin layer on a high surface area, wide-bandgap substrate. Its chemical and photoelectrochemical stability in strong base (e.g. pH 14) is also attractive. However, very few studies have been performed to optimize Fe_2TiO_5 electrodes using atomic doping to move its E_{FB} closer to its reported CBM. Various strategies that have been used for the development of Fe_2O_3 and other ferrite electrodes may also be used to further improve the photoelectrochemical properties of Fe_2TiO_5.

$SnNb_2O_6$ $SnNb_2O_6$ is an n-type semiconductor with a bandgap of 2.3 − 2.6 eV.[185-187] The α^{-1} of $SnNb_2O_6$ is reported to be 500 nm at λ = 450 nm, which compares favorably with other oxide-based photoelectrode materials.[188] $SnNb_2O_6$ has been primarily investigated as a visible light photocatalyst for H_2 evolution in the presence of a hole acceptor (e.g. methanol or lactic acid) or for O_2 evolution in the presence of an electron acceptor (e.g. $AgNO_3$).[81, 82, 185, 189-191] These studies confirm that the CBM and VBM positions of $SnNb_2O_6$ can enable the utilization of photogenerated holes and electrons for water reduction and oxidation, respectively. The bandgap of $SnNb_2O_6$ is comparable to that of $BiVO_4$, but the band positions of $SnNb_2O_6$ are thermodynamically more suitable for photoelectrochemical water splitting than those of $BiVO_4$.[81, 192]

One critical issue in the synthesis of $SnNb_2O_6$ is control of the oxidation state of Sn ions. Like α-$SnWO_4$, Sn in $SnNb_2O_6$ exists as Sn^{2+}. This provides a challenge during the synthesis because Sn^{2+} in Sn^{2+}-containing oxides can easily be oxidized to Sn^{4+} when heated in the presence of oxygen.[192] SnO is also known to disproportionate into Sn^{4+} and Sn^0 at high temperature even when an inert atmosphere is used.[193] This can affect the synthesis of $SnNb_2O_6$ when SnO is used as a precursor. Since the presence of Sn^{4+} ions or Sn^{4+}-containing impurity phases may serve as defect sites that can increase electron-hole recombination in $SnNb_2O_6$, the synthesis of $SnNb_2O_6$ using a mild temperature and an inert environment is preferable. For example, Takanabe and co-workers used XPS and Auger spectroscopy to show that $SnNb_2O_6$ prepared by flux-assisted synthesis at 600 °C in a N_2 environment contained a smaller amount of Sn^{4+} compared to $SnNb_2O_6$ prepared by solid state synthesis at 800 °C in a N_2 environment.[82] Kudo and co-workers used thermogravimetric analysis (TGA) to compare the formation of Sn^{4+} in $SnNb_2O_6$ and SnO. Since the oxidation of Sn^{2+} to Sn^{4+} in air involves the incorporation of oxygen, an increase in weight will be observed if this oxidation occurs.[81] Their result showed that considerable oxidation of Sn^{2+} in SnO occurs at ~500 °C, but considerable oxidation of Sn^{2+} in $SnNb_2O_6$ does not occur until ~800 °C. This result indicates that once Sn^{2+} is stabilized in the $SnNb_2O_6$ lattice, Sn^{2+} is more stable against thermal oxidation. This result also suggests that developing a synthesis method to form $SnNb_2O_6$ at a lower temperature and then performing subsequent annealing at a higher temperature when necessary (e.g. to improve crystallinity) will be a more effective strategy to decrease the formation of Sn^{4+}.

Despite the attractive bandgap and band positions of $SnNb_2O_6$, $SnNb_2O_6$ did not receive great attention as a photoanode candidate until 2017 when Kudo and co-workers reported the first successful investigation of its photoelectrochemical properties.[186] In this study, the authors prepared $SnNb_2O_6$ particles through the reaction of a $Na_2Nb_2O_6 \cdot H_2O$ precursor with molten $SnCl_2$ at 500 °C in a N_2 atmosphere followed by an additional annealing step at 900 °C in a N_2 atmosphere. The authors then used the particle transfer (PT) method to fabricate $SnNb_2O_6$ photoanodes.[194] Using this method, the $SnNb_2O_6$ powder was first drop-casted onto a glass substrate. Then, a Ti contact layer was deposited on top of the powder by thermal vapor deposition to form an ohmic contact with $SnNb_2O_6$. A conductive Sn layer was then deposited on the Ti contact layer using vacuum vapor deposition to increase the mechanical strength and conductivity. The resulting Sn/Ti/$SnNb_2O_6$ sample was bound to a new glass substrate with carbon tape and was lifted off the original glass substrate. Finally, all loosely bound $SnNb_2O_6$ powder was removed by sonication in water.

The authors subsequently added a CoO_x OEC by drop-casting an aqueous $Co(NO_3)_2$ solution followed by heating at 100 − 500 °C for 2 h in air. The authors stated that the use of an annealing temperature greater than 200 °C resulted in a drastic photocurrent decrease, which they postulated may be due to the oxidation of Sn^{2+} to Sn^{4+}. It may also be due to the incorporation of Co ions into the $SnNb_2O_6$ lattice, thus creating recombination sites at the $SnNb_2O_6/CoO_x$ interface.

While the bare $SnNb_2O_6$ electrode showed negligible photocurrent, the $SnNb_2O_6/CoO_x$ photoanode generated considerable photocurrent for water oxidation (Figure 27a). For example, optimum loading of CoO_x (0.5 wt%) resulted in a photocurrent density of 1.5 mA/cm^2 at 1.2 V vs. RHE (Figure 27b) in pH 9.4 borate buffer. The authors reported the photocurrent onset potential to be 0.3 V vs. RHE, but the LSV shown in Figure 27a suggests that the onset may be even more negative than 0.3 V vs. RHE. This means that $SnNb_2O_6$ can provide a photovoltage of almost 1 V for water oxidation. The $SnNb_2O_6$/CoOx photoanode also showed an excellent fill

factor and the photocurrent generated in the low bias region was considerable (e.g. 0.8 mA/cm^2 at 0.6 V vs. RHE). These results are exciting because such excellent performance in the low bias region is not common for oxide-based photoanodes. The LSVs shown in Figure 10a resemble those of early reports of $BiVO_4$, where the electron-hole separation in $BiVO_4$ was not optimized.[86, 130] Furthermore, the $SnNb_2O_6$/CoOx photoanode showed excellent stability over a 10-hour J-t measurement at 0.6 V vs. RHE in the same solution with a faradaic efficiency close to 100% for both H_2 and O_2 production (Figure 27c). Additionally, the IPCE and applied bias photon-to-current efficiency (ABPE) at 0.6 V vs. RHE were reported to be 18% and 0.39%, respectively.

The observation that the addition of an OEC drastically improved the photocurrent generation by $SnNb_2O_6$ suggests that the bare $SnNb_2O_6$ photoanode suffers from severe surface recombination and its η_{ox} for water oxidation is extremely low. Thus, bulk recombination in $SnNb_2O_6$ may not be as serious as it is in other photoanode materials. This also indicates that the negligible photocurrent generated by bare $SnNb_2O_6$ photoanodes reported in other studies[187, 190, 195, 196] may also be due to the lack of an OEC that can increase the rate of water oxidation to be faster than that of surface recombination.

We note that the dark current of $SnNb_2O_6$ prepared by Kudo and co-workers is negligible, (Figure 27a) indicating that Sn^{2+} in the $SnNb_2O_6$ lattice is electrochemically stable between 0 and 1.4 V vs. RHE. The authors mentioned that photooxidation of Sn^{2+} to Sn^{4+} in $SnNb_2O_6$ can occur during water oxidation by photogenerated holes. However, the authors also showed that the degree of photooxidation of Sn^{2+} to Sn^{4+} can be suppressed by the presence of a CoO_x OEC that can utilize a greater fraction of surface-reaching holes for the water oxidation reaction. Lastly, their results showed that although the formation of Sn^{4+} cannot be completely suppressed, the presence of Sn^{4+} may not be detrimental for the photocurrent generation as long as $SnNb_2O_6$ is coupled with an OEC that can cause the rate of water oxidation to be faster than the rate of surface recombination.

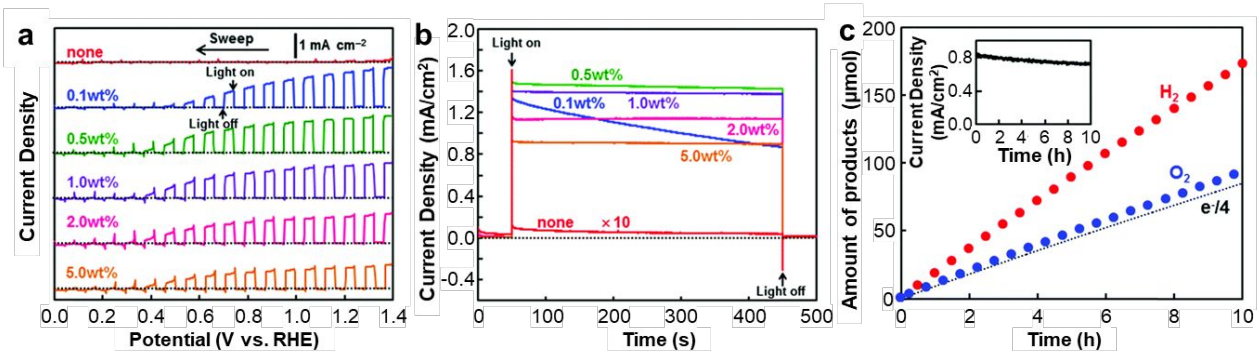

Figure 27. (a) J-V and (b) J-t plots at 1.2 V vs. RHE for the bare $SnNb_2O_6$ (red) and $SnNb_2O_6/CoO_x$ photoelectrodes in pH 9.4 borate buffer under AM 1.5G illumination. The CoO_x loading amount was varied from 0.1 - 5.0 wt. %. (c) H_2 and O_2 evolution using a three-electrode system composed of a $SnNb_2O_6/CoO_x$ (0.5 wt. %) WE, a Pt CE, and an Ag/AgCl RE. The inset shows the photocurrent density at 0.6 V vs. RHE. Adapted with permission from Ref. 186. Copyright 2017 The Royal Society of Chemistry.

To better understand the charge transport properties of $SnNb_2O_6$, future studies should include the determination of η_{sep} as well as in-depth investigations of the carrier mobility and carrier diffusion length. The photocurrent of $SnNb_2O_6$ is expected to be further enhanced with

composition tuning if challenges related to the suppression of Sn^{4+} formation can be successfully addressed. Adding a surface protection layer that can prevent the formation of Sn^{4+} during photocurrent generation may also become an effective strategy to improve the photoelectrochemical properties of $SnNb_2O_6$.

4. Summary and Outlook

Compared with our knowledge of ternary oxide-based photoelectrodes ten years ago, tremendous progress has been made in developing and understanding oxide-based photoanodes for use in PECs. In this review, we have provided a critical evaluation of ternary oxide-based photoanodes that have met our selection criteria laid out in the introduction. The results summarized here clearly show that the performance of most oxide-based photoanodes is limited by their severe bulk recombination. Therefore, improving the charge transport properties of both majority and minority carriers to improve bulk separation is the key to improving the photoelectrochemical properties of oxide-based photoanodes. Atomic doping, defect control (either generation or suppression), and morphology tuning were discussed as the primary strategies to improve charge carrier separation. Additionally, multiple studies demonstrated that a dopant introduced for a certain purpose can affect other properties of the host compound. For example, a dopant introduced to increase the majority carrier density can either improve or diminish the minority carrier transport properties, or a dopant introduced to enhance photon absorption can also improve the mobility of the majority carriers. Therefore, obtaining a comprehensive understanding of the effects of a dopant and identification of a dopant that can simultaneously improve multiple properties of a photoanode can offer effective strategies for atomic doping. Also, while the carrier transport in most oxide-based photoanodes occurs through small polaron hopping, our understanding of the formation and transport of small polarons is still very limited. Examples discussed in this review demonstrated that factors that can negatively affect the carrier transport in a semiconductor whose conduction is through the CB can result in an increase in the bulk separation efficiency of an oxide-based semiconductor whose transport is through small polaron hopping. Future studies that can enhance our understanding of small polaron-based transport and provide rational strategies to further enhance charge transport properties of oxide-based photoanodes are imperative.

$BiVO_4$ stands out from other oxide-based photoanodes due to its unusually high bulk charge separation efficiency (~100% at 1.23 V vs. RHE). Thus, $BiVO_4$ can be used as the foundation to pursue two different research directions. The first is to obtain a better understanding of the key features of $BiVO_4$ that are responsible for its high bulk separation efficiency. This knowledge can be used to develop materials with new compositions that can achieve comparable bulk separation while achieving a lower bandgap energy than $BiVO_4$. The second approach is to develop $BiVO_4$-based photoanodes where high surface area $BiVO_4$ is coupled with one or two additional photoanodes that have smaller bandgaps than $BiVO_4$. The smaller bandgap semiconductors can be deposited as extremely thin layers to maximize their bulk separation. The use of high surface area $BiVO_4$ as the substrate will ensure that even if these smaller bandgap semiconductors are deposited as extremely thin layers, they can absorb a sufficient amount of photons to significantly increase the photocurrent generation.

Although many challenges still remain, an increase in the scope of oxide-based materials that have been investigated and the strategies and knowledge accumulated to overcome their

limitations will further accelerate the development of oxide-based photoanodes. We would like to conclude our review by acknowledging the efforts of all the research groups that have made a significant contribution to the advancement of oxide-based PECs. We wish them the best of luck in their future studies.

List of Abbreviations

α: absorption coefficient
α^{-1}: light penetration depth
δ: inversion degree
A_{corr}: reflectance-corrected absorbance
ABPE: applied bias photon-to-current efficiency
ALD: atomic layer deposition
AM 1.5G: Air mass 1.5G illumination (100 mW/cm^2)
APCE: absorbed photon-to-current efficiency
CBM: conduction band minimum
CV: cyclic voltammogram
CVD: chemical vapor deposition
DFT: density functional theory
EDS: energy dispersive X-ray spectroscopy
E_{FB}: flatband potential
EIS: electrochemical impedance spectroscopy
EPMA: electron probe micro-analysis
FTO: fluorine-doped tin oxide
FWHM: full width at half maximum
HRTEM: high-resolution transmission electron microscopy
IMPS: intensity-modulated photocurrent spectroscopy
IO: inverse opal
IPCE: incident photon-to-current efficiency
ITO: indium-doped tin oxide
J_{abs}: expected photocurrent density using absorbance spectra
J_{op}: operating current density
J-t: current density-time
J-V: current density-potential
J_{PEC}: measured photocurrent density
$k_{ox:}$ rate constant for water oxidation
k_{rec}: rate constant for surface recombination
LSV: linear sweep voltammogram
MWCNT: multi-walled carbon nanotubes
OCP: open circuit potential
OEC: oxygen evolution catalyst
O_h: octahedral
η_{bulk}/η_{sep}: bulk separation efficiency
$\eta_{ox}/\eta_{surface}$: charge injection efficiency (or surface separation efficiency)
PEC: photoelectrochemical cell

PT: particle transfer
RHE: reversible hydrogen electrode
SEM: scanning electron microscopy
STH: solar-to-hydrogen
T_d: tetrahedral
TEM: transmission electron microscopy
TGA: thermogravimetric analysis
TRMC: time-resolved microwave conductivity
UPS: ultraviolet photoelectron spectroscopy
VBM: valence band maximum
XPS: X-ray photoelectron spectroscopy
XRD: X-ray diffraction
XRF: X-ray fluorescence

Conflicts of interest

There are no conflicts to declare

Acknowledgements

This work was supported by the Division of Chemical Sciences, Geosciences, and Biosciences, Office of Basic Energy Sciences of the U.S. Department of Energy through Grant DE-SC0008707.

References

1. A. Fujishima and K. Honda, *Nature*, 1972, **238**, 37-38.
2. A. J. Nozik, *Annu. Rev. Phys. Chem.*, 1978, **29**, 189-222.
3. M. Grätzel, *Nature*, 2001, **414**, 338-344.
4. J. A. Turner, *Science*, 2004, **305**, 972-974.
5. M. G. Walter, E. L. Warren, J. R. McKone, S. W. Boettcher, Q. Mi, E. A. Santori and N. S. Lewis, *Chem. Rev.*, 2010, **110**, 6446-6473.
6. T. Bak, J. Nowotny, M. Rekas and C. C. Sorrell, *Int. J. Hydrogen Energy*, 2002, **27**, 991-1022.
7. L. Fornarini, A. J. Nozik and B. A. Parkinson, *J. Phys. Chem.*, 1984, **88**, 3238-3243.
8. The American Society for Testing and Materials (ASTM) G-173 spectra, https://www.nrel.gov/grid/solar-resource/spectra-am1.5.html
9. R. E. Hummel, in *Electronic Properties of Materials*, Springer, Newyork NY, 4th edn., 2011, ch. 10 The Optical Constants, pp. 215-225.
10. H. Dotan, K. Sivula, M. Grätzel, A. Rothschild and S. C. Warren, *Energy Environ. Sci.*, 2011, **4**, 958-964.
11. J. M. Foley, M. J. Price, J. I. Feldblyum and S. Maldonado, *Energy Environ. Sci.*, 2012, **5**, 5203-5220.
12. M. Zhou, J. Bao, W. Bi, Y. Zeng, R. Zhu, M. Tao and Y. Xie, *ChemSusChem*, 2012, **5**, 1420-1425.
13. G. V. Govindaraju, G. P. Wheeler, D. Lee and K.-S. Choi, *Chem. Mater.*, 2017, **29**, 355-370.
14. K. Lark-Horovitz and V. A. Johnson, in *Solid State Physics PART B Electrical, Magnetic, and Optical Properties* Academic Press, Newyork and London, 1959, vol. 6, ch. 12 Photoelectric Phenomena, pp. 393-406.
15. K. Sivula and R. van de Krol, *Nat. Rev. Mater.*, 2016, **1**, 15010.
16. D. H. Taffa, R. Dillert, A. C. Ulpe, K. C. L. Bauerfeind, T. Bredow, D. W. Bahnemann and M. Wark, *J. Photon. Energy*, 2016, **7**, 012009.
17. X. Xu, A. K. Azad and J. T. S. Irvine, *Catal. Today*, 2013, **199**, 22-26.
18. P. H. Borse, J. S. Jang, S. J. Hong, J. S. Lee, J. H. Jung, T. E. Hong, C. W. Ahn, E. D. Jeong, K. S. Hong, J. H. Yoon and H. G. Kim, *J. Korean Phy. Soc.*, 2009, **55**, 1472~1477.
19. S. D. Tilley, M. Cornuz, K. Sivula and M. Grätzel, *Angew. Chem. Int. Ed.*, 2010, **49**, 6405-6408.
20. J. H. Kim, J.-W. Jang, Y. H. Jo, F. F. Abdi, Y. H. Lee, R. van de Krol and J. S. Lee, *Nat. Commun.*, 2016, **7**, 13380.
21. L. G. J. De Haart and G. Blasse, *Solid State Ionics*, 1985, **16**, 137-139.
22. A. A. Tahir and K. G. U. Wijayantha, *J. Photochem. Photobiol. A*, 2010, **216**, 119-125.
23. J. H. Kim, J. H. Kim, J.-W. Jang, J. Y. Kim, S. H. Choi, G. Magesh, J. Lee and J. S. Lee, *Adv. Energy Mater.*, 2015, **5**, 1401933.
24. J. H. Kim, Y. J. Jang, J. H. Kim, J.-W. Jang, S. H. Choi and J. S. Lee, *Nanoscale*, 2015, **7**, 19144-19151.
25. N. Guijarro, P. Bornoz, M. Prévot, X. Yu, X. Zhu, M. Johnson, X. Jeanbourquin, F. Le Formal and K. Sivula, *Sustainable Energy Fuels*, 2018, **2**, 103-117.

26. J. H. Kim, Y. J. Jang, S. H. Choi, B. J. Lee, J. H. Kim, Y. B. Park, C.-M. Nam, H. G. Kim and J. S. Lee, *J. Mater. Chem. A*, 2018, **6**, 12693-12700.
27. X. Zhu, N. Guijarro, Y. Liu, P. Schouwink, R. A. Wells, F. Formal, S. Sun, C. Gao and K. Sivula, *Adv. Mater.*, 2018, **30**, 1801612.
28. A. G. Hufnagel, K. Peters, A. Müller, C. Scheu, D. Fattakhova-Rohlfing and T. Bein, *Adv. Funct. Mater.*, 2016, **26**, 4435-4443.
29. Y. Guo, N. Zhang, X. Wang, Q. Qian, S. Zhang, Z. Li and Z. Zou, *J. Mater. Chem. A*, 2017, **5**, 7571-7577.
30. K. Itoh and J. O. M. Bockris, *J. Electrochem. Soc.*, 1984, **131**, 1266-1271.
31. Y. Hou, X.-Y. Li, Q.-D. Zhao, X. Quan and G.-H. Chen, *Adv. Funct. Mater.*, 2010, **20**, 2165-2174.
32. Y.-F. Xu, H.-S. Rao, X.-D. Wang, H.-Y. Chen, D.-B. Kuang and C.-Y. Su, *J. Mater. Chem. A*, 2016, **4**, 5124-5129.
33. Z. Luo, C. Li, D. Zhang, T. Wang and J. Gong, *Chem. Commun.*, 2016, **52**, 9013-9015.
34. K. J. McDonald and K.-S. Choi, *Chem. Mater.*, 2011, **23**, 4863-4869.
35. T. W. Kim and K.-S. Choi, *J. Phys. Chem. Lett.*, 2016, **7**, 447-451.
36. R. L. Spray, K. J. McDonald and K.-S. Choi, *J. Phys. Chem. C*, 2011, **115**, 3497-3506.
37. D. Ravinder, *J. Alloys Compd.*, 1999, **291**, 208-214.
38. R. F. G. Gardner, F. Sweett and D. W. Tanner, *J. Phys. Chem. Solids*, 1963, **24**, 1175-1181.
39. F. A. Benko and F. P. Koffyberg, *Mater. Res. Bull.*, 1986, **21**, 1183-1188.
40. Y. Hou, F. Zuo, A. Dagg and P. Feng, *Angew. Chem. Int. Ed.*, 2013, **52**, 1248-1252.
41. H. G. Kim, P. H. Borse, J. S. Jang, E. D. Jeong, O.-S. Jung, Y. J. Suh and J. S. Lee, *Chem. Commun.*, 2009, **0**, 5889-5891.
42. R. Dom, P. H. Borse, K.-S. Hong, S. Choi, B. S. Lee, M. G. Ha, J. P. Kim, E. D. Jeong and H. G. Kim, *J. Korean Phys. Soc.*, 2015, **67**, 1639-1645.
43. T. Tsoncheva, E. Manova, N. Velinov, D. Paneva, M. Popova, B. Kunev, K. Tenchev and I. Mitov, *Catal. Commun.*, 2010, **12**, 105-109.
44. A. M. Balagurov, I. A. Bobrikov, M. S. Maschenko, D. Sangaa and V. G. Simkin, *Crystallography Rep.*, 2013, **58**, 710-717.
45. H. Yang, J. Yan, Z. Lu, X. Cheng and Y. Tang, *J. Alloys Compd.*, 2009, **476**, 715-719.
46. C. Michel, J.-M. Moreau, G. D. Achenbach, R. Gerson and W. J. James, *Solid State Commun.*, 1969, **7**, 701-704.
47. Q. Liu, Y. Zhou, L. You, J. Wang, M. Shen and L. Fang, *Appl. Phys. Lett.*, 2016, **108**, 022902.
48. S. J. A. Moniz, C. S. Blackman, P. Southern, P. M. Weaver, J. Tang and C. J. Carmalt, *Nanoscale*, 2015, **7**, 16343-16353.
49. J. Song, T. L. Kim, J. Lee, S. Y. Cho, J. Cha, S. Y. Jeong, H. An, W. S. Kim, Y.-S. Jung, J. Park, G. Y. Jung, D.-Y. Kim, J. Y. Jo, S. D. Bu, H. W. Jang and S. Lee, *Nano Res.*, 2018, **11**, 642-655.
50. N. Rong, M. Chu, Y. Tang, C. Zhang, X. Cui, H. He, Y. Zhang and P. Xiao, *J. Mater. Sci.*, 2016, **51**, 5712-5723.
51. T. R. Paudel, S. S. Jaswal and E. Y. Tsymbal, *Phys. Rev. B*, 2012, **85**, 104409.
52. T. Rojac, A. Bencan, G. Drazic, N. Sakamoto, H. Ursic, B. Jancar, G. Tavcar, M. Makarovic, J. Walker, B. Malic and D. Damjanovic, *Nat. Mater.*, 2016, **16**, 322-327.

53. W. Ji, K. Yao, Y.-F. Lim, Y. C. Liang and A. Suwardi, *Appl. Phys. Lett.*, 2013, **103**, 062901.
54. D. Cao, Z. Wang, Nasori, L. Wen, Y. Mi and Y. Lei, *Angew. Chem.*, 2014, **126**, 11207-11211.
55. Y.-L. Huang, W. S. Chang, C. N. Van, H.-J. Liu, K.-A. Tsai, J.-W. Chen, H.-H. Kuo, W.-Y. Tzeng, Y.-C. Chen, C.-L. Wu, C.-W. Luo, Y.-J. Hsu and Y.-H. Chu, *Nanoscale*, 2016, **8**, 15795-15801.
56. S. Wang, P. Chen, J.-H. Yun, Y. Hu and L. Wang, *Angew. Chem. Int. Ed.*, 2017, **56**, 8500-8504.
57. Y. Gao, O. Zandi and T. W. Hamann, *J. Mater. Chem. A*, 2016, **4**, 2826-2830.
58. J. E. Yourey and B. M. Bartlett, *J. Mater. Chem.*, 2011, **21**, 7651-7660.
59. J. E. Yourey, K. J. Pyper, J. B. Kurtz and B. M. Bartlett, *J. Phys. Chem. C*, 2013, **117**, 8708-8718.
60. J. C. Hill and K.-S. Choi, *J. Mater. Chem. A*, 2013, **1**, 5006-5014.
61. C. R. Lhermitte and B. M. Bartlett, *Acc. Chem. Res.*, 2016, **49**, 1121-1129.
62. M. Pourbaix, *Atlas of electrochemical equilibria in aqueous solutions*, National Association of Corrosion Engineers, Houston TX, 1974.
63. D. Bohra and W. A. Smith, *Phys. Chem. Chem. Phys.*, 2015, **17**, 9857-9866.
64. A. Theuwis, I. E. Vermeir and W. P. Gomes, *J. Electroanal. Chem.*, 1996, **410**, 31-42.
65. Y. Gao and T. W. Hamann, *Chem. Commun.*, 2017, **53**, 1285-1288.
66. K. M. Nam, E. A. Cheon, W. J. Shin and A. J. Bard, *Langmuir*, 2015, **31**, 10897-10903.
67. J. E. Yourey, J. B. Kurtz and B. M. Bartlett, *Inorg. Chem.*, 2012, **51**, 10394-10401.
68. Y. Tang, N. Rong, F. Liu, M. Chu, H. Dong, Y. Zhang and P. Xiao, *Appl. Surf. Sci.*, 2016, **361**, 133-140.
69. D. Hu, P. Diao, D. Xu, M. Xia, Y. Gu, Q. Wu, C. Li and S. Yang, *Nanoscale*, 2016, **8**, 5892-5901.
70. N. Gaillard, Y. Chang, A. Deangelis, S. Higgins and A. Braun, *Int. J. Hydrogen Energy*, 2013, **38**, 3166-3176.
71. D. Peeters, O. Mendoza Reyes, L. Mai, A. Sadlo, S. Cwik, D. Rogalla, H. Schütz, H.-W. Becker, J. Hirst, S. Müller, D. Friedrich, D. Mitoraj, M. Nagli, M. Caspary Toroker, R. Eichberger, R. Beranek and A. Devi, *J. Mater. Chem. A*, 2018, **6**, 10206-10216.
72. W. Ye, F. Chen, F. Zhao, N. Han and Y. Li, *ACS Appl. Mater. Inter.*, 2016, **8**, 9211-9217.
73. K. J. Pyper, J. E. Yourey and B. M. Bartlett, *J. Phys. Chem. C*, 2013, **117**, 24726-24732.
74. Y. Gao and T. W. Hamann, *J. Phys. Chem. Lett.*, 2017, **8**, 2700-2704.
75. J. C. Hill, Y. Ping, G. A. Galli and K.-s. Choi, *Energy Environ. Sci.*, 2013, **6**, 2440-2446.
76. K. J. Pyper, T. C. Evans and B. M. Bartlett, *Chin. Chem. Lett.*, 2015, **26**, 474-478.
77. M. Harb, A. Ziani and K. Takanabe, *Phys. Status Solidi B*, 2016, **253**, 1115-1119.
78. I.-s. Cho, C. H. Kwak, D. W. Kim, S. Lee and K. S. Hong, *J. Phys. Chem. C*, 2009, **113**, 10647-10653.
79. Z. Zhu, P. Sarker, C. Zhao, L. Zhou, R. L. Grimm, M. N. Huda and P. M. Rao, *ACS Appl. Mater. Inter.*, 2017, **9**, 1459-1470.
80. A. Ziani, M. Harb, D. Noureldine and K. Takanabe, *APL Mater.*, 2015, **3**, 096101-096101.
81. Y. Hosogi, Y. Shimodaira, H. Kato, H. Kobayashi and A. Kudo, *Chem. Mater.*, 2008, **20**, 1299-1307.

82. D. Noureldine, D. H. Anjum and K. Takanabe, *Phys. Chem. Chem. Phys.*, 2014, **16**, 10762-10769.
83. J. Solis, J. Frantti, V. Lantto, L. Häggström and M. Wikner, *Phys. Rev. B*, 1998, **57**, 13491-13500.
84. M. M. Khader, M. M. Saleh and M. E. El-Naggar, *J. Solid State Electrochem.*, 1998, **2**, 170-175.
85. F. F. Abdi, A. Chemseddine, S. P. Berglund and R. Van De Krol, *J. Phys. Chem. C*, 2017, **121**, 153-160.
86. K. J. McDonald and K.-S. Choi, *Energy Environ. Sci.*, 2012, **5**, 8553-8557.
87. T. W. Kim and K.-S. Choi, *Science*, 2014, **343**, 990-994.
88. Y. Park, D. Kang and K.-S. Choi, *Phys. Chem. Chem. Phys.*, 2014, **16**, 1238-1246.
89. T. W. Kim, Y. Ping, G. A. Galli and K.-S. Choi, *Nat. Commun.*, 2015, **6**, 8769.
90. J. H. Kim, Y. Jo, J. H. Kim, J. W. Jang, H. J. Kang, Y. H. Lee, D. S. Kim, Y. Jun and J. S. Lee, *ACS Nano*, 2015, **9**, 11820-11829.
91. C. Ding, J. Shi, D. Wang, Z. Wang, N. Wang, G. Liu, F. Xiong and C. Li, *Phys. Chem. Chem. Phys.*, 2013, **15**, 4589-4595.
92. A. J. E. Rettie, H. C. Lee, L. G. Marshall, J.-F. Lin, C. Capan, J. Lindemuth, J. S. McCloy, J. Zhou, A. J. Bard and C. B. Mullins, *J. Am. Chem. Soc.*, 2013, **135**, 11389-11396.
93. Y. Qiu, W. Liu, W. Chen, W. Chen, G. Zhou, P.-C. Hsu, R. Zhang, Z. Liang, S. Fan, Y. Zhang and Y. Cui, *Sci. Adv.*, 2016, **2**.
94. D. K. Lee and K.-S. Choi, *Nat. Energy*, 2018, **3**, 53-60.
95. Y. Kuang, Q. Jia, H. Nishiyama, T. Yamada, A. Kudo and K. Domen, *Adv. Energy Mater.*, 2015, **6**, 1501645.
96. S. Xiao, C. Hu, H. Lin, X. Meng, Y. Bai, T. Zhang, Y. Yang, Y. Qu, K. Yan, J. Xu, Y. Qiu and S. Yang, *J. Mater. Chem. A*, 2017, **5**, 19091-19097.
97. F. F. Abdi, L. Han, A. H. M. Smets, M. Zeman, B. Dam and R. van de Krol, *Nat. Commun.*, 2013, **4**, 2195.
98. L. Han, F. F. Abdi, R. van de Krol, R. Liu, Z. Huang, H.-J. Lewerenz, B. Dam, M. Zeman and A. H. M. Smets, *ChemSusChem*, 2014, **7**, 2832-2838.
99. L. Pan, J. H. Kim, M. T. Mayer, M.-K. Son, A. Ummadisingu, J. S. Lee, A. Hagfeldt, J. Luo and M. Grätzel, *Nat. Catal.*, 2018, **1**, 412-420.
100. Y.-S. Chen, J. S. Manser and P. V. Kamat, *J. Am. Chem. Soc.*, 2015, **137**, 974-981.
101. C. Ding, W. Qin, N. Wang, G. Liu, Z. Wang, P. Yan, J. Shi and C. Li, *Phys. Chem. Chem. Phys.*, 2014, **16**, 15608-15614.
102. P. Chakthranont, T. R. Hellstern, J. M. McEnaney and T. F. Jaramillo, *Adv. Energy Mater.*, 2017, **7**, 1701515.
103. N. Kornienko, N. A. Gibson, H. Zhang, S. W. Eaton, Y. Yu, S. Aloni, S. R. Leone and P. Yang, *ACS Nano*, 2016, **10**, 5525-5535.
104. Y. Peng, G. V. Govindaraju, D. K. Lee, K.-S. Choi and T. L. Andrew, *ACS Appl. Mater. Inter.*, 2017, **9**, 22449-22455.
105. J. H. Kim, S. Han, Y. H. Jo, Y. Bak and J. S. Lee, *J. Mater. Chem. A*, 2018, **6**, 1266-1274.
106. P. Bornoz, F. F. Abdi, S. D. Tilley, B. Dam, R. van de Krol, M. Graetzel and K. Sivula, *J. Phys. Chem. C*, 2014, **118**, 16959-16966.

107. Q. Wang, T. Hisatomi, Q. Jia, H. Tokudome, M. Zhong, C. Wang, Z. Pan, T. Takata, M. Nakabayashi, N. Shibata, Y. Li, I. D. Sharp, A. Kudo, T. Yamada and K. Domen, *Nat. Mater.*, 2016, **15**, 611.
108. S. Wang, P. Chen, Y. Bai, J.-H. Yun, G. Liu and L. Wang, *Adv. Mater.*, 2018, **30**, 1800486.
109. Y. Kuang, Q. Jia, G. Ma, T. Hisatomi, T. Minegishi, H. Nishiyama, M. Nakabayashi, N. Shibata, T. Yamada, A. Kudo and K. Domen, *Nat. Energy*, 2016, **2**, 16191.
110. Y. Park, K. J. McDonald and K.-S. Choi, *Chem. Soc. Rev.*, 2013, **42**, 2321-2337.
111. F. F. Abdi, T. J. Savenije, M. M. May, B. Dam and R. van de Krol, *J. Phys. Chem. Lett.*, 2013, **4**, 2752-2757.
112. R. A. Pala, A. J. Leenheer, M. Lichterman, H. A. Atwater and N. S. Lewis, *Energy Environ. Sci.*, 2014, **7**, 3424-3430.
113. J.-W. Jang, D. Friedrich, S. Müller, M. Lamers, H. Hempel, S. Lardhi, Z. Cao, M. Harb, L. Cavallo, R. Heller, R. Eichberger, R. van de Krol and F. F. Abdi, *Adv. Energy Mater.*, 2017, **7**, 1701536.
114. H. S. Park, K. E. Kweon, H. Ye, E. Paek, G. S. Hwang and A. J. Bard, *J. Phys. Chem. C*, 2011, **115**, 17870-17879.
115. C. Jiang, R. Wang and B. A. Parkinson, *ACS Comb. Sci.*, 2013, **15**, 639-645.
116. K. P. S. Parmar, H. J. Kang, A. Bist, P. Dua, J. S. Jang and J. S. Lee, *ChemSusChem*, 2012, **5**, 1926-1934.
117. S. P. Berglund, A. J. E. Rettie, S. Hoang and C. B. Mullins, *Phys. Chem. Chem. Phys.*, 2012, **14**, 7065-7075.
118. W. Luo, Z. Yang, Z. Li, J. Zhang, J. Liu, Z. Zhao, Z. Wang, S. Yan, T. Yu and Z. Zou, *Energy Environ. Sci.*, 2011, **4**, 4046-4051.
119. W. Zhang, F. Wu, J. Li, D. Yan, J. Tao, Y. Ping and M. Liu, *ACS Energy Lett.*, 2018, **3**, 2232-2239.
120. G. V. Govindaraju, J. M. Morbec, G. A. Galli and K.-S. Choi, *J. Phys. Chem. C*, 2018, **122**, 19416-19424.
121. G. Wang, Y. Ling, X. Lu, F. Qian, Y. Tong, J. Z. Zhang, V. Lordi, C. Rocha Leao and Y. Li, *J. Phys. Chem. C*, 2013, **117**, 10957-10964.
122. J. K. Cooper, S. B. Scott, Y. Ling, J. Yang, S. Hao, Y. Li, F. M. Toma, M. Stutzmann, K. V. Lakshmi and I. D. Sharp, *Chem. Mater.*, 2016, **28**, 5761-5771.
123. S. M. Bhaway, K. Kisslinger, L. Zhang, K. G. Yager, A. L. Schmitt, M. K. Mahanthappa, A. Karim and B. D. Vogt, *ACS Appl. Mater. Inter.*, 2014, **6**, 19288-19298.
124. D. Liu, Y. Liu, B. B. Garcia, Q. Zhang, A. Pan, Y.-H. Jeong and G. Cao, *J. Mater. Chem.*, 2009, **19**, 8789-8795.
125. R. W. Daniele Ielmini, in *Resistive Switching: From Fundamentals of Nanoionic Redox Processes to Memristive Device Applications*, Wiley, 2015, ch. 6 Electrical Transport in Transition Metal Oxides, pp. 165-196.
126. L. Zhang, X. Ye, M. Boloor, A. Poletayev, N. A. Melosh and W. C. Chueh, *Energy Environ. Sci.*, 2016, **9**, 2044-2052.
127. P. Singh and N. M. Ravindra, *Sol. Energy Mater. Sol. Cells*, 2012, **101**, 36-45.
128. C. Jacoboni, in *Theory of Electron Transport in Semiconductors: A Pathway from Elementary Physics to Nonequilibrium Green Functions*, Springer, Berlin, 2010, ch. 9 Electronic Interactions, pp. 127-161.
129. D. K. Zhong, S. Choi and D. R. Gamelin, *J. Am. Chem. Soc.*, 2011, **133**, 18370-18377.

130. J. A. Seabold and K. S. Choi, *J. Am. Chem. Soc.*, 2012, **134**, 2186-2192.
131. R. Li, H. Han, F. Zhang, D. Wang and C. Li, *Energy Environ. Sci.*, 2014, **7**, 1369-1376.
132. S. K. Choi, W. Choi and H. Park, *Phys. Chem. Chem. Phys.*, 2013, **15**, 6499-6507.
133. J. H. Kim, J. W. Jang, H. J. Kang, G. Magesh, J. Y. Kim, J. H. Kim, J. Lee and J. S. Lee, *J. Catal.*, 2014, **317**, 126-134.
134. D. Guevarra, A. Shinde, S. K. Suram, I. D. Sharp, F. M. Toma, J. A. Haber and J. M. Gregoire, *Energy Environ. Sci.*, 2016, **9**, 565-580.
135. Y. Ma, F. Le Formal, A. Kafizas, S. R. Pendlebury and J. R. Durrant, *J. Mater. Chem. A*, 2015, **3**, 20649-20657.
136. C. Zachäus, F. F. Abdi, L. M. Peter and R. van de Krol, *Chem. Sci.*, 2017, **8**, 3712-3719.
137. M. R. Nellist, F. A. L. Laskowski, J. Qiu, H. Hajibabaei, K. Sivula, T. W. Hamann and S. W. Boettcher, *Nat. Energy*, 2018, **3**, 46-52.
138. L. M. Peter, K. G. U. Wijayantha and A. A. Tahir, *Faraday Discuss.*, 2012, **155**, 309-322.
139. F. M. Toma, J. K. Cooper, V. Kunzelmann, M. T. McDowell, J. Yu, D. M. Larson, N. J. Borys, C. Abelyan, J. W. Beeman, K. M. Yu, J. Yang, L. Chen, M. R. Shaner, J. Spurgeon, F. A. Houle, K. A. Persson and I. D. Sharp, *Nat. Commun.*, 2016, **7**, 12012.
140. M. T. McDowell, M. F. Lichterman, J. M. Spurgeon, S. Hu, I. D. Sharp, B. S. Brunschwig and N. S. Lewis, *J. Phys. Chem. C*, 2014, **118**, 19618-19624.
141. M. F. Lichterman, M. R. Shaner, S. G. Handler, B. S. Brunschwig, H. B. Gray, N. S. Lewis and J. M. Spurgeon, *J. Phys. Chem. Lett.*, 2013, **4**, 4188-4191.
142. D. Lee, A. Kvit and K.-S. Choi, *Chem. Mater.*, 2018, **30**, 4704-4712.
143. Y. Pihosh, I. Turkevych, K. Mawatari, T. Asai, T. Hisatomi, J. Uemura, M. Tosa, K. Shimamura, J. Kubota, K. Domen and T. Kitamori, *Small*, 2014, **10**, 3692-3699.
144. L. C. Seitz, Z. Chen, A. J. Forman, B. A. Pinaud, J. D. Benck and T. F. Jaramillo, *ChemSusChem*, 2014, **7**, 1372-1385.
145. M. S. Prévot and K. Sivula, *J. Phys. Chem. C*, 2013, **117**, 17879-17893.
146. J. H. Montoya, L. C. Seitz, P. Chakthranont, A. Vojvodic, T. F. Jaramillo and J. K. Nørskov, *Nat. Mater.*, 2016, **16**, 70.
147. J. A. Seabold and N. R. Neale, *Chem. Mater.*, 2015, **27**, 1005-1013.
148. C.-M. Jiang, M. Farmand, C. H. Wu, Y.-S. Liu, J. Guo, W. S. Drisdell, J. K. Cooper and I. D. Sharp, *Chem. Mater.*, 2017, **29**, 3334-3345.
149. L. Zhou, Q. Yan, A. Shinde, D. Guevarra, P. F. Newhouse, N. Becerra-Stasiewicz, S. M. Chatman, J. A. Haber, J. B. Neaton and J. M. Gregoire, *Adv. Energy Mater.*, 2015, **5**, 1500968-1500968.
150. P. F. Newhouse, D. A. Boyd, A. Shinde, D. Guevarra, L. Zhou, E. Soedarmadji, G. Li, J. B. Neaton and J. M. Gregoire, *J. Mater. Chem. A*, 2016, **4**, 7483-7494.
151. W. Guo, W. D. Chemelewski, O. Mabayoje, P. Xiao, Y. Zhang and C. B. Mullins, *J. Phys. Chem. C*, 2015, **119**, 27220-27227.
152. M.-w. Kim, B. Joshi, H. Yoon, T. Y. Ohm, K. Kim, S. S. Al-Deyab and S. S. Yoon, *J. Alloys Compd.*, 2017, **708**, 444-450.
153. I. Khan and A. Qurashi, *Sci. Rep.*, 2017, **7**, 14370-14370.
154. D. Cardenas-Morcoso, A. Peiro-Franch, I. Herraiz-Cardona and S. Gimenez, *Catal. Today*, 2017, **290**, 65-72.
155. M. A. Lumley and K.-S. Choi, *Chem. Mater.*, 2017, **29**, 9472-9479.

156. C.-M. Jiang, G. Segev, L. H. Hess, G. Liu, G. Zaborski, F. M. Toma, J. K. Cooper and I. D. Sharp, *ACS Appl. Mater. Inter.*, 2018, **10**, 10627-10633.
157. H. Ye, H. S. Park and A. J. Bard, *J. Phys. Chem. C*, 2011, **115**, 12464-12470.
158. A. C. Cardiel, K. J. McDonald and K.-S. Choi, *Langmuir*, 2017, **33**, 9262-9270.
159. L. Zhou, Q. Yan, J. Yu, R. J. R. Jones, N. Becerra-Stasiewicz, S. K. Suram, A. Shinde, D. Guevarra, J. B. Neaton, K. A. Persson and J. M. Gregoire, *Phys. Chem. Chem. Phys.*, 2016, **18**, 9349-9352.
160. T. Arai, Y. Konishi, Y. Iwasaki, H. Sugihara and K. Sayama, *J. Comb. Chem.*, 2007, **9**, 574-581.
161. B. Robertson and E. Kostiner, *J. Solid State Chem.*, 1972, **4**, 29-37.
162. C. D. Morton, I. J. Slipper, M. J. K. Thomas and B. D. Alexander, *J. Photochem. Photobiol. A*, 2010, **216**, 209-214.
163. S. K. Biswas and J.-O. Baeg, *Int. J. Hydrogen Energy*, 2013, **38**, 14451-14457.
164. W. Wang, Y. Zhang, L. Wang and Y. Bi, *J. Mater. Chem. A*, 2017, **5**, 2478-2482.
165. M. Zhang, Y. Ma, D. Friedrich, R. van de Krol, L. H. Wong and F. F. Abdi, *J. Mater. Chem. A*, 2018, **6**, 548-555.
166. M. Balamurugan, G. Yun, K.-S. Ahn and S. H. Kang, *J. Phys. Chem. C*, 2017, **121**, 7625-7634.
167. H. Mandal, S. Shyamal, P. Hajra, A. Bera, D. Sariket, S. Kundu and C. Bhattacharya, *RSC Adv.*, 2016, **6**, 4992-4999.
168. D. Tang, A. J. E. Rettie, O. Mabayoje, B. R. Wygant, Y. Lai, Y. Liu and C. B. Mullins, *J. Mater. Chem. A*, 2016, **4**, 3034-3042.
169. X. An, H. Lan, R. Liu, H. Liu and J. Qu, *New J. Chem.*, 2017, **41**, 7966-7971.
170. B. Morosin, R. J. Baughman, D. S. Ginley and M. A. Butler, *J. Appl. Cryst.*, 1978, **11**, 121-124.
171. P. S. Bassi, S. Y. Chiam, Gurudayal, J. Barber and L. H. Wong, *ACS Appl. Mater. Inter.*, 2014, **6**, 22490-22495.
172. D. S. Ginley and M. A. Butler, *J. Appl. Phys.*, 1977, **48**, 2019-2021.
173. H. Kozuka and M. Kajimura, *J. Sol-Gel Sci. Technol.*, 2001, **22**, 125-132.
174. C. Li, T. Wang, Z. Luo, S. Liu and J. Gong, *Small*, 2016, **12**, 3415-3422.
175. E. Courtin, G. Baldinozzi, M. T. Sougrati, L. Stievano, C. Sanchez and C. Laberty-Robert, *J. Mater. Chem. A*, 2014, **2**, 6567-6577.
176. H. Zhang, J. H. Kim, J. H. Kim and J. S. Lee, *Adv. Funct. Mater.*, 2017, **27**, 1-9.
177. J. Deng, X. Lv, J. Liu, H. Zhang, K. Nie, C. Hong, J. Wang, X. Sun, J. Zhong and S.-T. Lee, *ACS Nano*, 2015, **9**, 5348-5356.
178. S. Kment, F. Riboni, S. Pausova, L. Wang, L. Wang, H. Han, Z. Hubicka, J. Krysa, P. Schmuki and R. Zboril, *Chem. Soc. Rev.*, 2017, **46**, 3716-3769.
179. D. Eisenberg, H. S. Ahn and A. J. Bard, *J. Am. Chem. Soc.*, 2014, **136**, 14011-14014.
180. T. Hisatomi, H. Dotan, M. Stefik, K. Sivula, A. Rothschild, M. Grätzel and N. Mathews, *Adv. Mater.*, 2012, **24**, 2699-2702.
181. Q. Liu, J. He, T. Yao, Z. Sun, W. Cheng, S. He, Y. Xie, Y. Peng, H. Cheng, Y. Sun, Y. Jiang, F. Hu, Z. Xie, W. Yan, Z. Pan, Z. Wu and S. Wei, *Nat. Commun.*, 2015, **5**, 1-7.
182. L. Wang, N. T. Nguyen and P. Schmuki, *ChemSusChem*, 2016, **9**, 2048-2053.
183. T.-P. Ruoko, K. Kaunisto, M. Bärtsch, J. Pohjola, A. Hiltunen, M. Niederberger, N. V. Tkachenko and H. Lemmetyinen, *J. Phys. Chem. Lett.*, 2015, **6**, 2859-2864.

184. F. Le Formal, N. Tétreault, M. Cornuz, T. Moehl, M. Grätzel and K. Sivula, *Chem. Sci.*, 2011, **2**, 737-743.
185. Y. Hosogi, K. Tanabe, H. Kato, H. Kobayashi and A. Kudo, *Chem. Lett.*, 2004, **33**, 28-29.
186. R. Niishiro, Y. Takano, Q. Jia, M. Yamaguchi, A. Iwase, Y. Kuang, T. Minegishi, T. Yamada, K. Domen and A. Kudo, *Chem. Commun.*, 2017, **53**, 629-632.
187. S. Liang, R. Liang, L. Wen, R. Yuan, L. Wu and X. Fu, *Appl. Catal., B*, 2012, **125**, 103-110.
188. S. Katayama, H. Hayashi, Y. Kumagai, F. Oba and I. Tanaka, *J. Phys. Chem. C*, 2016, **120**, 9604-9611.
189. S. W. Seo, T. H. Noh, S. Park, C. W. Lee, S. H. Kim, H. J. Kim, H. K. Park and K. S. Hong, *Int. J. Hydrogen Energy*, 2014, **39**, 17517-17523.
190. C. Zhou, Y. Zhao, L. Shang, R. Shi, L. Z. Wu, C. H. Tung and T. Zhang, *Chem. Commun.*, 2016, **52**, 8239-8242.
191. Y. Hosogi, H. Kato and A. Kudo, *Chem. Lett.*, 2006, **35**, 578-579.
192. D. Noureldine and K. Takanabe, *Catalysis Science and Technology*, 2016, **6**, 7656-7670.
193. S. Uma, J. Singh and V. Thakral, *Inorg. Chem.*, 2009, **48**, 11624-11630.
194. T. Minegishi, N. Nishimura, J. Kubota and K. Domen, *Chem. Sci.*, 2013, **4**, 1120-1124.
195. S. Xun, Z. Zhang, T. Wang, D. Jiang and H. Li, *J. Alloys Compd.*, 2016, **685**, 647-655.
196. S. Zhu, S. Liang, J. Bi, M. Liu, L. Zhou, L. Wu and X. Wang, *Green Chem.*, 2016, **18**, 1355-1363.

TOC ENTRY

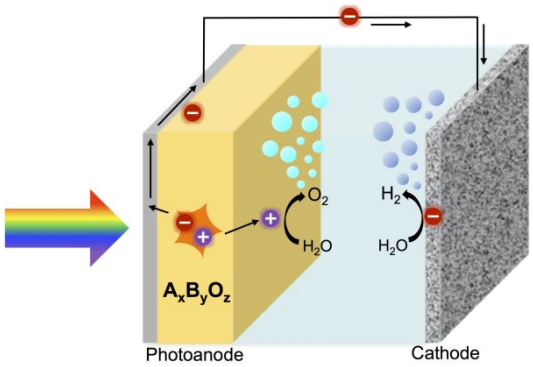

Advancements made in the development of ternary oxide-based photoanodes for use in water splitting photoelectrochemical cells (PECs) are reviewed.

TOC ENTRY

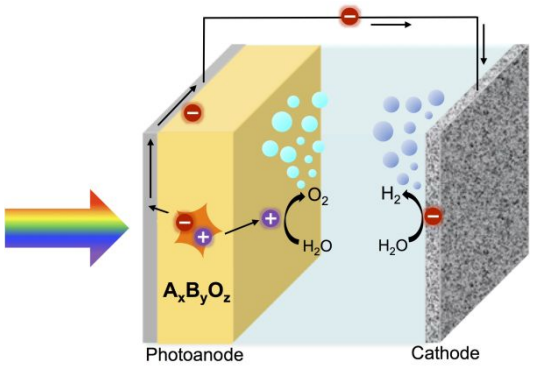

Advancements made in the development of ternary oxide-based photoanodes for use in water splitting photoelectrochemical cells (PECs) are reviewed.